Flash Sintering of Silicon Carbide Ceramics with Boron and Carbon Sintering Aids

Andrew R. Gibson
St Edmund Hall
University of Oxford

A thesis submitted for the degree of
Doctor of Philosophy
Hilary 2023

Acknowledgements

I’d begin by expressing my deepest gratitude to my supervisor, Prof. Richard Todd. Without his unwavering support and inspiring mentorship, completion of this thesis would not have been possible; he has changed his field - and his students - for the better. My time at Oxford has truly been formative and I owe him my sincere gratitude for the opportunity afforded to me.

Within the Materials Department, I would like to thank Tony Wheeler and Ian Sutton, who not only helped with the practicalities of a DPhil project, but who also kept the mood light. I would particularly like to thank Diana Passmore for her kindness and thoughtfulness in allowing me to make liberal use of the teaching labs for ‘just about an hour’ at a time throughout my DPhil. I’m sure she’ll appreciate going back to keeping her diary entries in pen, rather than pencil.

I would like to thank the members of Richard Todd’s ceramic group, past and present. Dr Tom Scott for his mentorship in my early days; Robin Lawrence for our ‘5 minute’ talks; and Dr Jiawei ’Jiang Jiang’ Jiang for getting me barred from my college bar - she was also an incredibly thoughtful friend to have and brightened the group more than she knew. I thank Yasuhiro and Shenghuan for their kindness and optimism; and to Doug, David, and Tuoran, for their friendship and support; our time in Warsaw was brilliant. To Christian, the lucky DPhil student who now must take the reins of flash sintering non-oxides, it was a pleasure to spend the time that we did together and I’m sure your research will far out class my own: good luck. Finally, Dr Jaspreet Singh (Jesse J). Although an unplanned ending to our DPhils, sharing a house together for this short time both embodied my time at Oxford, and was the perfect way to finish it. Some of my favourite memories of Oxford are from this period, and I hope he can share in that sentiment each time he looks at his arm.

My experience of Oxford would not be complete without Teddy Hall. From start to finish, the college MCR provided a social platform like no other and I am deeply grateful for all the friendships and memories it has helped foster. The most profound of which must be those formed with the boys in ‘Klub Kingston’: Dr Mark Baker, Esq. Elliot Bromley, Dr Jack Mills and Dr Ben White. From Croquet tournaments, Chinese exchanges, formals and college balls to the everyday tasks, I am incredibly grateful for the time that we spent together. I will cherish these memories for the rest

of my life, as I will their friendship. It should also go without saying that there are many other friendships that kept me going through the years: the guys from Glasgow University; the core six from back home; and no less notable mentions such as Cyril, Gilad and Tim. They enriched my experience in a way that only each individual could.

Last but certainly not least, I'd like to thank Abby for the caring and supportive role she has played since we met. A double lockdown could not be described as the best time to start a relationship, but she quickly became an integral part of my life, and I am incredibly grateful to have had her by my side (and that I published my paper first). Furthermore, the unwavering love and support from my entire family has been both moving and grounding. From nearly being kicked out of my undergraduate degree to now finishing my DPhil, they have weathered the storm as much as I have. I am incredibly lucky to be able to turn to a loving and thoughtful mother, a loving and dedicated father, and a loving, best friend of a sister. Any of my qualities that have got me this far I owe to them: this thesis is as much a culmination of my effort as it is theirs, and to them, I dedicate it.

Abstract

The aims of this doctoral thesis were to assess the feasibility of using flash sintering to manufacture silicon carbide and to understand how the technique affects its density, microstructure and mechanical properties.

An experimental apparatus was developed that allowed silicon carbide bar shaped specimens with boron and carbon sintering aids to be flash sintered to 96% density (with an average grain size of 4 μm) in 16 minutes in an alumina tube furnace at 1500 °C. Compared with samples of similar density that were conventionally sintered using the powder's recommended sintering schedule, the production time of the flash sintered samples was reduced by more than 6 hours and with a furnace temperature lower by 700 °C. Both methods sintered silicon carbide it in the liquid phase. Of the investigated flash sintering parameters, higher power limits, higher furnace temperatures, slower power ramp rates, and longer hold times were all found to increase the bulk density and the average grain size of specimens. The addition of carbon sources in the furnace tube during sintering was beneficial for sample densification, but could be detrimental if in close proximity to the sample. The additions also retarded grain growth in specimens and increased the time that samples could be flash sintered before fracturing from 16 minutes to 1.5 hours.

The Vickers hardness of most of the silicon carbide samples in this work was ~24 GPa. The inclusion of carbon additions in the furnace tube during sintering significantly increased the Vickers hardness of silicon carbide: 27.8 GPa ± 0.4 GPa. This increase in hardness was independent of density, grain size and polytype concentration but is suggested to be related to a carbon concentration threshold in the sintering atmosphere. Atom probe tomography analysis indicated that the super-hard silicon carbide samples had a greater concentration of boron rich clusters than silicon carbide of regular hardness. These clusters are suggested to cause dispersion hardening in these samples. Flash sintering did not degrade the strength or the fracture toughness of silicon carbide. If flash sintered silicon carbide was successfully scaled up, the material may outperform traditional silicon carbide armour plates in ballistic trials.

The flash event in a non-oxide ceramic was shown to be phenomenologically similar to that found in oxide ceramics: characterised by a rapid rise in sample temperature followed by densification and a decrease in sample resistivity. This behaviour was shown to be consistent with thermal runaway; the origin of which was found to be the early stages of sintering.

Statement of Originality

The work presented in this DPhil thesis has been conducted at the Department of Materials at the University of Oxford between October 2017 and January 2022, under the supervision of Prof. Richard Todd. The work in this thesis is original, and the work of others included within is acknowledged and referenced. Some of the work undertaken in this thesis has been published and presented at conferences as listed below:

Gibson, A., Li Y., Bonilla R. S. & Todd R. I. (2022). Pressureless flash sintering of α-SiC: Electrical characteristics and densification. *Acta Materialia*, 241, 118362.

Gibson, A., Li Y., & Todd R. I. (2022). Pressureless flash sintering of α-SiC. *Ceramics in Europe Conference 2022.* Oral Presentation. Warsaw, Poland.

Bechteler, C., **Gibson, A.**, & Todd, R. I. (2022). Formation and influence of plasma during flash sintering. *Ceramics in Europe Conference 2022.* Oral Presentation. Warsaw, Poland.

Gibson, A., & Todd R. I. (2022) (2021). Flash sintering of Silicon Carbide. *ECerS Student Speech Contest UK Heat.* Virtual.

Gibson, A., Li Y., & Todd R. I. (2022) (2019). Flash sintering of Silicon Carbide. *XVI ECerS Conference 2019.* Poster Presentation. Turin, Italy.

Todd, R. I., **Gibson, A.** & Li Y. (2019). Flash sintering of α-Silicon Carbide. *XVI ECerS Conference 2019.* Oral Presentation. Turin, Italy.

Contents

List of Abbreviations

APT Atom Probe Tomography

CVD Chemical Vapour Deposition

DC Direct Current

ECAS Electric Current Assisted Sintering

EDX Energy Dispersive X-Ray spectroscopy

FS Flash Sintering

FSPS Flash Spark Plasma Sintering

HAADF High Angle Annular Dark-Field

HP Hot Pressing

HIP Hot Isostatic Pressing

HRTEM High Resolution Transmission Electron Microscopy

LH Long Hold ramp rate schedule

NTC Negative Temperature Coefficient

SEPB Single Edge Pre-cracked Beam

SPS Spark Plasma Sintering

PTC Positive Temperature Coefficient

RGAr Research Grade Argon

SEM Scanning Electron Microscopy

SEVNB Single Edge V-Notch Beam

SNR Signal to Noise Ratio

TEM Transmission Electron Microscopy

XRD X-Ray Diffraction

List of Figures

Chapter 1

Introduction

Sintering of ceramics is an ancient technology, with evidence of its use dating back approximately 28,000 years[1]. The resultant ceramics have evolved from their primitive clay-based materials to high-specification engineering products with uses in a broad range of industries. Mining[2], nuclear energy[3], aerospace[4], energy storage[5], defence[6] and semiconductor industries[7] all make use of the unique properties of ceramics to find solutions to complex engineering problems that would be impossible with other materials. This diverse need of ceramics in industry has driven much of the research into improving their properties, reliability, and economic value.

To keep pace with this need, ceramic manufacturing technologies have changed drastically since their ancient conception. The introduction of pressure while sintering or the breakthrough in Electric Current Assisted Sintering (ECAS)[8] in the 1960s created materials with novel properties and functionalities[9]. However, the use of pressure in these techniques results in a drop in product throughput compared with the industrial scale[10] of pressureless sintering; there is an unmet need that combines the rapid heating rates of the ECAS technology with the lower cost of pressureless techniques.

The title “Flash Sintering” was first coined by Cologna et al. in 2010[11] and given to a technique that had the potential to fulfil this industrial need. Since it was first demonstrated by Cologna to densify 3YSZ in seconds (c.f. hours with conventional sintering), the technique has shown that it can successfully densify a wide range of ceramics[12–18]. Commercialisation of the technique is now underway at Lucideon, UK, who are investing in the technology with the aim of reducing the high production costs and time associated with ceramic materials for use in healthcare and energy storage applications[19]. While these are typically oxide ceramics, the benefits are likely to be even greater for non-oxide ceramics, which, due to their covalent nature, require even higher temperatures and longer hold times to fully densify. Despite this, there is little research regarding the fundamental understanding of how the technology affects the properties of non-oxide ceramics. As such a material, SiC has a wide range of applications and there is an industrial interest in making its manufacture more economical. The aims of this thesis were to assess the feasibility of using flash sintering to manufacture SiC and to understand how the technique affects its density, microstructure and mechanical properties.

Chapter 2 of this thesis introduces the important material properties of SiC and provides a critical appraisal of how the conventional, pressureless sintering technique, and various SiC sintering aids, affect the microstructure of SiC. It then introduces flash sintering and reviews the literature regarding the theories that describe the fundamental mechanisms that govern the phenomenon.

Chapter 3 explains the sample preparation; the flash sintering apparatus; the use of C insulation and C additions in the furnace tube; the flash sintering methodology; sample temperature estimation; the conventional sintering schedule; specimenc characterisation; microstructural analysis and the mechanical characterisation.

Chapter 4 is the first of the results and discussion chapters and details how each of the tested flash sintering parameters affected the densification of SiC and its microstructure. Electrical parameters include the electric field strength; electrical power dissipated in the specimen; power ramp rate and hold time at the maximum power limit. Investigations into the effect of furnace temperature and sintering atmosphere on sample microstructure and densification are also discussed.

Chapter 5 details the electrical response of SiC during flash sintering. The aim of this chapter was to explore what initiates the flash event in a non-oxide ceramic and test whether the most established theory that describes the flash event in oxide ceramics also characterises the phenomenon in a non-oxide ceramic.

Chapter 6 present the results of the mechanical characterisation of flash sintered SiC. The Vickers hardness, the 3-point flexural strength and the SEVNB toughness are discussed and compared with those of conventionally sintered SiC. The chapter concludes with a discussion of the applicability of flash sintered SiC to armour materials.

Chapter 7 provides a summary of the key findings of the investigations presented throughout the thesis. Chapter 8 closes with a discussion of the potential future work that aims to build on the findings of this thesis and the challenges that might face the commercialisation of flash sintered SiC.

Chapter 2

Literature Review

2.1 Introduction

2.1.1 Raw powder production

First synthesised in 1884 by E. G. Acheson by heating a mixture of clay and graphite, raw SiC powder to this date is still produced predominantly through the Acheson process[20]. The technique has changed little since then: an Acheson furnace (electrical resistance furnace) is filled with a mixture of silica sand and a C source, such as graphite, and heated until the centre of the mixture reaches 3000 °C. Ingots of α-SiC are formed at the centre of the mixture, while at its cooler extremities, β-SiC is formed from the reduction of SiO_2 by graphite. These ingots are then processed into raw materials for abrasives, refractories, and powders for sintered materials by crushing, acid treatment, rinsing, drying, magnetic cleaning and sieving[21]. In 1929, The U.S. Patent Office named Acheson's patent as one of the 22 most influential of the industrial era[22].

Following production using the Acheson process and the ensuing powder processing methods necessary to achieve fine powders, SiC powders typically contain impurities. Free-Si, free-C, O, and Fe contents are typically high, with trace amounts of Ti, Al, Ni and V[23]. These impurity contents may be incorporated into the SiC during sintering and affect final material properties.

2.1.2 Crystal structure and polymorphism

SiC crystals are structured in layers of SiC_4 tetrahedra, with each vertex shared with that of the adjacent tetrahedra[24]. Polymorphism arises in SiC as these Si-C bilayers stack in various combinations to form different crystal structures. Schematics of the crystal structures of the four most common SiC polymorphs, 2H, 3C (cubic), 4H and 6H are shown in Fig. 2.1. The 3C SiC, cubic structure is referred to as β-SiC, while all other polytypes are known as α-SiC, which can take hexagonal or rhombohedral forms.

Knippenberg[26] and Inomata[27] first investigated the thermal stability of various SiC polymorphs and an illustration of their results is shown in Fig. 2.2. Longer lattice constants result in high temperature stability; the 3C cubic phases is considered a meta-stable, low temperature phase[21]. The introduction of metallic elements affects thermal stability of the polymorphs, and elements such as N, Al and B readily form solid solutions with SiC[28], although their solubility is low. Jepps and Page observed that electron donor impurity atoms appear to stabilise the cubic SiC phase, while acceptor impurities stabilise hexagonal structures[29]. Al and B are known to stabilise the

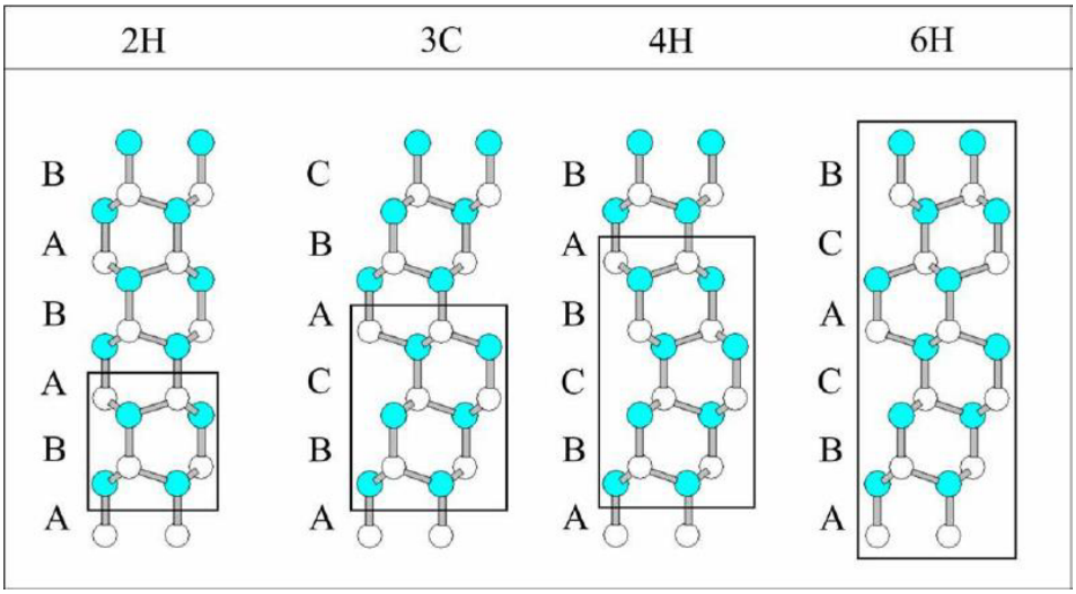

Figure 2.1: Common SiC polytypes[25]

4H and 2H polytypes[21], respectively, while N was shown by Kondo et al. to stabilise the 3C polytype[30]. Both Kieffer et al.**Kieffer1969PHASESi-C-N** and Jepps and Page[31] show that a N sintering atmosphere promotes the reverse phase transition from alpha to beta SiC.

2.2 Sintering of silicon carbide

2.2.1 Conventional sintering without pressure

2.2.1.1 Solid state sintering

As a diffusion-controlled process and driven by the removal of pore surface energy, sintering converts an inorganic, powder powder compact (green body) into a dense polycrystalline solid[32]. Traditionally, the process is subdivided into 3 stages: i) neck

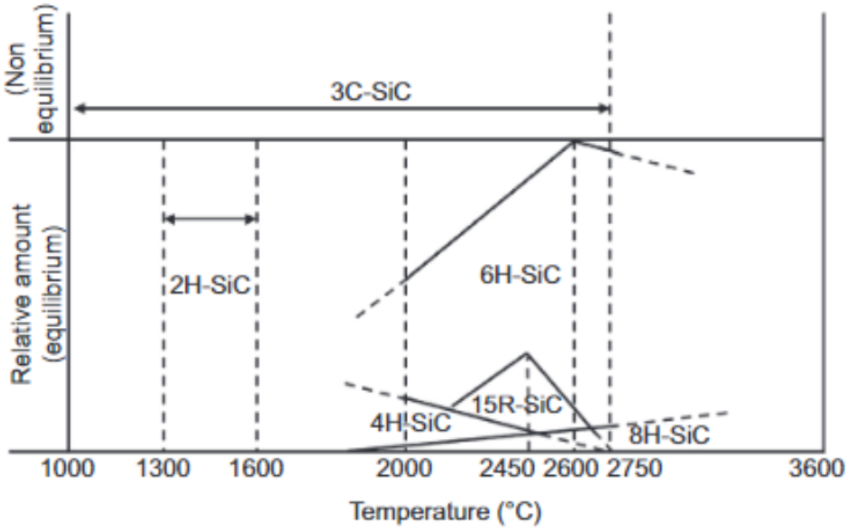

Figure 2.2: Thermal stability of SiC polytypes[26].

formation (where particle surfaces start to join); ii) intermediate sintering (material diffuses to fill up continuous open pore channels) and iii) final sintering stage (where the continuous channels pinch off to form individual, closed pores).

As described by Chiang et al., during sintering, matter can be transported to the "neck" (where the dotted arrows point to in Fig. 2.3) between two particles by six distinct processes: surface diffusion; lattice diffusion or vapour transport from the surface of the particle; grain boundary or lattice diffusion from the interface between the particles and finally, if dislocations are present in the material, these can also provide diffusion gradients to allow lattice diffusion to the neck[32]. A schematic of the processes is shown in Fig. 2.3.

If material is removed from the grain boundary/interface, the centres of the particles move closer together and an overall shrinkage in green body dimensions/ densification occurs. Mechanisms that draw matter from the surface of the particles and not the grain boundaries cause coarsening, where the centres of the particles do not move

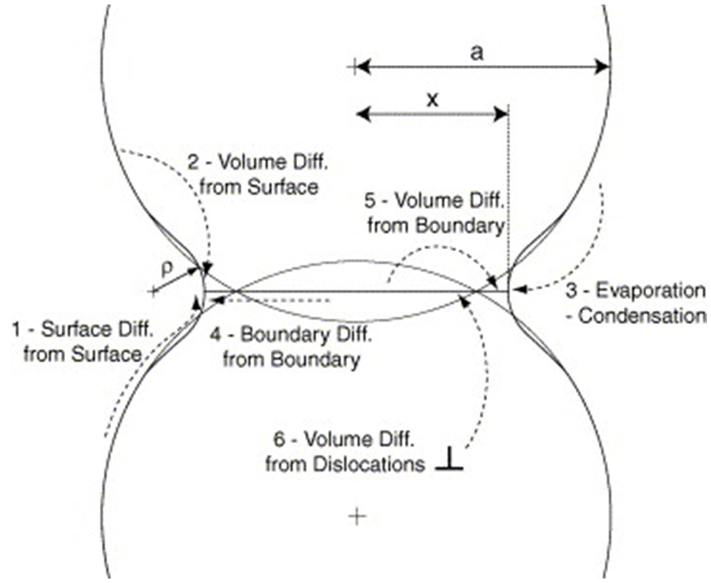

Figure 2.3: Diffusion routes during solid state sintering, where a is the particle radius and x the radius of the disc of contact between the two particles (Original illustration by Ashby[33,34]).

towards one another, and the material does not densify. In this instance, material diffusing from the surface shapes the pore into a spheroid while maintaining constant volume, which reduces curvature and hence the sintering driving force.

Each diffusional process is governed by its own activation energy and hence solid-state diffusion coefficients ($D = D_0 exp((-Q)/RT)$, where D is the diffusional coefficient, D_0, the pre-exponential coefficient, Q, the process activation energy, R the molar gas constant and T, the system temperature). Typically, $Q_s < Q_{gb} < Q_l$, where Q_s, Q_{gb}, Q_l represent surface, grain boundary and lattice activation energies, respectively. This indicates that surface and evaporation processes dominate at low temperatures, while grain boundary and lattice diffusion mechanisms are only activated at higher temperatures. This led to the principle behind fast firing techniques: that rapid heating of the ceramic powder avoids the low temperature coarsening regimes in favour of high temperature densification mechanisms.

If a secondary liquid phase is present during sintering and sufficiently wets the primary phase (and the primary phase is partially soluble in the second), matter is transferred rapidly from the grain boundary to the stress free interfaces (necks) in Fig. 2.3[32] by diffusion through the liquid film on the boundary. This is known as liquid phase sintering. The process initiates with particle rearrangement, which can also cause rapid shrinkage. Additionally, the low melting temperature of the sintering aids lowers the sintering temperature of the material.

2.2.1.2 Sintering of SiC with B,C sintering additives

Conventionally, B,C sintering additives have been thought to sinter SiC in the solid state. The first to successfully sinter SiC without pressure was Prochazka in 1975[35]. He hypothesised that free C added to SiC as a sintering aid removes the innate surface silica of SiC which increases the surface energy of the particles, while the B decreases the interfacial energy of the grain boundary. This decreases the ratio of grain boundary to surface tension, which satisfies the equation $\gamma_{gb}/\gamma_{sf} < \sqrt{3}$ (Young-Duprè equation[36] at a triple point) and sintering becomes possible.

Greskovich and Rosolowki[37] and, separately, Hase and Suzuki[38,39], dispute the existence of a thermodynamic barrier to sintering of SiC without pressure. Greskovich and Rosolowsk postulate that if powders are pulverised into smaller grains, sintering can occur. They measured dihedral angles of >100° at triple grain grain boundaries in SiC treated at 1900 °C and concluded that could be no thermodynamic barrier to sintering. From shrinkage rate measurements and specific surface area measurements they also conclude that B,C additives promote grain boundary diffusion while inhibiting surface diffusion.

Microstructures of SiC densified with B,C additives are highly dependent on temperature. Following the suggested sintering schedule by the powder manufacturer (2200 °C for 1 h), Magnani et al. created BC-SiC with a highly bimodal microstructure with very large, needle like grains (>100 µm)[40]. By using a two-step sintering profile which reduced the temperature to 2100 °C, then 2050 °C for 7 h, they significantly reduced the average grain size and homogenised the microstructure, while maintaining a high degree of densification (∼97%).

Some authors dispute that B,C sintering aids sinter SiC in the solid state. Akin to Greskovich and Rosolowsk, and Hase and Suzuki (above), Stobierski and Gubernat also disagree with the concept of a thermodynamic barrier to sintering SiC with B,C additions. Instead, they argue that the B,C additives form a liquid state during the sintering of SiC. By inserting BC-SiC samples rapidly into a dilatometer at 2150 °C, they show that as the amount of B in the sample is increased, clear microstructural evidence of a liquid phase appears[41]. They also show that the shrinkage rate increases with B content. A threshold is defined, 0.5wt.% B (and 3.3wt.% C), above which an excess of liquid phase is formed, and hence elongated SiC grains, a bimodal microstructure, and large B inclusions. Below this this limit, solid state sintering occurs, which results in slow densification rates and fine grains.

High Resolution Transmission Electron Microscopy (HRTEM) analysis by Li et al. shows an amorphous layer 6 nm wide at the grain boundary of pressurlessly sintered BC-SiC[42]. Although they could not determine if the phase was predominantly B or

C, the sintering additive concentration (0.4wt.% B and 0.4wt.% C) was chosen to be the same as the solubility limit of B in SiC (0.4wt.%), and hence they suggest that the phase was mostly C. Using HRTEM and High Angle Annular Dark-Field (HAADF) analysis on grain boundaries in BC-SiC (0.5wt.% B, 1wt.% C), Kaneko et al. show that B is only present at some of the SiC grain boundaries, and most of it is found in nano-sized B inclusions in the SiC grains, near the grain boundaries[43]. Similar findings are presented by Zhang et al. who use Transmission Electron Microscopy (TEM) and EDX to show that SiC sintered with ABC additions can form nanoscale inclusions that are rich in secondary phases throughout the SiC grains[44]. They show a slight depletion of the inclusions near grain boundaries, compared with the bulk of the grain.

These investigations suggest that the solubility limit of B in SiC is around 0.4wt.%, and in which case, gives further evidence to suggest that the empirically determined liquid phase threshold defined by Stobierski and Gubernat (0.5wt.% B at 3.3wt.% C) does correlate to the amount of liquid B at the grain boundary during sintering of SiC. The presence of a liquid phase at sintering temperatures is indicated from the pseudo-binary phase and ternary phase diagrams of B_4C-SiC[45,46] and additionally, the sintering temperature of BC-SiC (approximately 2150 °C) is above the melting temperature of B (2077 °C). The presence of a liquid phase with a melting temperature around that required to sinter SiC with B,C additives might also explain why Magnani produced SiC with excessive grain growth at 2200 °C but then with small, equiaxed grains when sintered at slightly cooler temperatures (2100 °C and 2050 °C)[40].

Given the above, it is suggested that, in contradiction to the original theory set out by Prochaska[47], the addition of B and C sinters SiC in the liquid phase. The extent to which full densification occurs entirely through liquid phase sintering or the subsequent, slower solid-state sintering is determined by the additive content. The B,C liquid phase allows the initial stages of sintering to occur. However, if the B content is low (below its solubility limit in SiC), the phase is entirely incorporated into the SiC grains as grain growth occurs, as inclusions or in solid solution, which leaves no excess liquid B at the grain boundaries and hence solid-state sintering ensues after the initial stages of sintering. It was noted by Gubernat and Stobierski that C alone did not densify SiC[48]. If the amount of B is greater than its solubility limit in SiC, then a liquid phase will remain at grain boundaries and hence liquid phase sintering will continue. It was observed by Zhang et al. that although these secondary phase inclusions can precipitate and become larger during annealing, this effect only became apparent after 700 h of annealing at 2050 °C[44].

Stobierski and Gubernat also argue that the role of C goes beyond removing the SiO_2 layer on SiC. They suggest that C plays an active role in sintering, as varying the C content of a green body affects the size and shape of the pores and the SiC grains during sintering[48]. They attribute this to C arresting ineffective transport mechanisms at low temperatures and during sintering. They also suggest that C could solidify the liquid phases during sintering, which could be expected from the tertiary phase diagram of B_4C-SiC[46]. Additionally, C chemically bonds with volatile Si at sintering temperatures, which improves stability of SiC and reduces the likelihood of thermal decomposition (discussed further in Chapter 4).

2.2.1.3 Liquid phase sintering of SiC with oxide additives

Liquid phase sintering of SiC with Al_2O_3 as a sintering aid was first achieved by Lange in 1975 using a hot press[49]. Most investigations of liquid phase sintered SiC focus on oxide sintering aids; Noviyanto and Yoon show that out of the various oxide sintering aids added to β-SiC during hot pressing at 1750 °C, only Al_2O_3, MgO and Y_2O_3 are effective at densification while remaining unreactive with SiC[50]. However, due to their low melting temperatures, oxide sintering aids reduce the high temperature utility of SiC ceramics.

2.2.2 Addition of pressure during sintering

Typically, for powder systems that are difficult to sinter, pressure can be applied to the powder compact while heating through HP[51], Hot Isostatic Pressing (HIP)[52] or Spark Plasma Sintering (SPS)[9,53] techniques. While HP and HIP techniques rely on more traditional heating of the powder compacts, in SPS technology, current is directly passed through the die that contains the powder compact. This allows faster heating rates to be achieved over the HP and HIP techniques. The use of pressure also allows SiC to be manufactured without any sintering additives[54]; an attractive property in the semiconductor manufacturing industry where the degree of purity and densification takes precedence over economy[21]. However, for many industries this is not the case, and inherent use of pressure results in a slow throughput, an inability to produce large, complicated shapes[21] and large overhead costs.

Given the inherent difficultly of sintering SiC without pressure or sintering aids, two distinct sintering grades of SiC powders can be defined: pressureless and pressure assisted powders. Pressueless grade SiC powders have sintering additives dispersed throughout the powder, like B and C. The addition of pressure during sintering relinquishes the need for sintering aids, as the additional pressure increases the driving force of sintering. While pressureless grade SiC can sintered using pressure, this would nullify the key benefit of not using sintering aids during densification, especially in applications where a secondary grain boundary phase is detrimental to that material's industrial uses.

2.3 Properties of silicon carbide

2.3.1 Electrical properties

2.3.1.1 Nearly free electron theory and band structure

Band structure in materials is understood via the nearly free electron theory and the solutions of the time-independent Schrodinger Equation[55]. In a given periodic energy potential over a volume of space, such as a crystal lattice, these solutions are known as Bloch functions. These periodic functions collapse to yield solutions with positive and negative Fourier coefficients – i.e. discontinuities in energy at Brillouin Zone Boundaries (the boundaries of the primitive cell in reciprocal space[56]). These discontinuities successively segment the continuous energy curve into allowed and forbidden (for pure, undoped materials) energy states that a free charge carrier can and cannot occupy, respectively.

These segments of allowed energy states are known as energy bands. Allowed energy bands below the Fermi energy level, E_F (energy level of highest occupied state are known as valence bands, E_V. States above E_F are known as conduction bands, E_C. The forbidden region between the valence and conduction bands is known as the energy band gap ($E_G = E_C - E_V$). Should an energy band be partially occupied, i.e. the Fermi energy level is within an allowed band structure, the material is known as a conductor. If the valence bands are totally full and the E_F lies within a large band gap then the material will intrinsically be insulating. However, should the Fermi level sit in a sufficiently small (0.5 - 2.5 eV) band gap, the material will conduct if an electron in the valence band is given sufficient energy to “jump” to the conduction band. This is known as a semiconducting material.

These materials can either have direct or indirect band gaps. Direct band gaps are defined to have the lowest point in E_C correspond to the highest point in E_V with the same reciprocal k-vector, i.e. electrons in E_V need only to overcome the energy of the band gap to cross to E_C[55]. For indirect band gap materials these two points in the conduction and valence bands are not coherent in k-space and hence require additional energy (momentum) in order to cross E_G (hence why Si requires 3.6 eV to create an electron-hole pair despite having $E_G = 1.12$ eV at 300 K)[55].

If an electric field is applied over the semiconductor, the charge carriers will migrate through the material towards the oppositely charged electrode. This accumulation of charge causes the valance and conduction bands to bend[57]. The energy band gap remains constant as the bands are bent.

2.3.1.2 Role of impurities in the electrical conduction of SiC

Trace impurities in a semiconductor can often dominate the electrical properties of the material. To control this electrical behaviour, net impurity concentrations can be added to a semiconductor in a process called doping1. As a group IV material, SiC can be doped with group III (Al, B) or V (N, P) elements which introduce either "acceptor" holes or "donor" electrons into the lattice, respectively. These alter the material's majority and minority charge carrier concentrations and hence it's conductivity. Schematically, these dopants are represented in the band structure as additional states in the normally forbidden zone or energy band gap. "Acceptor" holes sites appear near the valence band, while "donor" electron sites are closer to the conduction band. Materials doped with donor impurities are labelled as n-type semiconductors and their majority charge carriers are electrons, while materials doped with impurities that form acceptor sites, and are known as p-type semiconductors whose majority charge carriers are holes.

2.3.1.3 Thermoelectric effects in silicon carbide

The Peltier effect arises when an applied DC electric field forces current through the junction of two materials with different Fermi energy levels[58]. This manifests as heating or cooling at the junction of the two materials. The direction of the current and the Peltier coefficient of the junction (material dependent) determines whether heating or cooling occurs. The Peltier coefficient is defined as:

$$\Pi_{AB} = \frac{\dot{q}}{I} \tag{2.1}$$

i.e. which represent the proportionality between the thermal and electrical current densities in the respective electric conductor where Π_{AB} is the Peltier coefficient of a junction between materials A and B, $\dot{q}$ is the rate of heating, and I is the current. Material A is defined as the material that the current leaves before entering material B. The coefficient is defined as positive when the electrical current causes heating when passing from material A to B[58]. In practice, the Peltier coefficient is difficult to determine experimentally[58]. Instead, another thermoelectric coefficient, the Seebeck coefficient, which describes the electromotive force induced in a heated junction of two dissimilar materials, can be used to calculate the Peltier coefficient. This is more easily determined experimentally and can be related to the Peltier coefficient by:

$$\Pi_{AB} = \alpha_{AB} = (\alpha_A - \alpha_B)T \tag{2.2}$$

where α_A and α_B are the Seebeck coefficients of the two individual materials and T is the temperature of the junction[58]. Seebeck coefficients are temperature dependent[59,60].

2.3.1.4 Electrical resistivity of SiC

A review of liquid phase sintered SiC by Kim et al. discusses how the electrical resistivity of SiC can be modified to span over 14 orders of magnitude by introducing acceptor or donor impurities into the SiC lattice[61]. Kim suggests that N acts as a donor impurity by introducing n-type sites in the energy band gap which increase the conductivity of sintered SiC heating elements. They also show that doping the SiC lattice with Al or B introduces holes, or acceptor sites in the band gap, which reduce conductivity by three orders of magnitude by trapping negative charge carriers. This acceptor-donor compensation was also observed by Taki et al. who observed a drop in conductivity of N-doped SiC by doping it with B[62].

The temperature dependent resistivity of SiC heating elements was investigated by Gnesin et al.[63] They showed that sintered SiC has a Negative Temperature Coefficient (NTC) of resistivity when heated from room temperature to ∼1000 °C and then is largely independent of temperature thereafter. They postulate that this low temperature behaviour is caused by the promotion of electrons from the valence bands to the conduction bands. Once most of the electrons are promoted, there is little change in the charge carrier concentration and hence a temperature independent resistivity. This temperature independent region of resistivity was also observed by Racette[64].

2.3.2 Thermal properties

Typically, SiC has a high thermal conductivity. Slack[65] estimates that the thermal conductivity of single crystal SiC at room temperature is 490 W m^{-1} K^{-1}. However, polycrystalline SiC materials have lower thermal conductivities, owing to their random grain orientation, lattice imperfections, pores and grain boundary phases[66–68]. SiC sintered without pressure and with 1wt.% B and 3wt.% C has been shown[69–71] to have a thermal conductivity in the range of 110 – 140 W m^{-1} K^{-1}. Li et al. increased the thermal conductivity of BC-SiC to 180 W m^{-1} K^{-1} by using novel B-C sources (boric acid and D-fructose)[42]. They suggest this reduced the amount of B defects in the SiC grains, which are detrimental to thermal conductivity.

Munro et al. show that the specific heat capacity of SiC increases with temperature (650 – 1400 J W kg^1 K^1 from room temperature to 2200 °C) due to an increase in internal (rotational and vibrational) energy, but it is not dependent on the sintering aid used[71]. Thermal decomposition of SiC has been shown to occur at temperatures about 2500 °C[72] and Stobierski and Gubernat expect thermal decomposition of SiC to occur above 2000 °C[41]. Dolloff[72] reported that, at ambient pressures, SiC melts incongruently with Si melting and a C solid remaining in the microstructure.

2.3.3 Mechanical properties

2.3.3.1 Vickers hardness

Depending on indentation technique and the microstrucuture of SiC, the Vickers hardness of SiC can have a wide range of values. Fine and coarse grained SiC armour materials were investigated by Wade et al.[73]. Both materials had hardness values that were within experimental error of the other (approximately 23 and 22 GPa with a 4 kg load, respectively). Similar results were found by Magnani et al., which show that increasing the sintering time of SiC with B,C additives produces highly bimodal microstructures with very large elongated grains, compared with the same powder but sintered in a two-step process which produced a microstructure with much finer grains[40]. They found that this makes little difference to the Vickers hardness of the material for the hardness of the materials was within experimental uncertainty of the other. This contrasts with behaviour expected from the Hall-Petch equation[74], which suggests that lowering the average grain size will impede dislocation movement and hence increase the hardness of the material (to a point, before grain boundary sliding dominates and smaller grain sizes are detrimental to hardness). The difficulty of moving dislocations through a covalently bonded ceramic is more likely to contribute to the hardness of the material than the effect of dislocation pileup at its grain boundaries.

The effect of B_4C concentration on the hardness of SiC has been investigated previously and higher than average hardness values were reported[45,75–77]. Each investigation produced B_4C-SiC through different processing routes (Chemical Vapour Deposition (CVD)), pressureless sintering and HP) and a common processing variable/heating schedule could not be identified between each of the tests. Shaffer et al. showed that a B_4C-SiC material cannot reach the hardness of B_4C[45]. The increase in hardness of the B_4C-SiC is suggested by Kieffer et al. to be caused by dispersion hardening by sub-microscopic separation of B in the SiC grains[75]. The investigations above indicate that the hardness of SiC may be more dependent on the secondary phase within the SiC grains than necessarily on grain size or shape.

2.3.3.2 Fracture toughness

Fracture toughness values of BC-SiC that could be expected from the literature are shown in Table 2.1. To investigate the fracture mechanism of SiC, Kim et al. doped α-SiC with β-SiC (and B,C sintering additives), to produce SiC with fine and coarse microstructures[78]. Their results show that while the fracture mode in both samples is predominantly transgranular, the fracture surface of the former may have sections of intergranular fracture.

However, this does not appreciably alter the fracture toughness of either sample, which remains within experimental uncertainty of the other. They attribute this to the strong interfacial bonding of SiC grains produced using B,C sintering additives. Similar findings are shown by Magnani et al. who use long hold times and two step sintering profiles to create BC-SiC with fine and coarse microstructures which shows no discernible difference between the toughness of either sample[40]. Considering this discussion, the variation from 2.5 – 3.2 MPa $m^{-1/2}$ of the values in Table 2.1, in which all the materials had mainly transgranular fracture, is likely a consequence of the testing technique.

In separate work, Malik et al. show that it is possible to increase the fracture toughness of SiC by doping it with BN to decrease the strength of the interfacial bonding between grains[82]. The high interfacial residual strains caused by the thermal expansion mismatch between SiC and BN phases results in interfacial debonding. This dissipates strain energy, causes crack deflection and creates interlocking sections of crack and hence increases the fracture toughness of the material. Similar

Authors	Test	Fracture toughness [MPa $m^{-1/2}$]
Rao et al.[78]	SEVNB (3-pt)	3.2 ± 0.2
Wang et al.[79]	SEVNB (3-pt)	2.7
Gogotsi et al.[80]	SEVNB (4-pt)	2.61 ± 0.14
Kaur et al.[81]	SEPB	2.5 ± 0.2

Table 2.1: Fracture toughness values of BC-SiC from the literature.

Authors	Test	Flexural strength [MPa]
Hurst et al.[85]	4-pt	320 - 467
Munro et al.[71]	4-pt	359
Chen et al.[86]	3-pt	312
Wu et al.[87]	3-pt	349 - 431
Magnani et al.[40]	4-pt	556

Table 2.2: Flexural strength values of BC-SiC from the literature.

weakening of interfacial bonding between grains can be achieved by introducing a weak grain boundary phase, such as that created from the addition of Al to BC-SiC. Cao et al. report a hot pressed SiC material with a very high fracture toughness of 9.1 MPa $m^{-1/2}$, as the weak liquid interfacial phase causes crack deflection between SiC grains and crack bridging[83].

2.3.3.3 Flexural strength

BC-SiC has a range of flexural strength values, despite the same testing method being used by different authors (Table 2.2) to establish its value. Investigating the effect of fine and coarse grained microstructure on flexural strength of α-SiC doped with B,C sintering additives with varying contents of β-SiC, Malik et al. show that flexural strength inversely correlates with grain aspect ratio[84]. They suggest that this is caused by the superior sinterability of α-SiC and the smaller flaw sizes that are attributable to this. The sample with the highest flexural strength in Table 2.2 was created using a two-step sintering profile which produced a microstructure with fine grains. This may justify Malik's conclusion further.

2.3.4 Ceramic armour

The properties of ceramic materials give them utility in ballistic armour applications. The ceramic is used as the strike face in light weight, bi-layer armour systems, with the ceramic bonded to a strong and tough backing material. A schematic of the system is shown in Fig. 2.4 and illustrates how it might defeat an incoming projectile[88]. Compared with conventional, metallic armour materials, ceramics typically have a higher hardness and better ballistic mass efficiency: a smaller mass of ceramic is required to defeat a high kinetic energy threat than would be necessary of a metallic armour[89]. These lightweight ceramic armour systems are used as hard plate inserts in personal armour, appliqué armour for light vehicles and in ultra-light weight applications, such as armour systems in helicopters[90]. The better ballistic efficiency of ceramic armours over that of metallic compositions results in greater battlefield mobility, but the cost of the ceramic materials can be prohibitive.

The time in which the projectile is in contact with the armour surface and minimal armour deformation occurs is known as dwell[88]. During this time, the area of the projectile that is in contact with the ceramic surface erodes, and material from this area flows radially outwards. The magnitude of the erosion and deformation of both materials is increased by the lateral confinement of material around the point of impact by the surrounding, undamaged ceramic. Eventually, enough ceramic material is removed and the stress wave that is reflected from the backing plate causes the ceramic armour to fracture and form a cone of material underneath the point of contact. This spreads the load of the impact over a wider area and reduces the stress

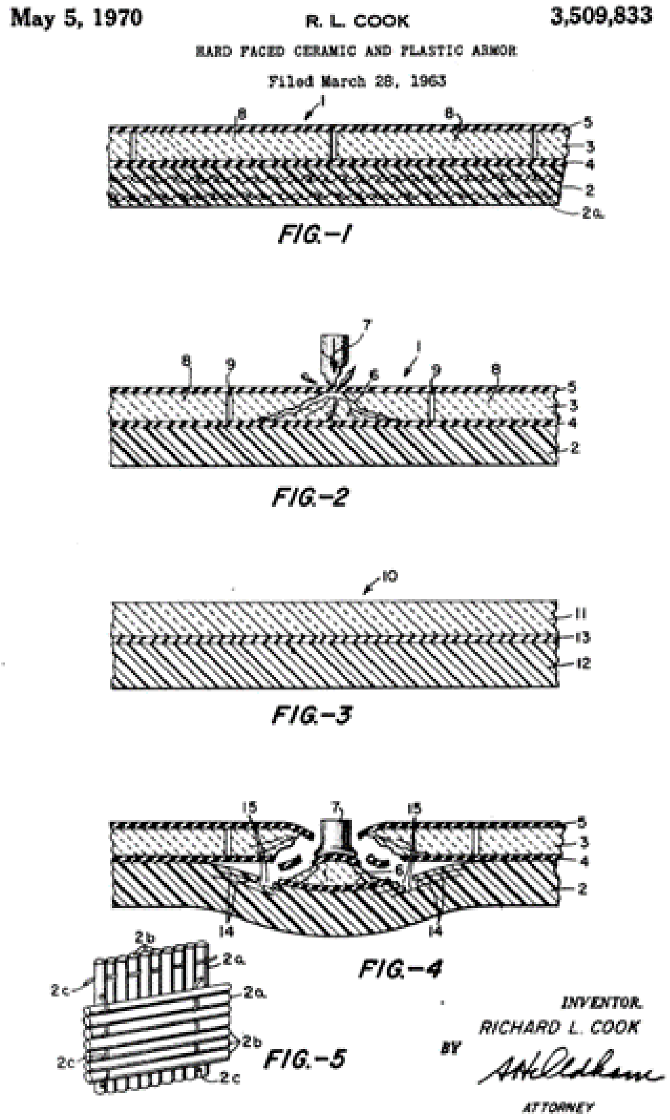

Figure 2.4: Patent illustration of design and proposed operation of ceramic - plastic armour system[88].

applied to the ceramic. With the kinetic energy of the projectile significantly reduced, the ductile backing material is able to deform and absorb the last of the projectile's kinetic energy. While this is the theory behind projectile defeat, it does not hold for every ballistic interaction.

Due to the dynamic nature of a ballistic impact and the simultaneous occurrence of multiple mechanisms that lead to failure of the ceramic armour during the process, understanding which microstructural features of the ceramic correlate with ballistic performance is challenging. The hardness of a material has been acknowledged as an important aspect[91,92], but ceramic plasticity[91,93], and fragmentation behaviour[94] have also been indicated as influential parameters. Hallam et al. indicate that Knoop hardness might correlate with V_{50} ballistic performance against armour piercing rounds (V_{50} is the velocity at which 50% of the projectiles will penetrate a target) and suggest that the variability in indentation behaviour correlates with that of ballistic performance[6]. However, they acknowledge the widely accepted result[95–97] that there is not a single material property that is the determining factor that might predict the ballistic performance of a ceramic material.

As summarised by Dresch et al.: a hard material is required to erode and fracture the incoming projectile; high fracture toughness and strength values give the armour multi-hit capability; the elastic modulus is related to the stress wave propagation which spreads the area of damage; and the fracture mode is associated with the amount of energy absorbed during the impact[98]. Trade-offs between these material properties result in no “silver bullet” with regard to ballistic performance: Boldin et al. recommend B_4C or SiC ballistic plates for moderate protection and minimum weight, but Al_2O_3 armour if multi-hit capacity is required[90]. If V_{50} performance is to be used as a benchmark to compare ballistic performance, Hallam et al. showed that out of leading armour grade ceramics such as B_4C and SiC-AlN-C, SiC + 5wt% B_4C was the highest performing armour material[6]. However, there are other influencing factors which might affect the result of V_{50} trials (such as backing plate choice), and it is difficult to determine the optimal ceramic strike face for all scenarios.

2.4 Flash Sintering

2.4.1 Background and principles of the phenomenon

2.4.1.1 Background and description

Flash sintering is a novel ceramic manufacturing technique. Under investigation since it was reported in 2010[11], it has since shown its ability to densify a wide range of ceramics[12–18]. The process involves heating a powder compact (green body) in a furnace whilst passing an electric current through it. The electric field that draws the current through the sample is applied over the specimen using contacting electrodes, typically attached to the ends of the specimen. Depending on the conductivity of the material that is to be sintered, electric field strengths can vary from 10 – 1000 $\mathrm{V\,cm^{-1}}$. The preheating temperature is lower than conventional sintering temperatures. This preheating reduces sample resistivity which allows more current to flow. In turn, this heats the sample through Joule heating and causes a further drop in the resistivity of the specimen. This NTC behaviour is a characteristic of most ceramic materials. Under constant voltage, this runaway process continues until the current increases very rapidly up to a pre-set current limit, where it is held for a period of time. This runaway phenomenon is the hallmark electrical trait of the technique and is termed the "flash event"[16]. The critical combination of furnace temperature and electric field strength at which this occurs is dependent on the resistivity of the material being sintered. This was the original heating schedule used by Cologna[11], but there are now many other electrical loading schedules used in flash sintering. In all of them, densification through sintering occurs during the process, often in a few seconds for most oxide ceramics[11,99]. While this hallmark electrical behaviour has been shown over the full range of materials tested, controversy remains as to the fundamental mechanisms that govern this behaviour and the subsequent rapid densification of the specimen.

2.4.2 Mechanisms of flash sintering

2.4.2.1 Thermal runaway

A thermal runaway model based on an inverse Arrhenius dependence of sample resistivity on temperature was developed by Todd et al.[100] (a similar publication regarding thermal runaway in ZnO by Luo et al. closely followed[101]). They describe the flash event as a process that involves an exponential rise of the rate of Joule heating which eventually dominates the sample's radiative losses which initially act to prevent the thermal runaway process. The model accounts for current and temperature localisation by attributing such characteristics to insufficient thermal conductivity in homogenising the temperature profile across the cross section of the sample. Further to this, their model accurately accounts for the incubation time before the flash event; predicts the critical furnace temperature at which the "flash event" occurs; and the quantitative evolution of the electric field, current and resistivity throughout the flash sintering of 3YSZ. A more detailed numerical analysis is given by Hewitt et al., but the same conclusion is reached: that the electrical and thermal characteristics of 3YSZ during flash sintering can be attributed to simple thermal runaway[102].

Jha et al. assert that linearization of parameters present in the aforementioned numerical analysis is likely to render inaccurate results, "given the non-linear increase in conductivity observed in flash sintering". They attribute this non-linearity to a generation of charged defects within the material[103]. However, a model derived from non-linear differential equations developed by da Silva et al. predicts flash sintering characteristics of 3YSZ and provides evidence to counter this. Their model shows that the critical condition for the flash phenomenon is less to do with sintering kinetics (defect related) than with the temperature dependant resistivity of the sample[104].

2.4.2.2 Defect induced densification

Raj suggests that there must be at least one other active mechanism in flash sintering, as Joule heating alone could not account for the observed densification rates. He attributes the sudden increase in sample conductivity to avalanches of Frenkel pair defects induced by the electric field[105]. These defect pairs are created when an atom moves to an adjacent interstitial site in the lattice; the vacancy and this interstitial are known as a Frenkel pair[106]. Raj argues that a critical combination of field and temperature leads to the nucleation of regions within the sample of high defect concentrations which increases conductivity and diffusivity within the sample, initiating the flash event. These defect populations aid chemical diffusion and are claimed to be responsible for the electroluminescence and non-equilibrium phase transitions proposed in the isothermal hold period of flash sintering.

Grasso et al. highlight several factors that must be accounted for to enable the Frenkel pair theory to become viable: i) the theory only applies to materials that would allow the creation of Frenkel pairs, but flash sintering has been demonstrated in multiple electronic conductors[107–109] (in which defects such as Frenkel pairs are not usually present); ii) ionisation of the interstitials would require far larger fields than those commonly used in flash sintering experiments; iii) the Poole-Frenkel mechanism[110] lacks an incubation period also found in flash experiments[111]. Bechteler et al. have also shown that the "electroluminescence" during flash sintering is actually thermal radiation[112]. All of the above make it unlikely that flash sintering is initiated by an avalanche of crystal defects.

2.4.2.3 Similarities with dielectric breakdown

Biesuz et al. highlight the similarities between the flash event and dielectric breakdown in alumina[113]. Dielectric breakdown typically requires much larger field strengths than those encountered in flash sintering. However, Biesuz et al. suggest that the correct combination of furnace temperature and sample thickness, porosity and purity levels can decrease the dielectric breakdown strength of alumina to those found in flash sintering experiments. They show[114] that a flash event can be initiated in alumina using an electric field strength of 500 V cm^{-1}, despite the dielectric breakdown of polycrystalline alumina[115] requiring electric field strengths in the range of 1500 – 4500 V cm^{-1}.

While there are similarities between the electrical characteristics of flash sintering and dielectric breakdown, there also discrepancies. Flash sintering occurs over the order of tens of seconds, whereas dielectric breakdown is far more sudden (~ms). At relatively low electric field strengths, the flash event is preluded by a gradual increase in conductivity - behaviour that would not be expected of a material that had dielectrically broken down. It should be noted as well, that dielectric breakdown typically causes irreversible damage and eliminates any insulating property of that material[115]. This is not the case for ceramics samples that have been flash sintered[116].

2.4.3 Flash sintering of non-oxides

Although the bulk of flash sintering investigations to date have focused on oxide ceramics, the same cost-effective attributes of the technique make it attractive for production of non-oxide ceramics as well, especially as they typically require higher temperatures than their oxide counterparts to fully densify.

Pressureless flash sintering of SiC with oxide sintering aids (Yttria Alumina Garnet) was first attempted by Zapata-Solvas using a modified hot press[16] (no additional pressure aside the weight of the graphite ram was applied to the sample). While the results are promising, the highest bulk density reached to date is 88% and liquid phase sintering aids compromise the high temperature properties of the SiC that is produced. Candelario et al. attempted to flash sinter a similar material[117]. While they showed that flash sintering benefits from finer powders, a greater additive content and better dispersion of additive due to colloidal processing, their final material was highly porous.

To increase sample density, Grasso et al. introduced pressure through Flash Spark

Plasma Sintering (FSPS), described in section 2.2.2) and were able to densify SiC with B,C sintering aids to high densities[107]. However, the use of pressure required presintered greenbodies and would result in large overhead costs if commercialised. FSPS has been used to sinter ZrB_2[109] and high density WC has been achieved with only modest pressure and using a non-conducting die as thermal insulation[17,108]. While these materials have resistivities that have an intrinsic Positive Temperature Coefficient (PTC), the resistivity of ceramic greenbodies generally exhibit NTC behaviour, which allows flash sintering to initiate in these materials. Flash sintering of B_4C has been attempted. However, densities above that of the green body were not achieved; sintering only occurred in localised hot spots[118].

2.4.4 Flash sintering apparatus and temperature estimation

2.4.4.1 Flash sintering apparatus

In essence, flash sintering apparatus consists of a furnace and a power supply. In a typical flash sintering experiment, the powder compact is placed in a furnace and attached to electrodes, which are connected to a power supply, outside of the furnace. The furnace can be sealed to allow an inert sintering atmosphere. Software is usually required to record electrical data from the power supply; from which the electrical properties of the sample during flash sintering can be estimated.

Numerous furnace designs have been developed: vertical tubular[14,119], horizontal tubular[120], quadrupole lamp[121,122], modified HP[16] or FSPS machines[107,109,123–126], vertical tubular split[127], induction heating[128], box furnace[100,129], or alternatives based on flame heating[130], arc torch[131] and recently, the use of an arc plasma as a sample pre-treatment immediately before flash sintering[132].

Of these apparatuses, a modified SPS (FSPS) has been used to fabricate high density SiC[107,124]. The technique places graphite felt around the sample which allows pre-heating until a temperature is reached such that current flows through the sample once it is sufficiently conductive. Samples require pre-sintering to withstand the use of pressure in this technique. Prior to this, Zapata Solvas et al. used a conceptually similar precursor to the FSPS machine to flash sinter SiC without pressure[16]. Their modified hot press machine heats the sample via a graphite susceptor, which is heated via an induction coil. The vertically aligned graphite punch above the sample is connected to the power supply and the HP frame is earthed. Only the weight of the graphite punch is exerted on the sample. Neither the FSPS or the HP methods allows visualisation of the sample while flash sintering.

One of the inherent flaws of the flash sintering technique is the inhomogeneous microstructures it creates within samples. This is caused by thermal gradients between the hot centre of the sample where the electrical power is dissipated by the current, and the cooler furnace surrounding the sample. Biesuz et al. show that the use of thermal insulation during flash sintering can increase the density of 8YSZ specimens[133]. They surrounded the samples in alumina felt, wool and coarse zirconia powder and found that reducing the heat loss from the surface of the sample increases its density by 4-10% and increases the average grain size at its surface, compared to when no insulation is used. Li et al. managed current localisation by appropriate electrode placement, which forced the current to the edges of the sample[134]. Clever thermal management will be key if the flash sintering technique is to be commercialised.

2.4.4.2 Errors in temperature estimation

Small sample sizes, high electric field strengths and high sample temperatures make obtaining accurate temperature measurements during flash sintering challenging. Accounts of the main methods are briefly described below.

- Thermocouples: due to the current small size of flash sintering samples, 0.5 - 1.5 mm diameter thermocouples may give slow response times in measurements and may act as a heat sink, affecting the sample temperature. Thermocouples operate due to the thermoelectric effect, i.e. that a temperature difference gives rise to a potential difference which can be calibrated to give a temperature reading. As a result, the thermocouple must be electrically insulated – usually through use of thermally insulating oxides – which might be expected to yield inaccurate results during the transitory stage in flash sintering (the power spike)[111].

- Pyrometry: using either single or dual wavelength measurement pyrometers (the latter being insensitive to surface emissivity) it is possible to detect the surface temperature of samples during flash sintering. However, the small sample sizes of flash sintered specimens make this technique prone to error, as additional light from the furnace may be captured by the pyrometer and affect the temperature estimation.

- Impedance: as a means of in situ thermometry, impedance spectroscopy informs the user of bulk sample temperature, assuming no change in sample shape or conduction mechanism, by translating electrical resistance data (real part) at an appropriately high frequency into a calibrated temperature reading. It has been shown to detect high temperature runaway in 8YSZ (≥1500°C)[135]. However, the assumption that there is no change in sample geometry does not lend itself well to flash sintering, in which shrinkage is a fundamental mechanism that drives densification and hence may introduce error in the estimation of sample temperature. Additionally, the passage of DC current through the sample fundamentally changes the electrical properties, invalidating any calibration.

- Blackbody model: As first proposed by Raj et al., the sample temperature during flash sintering can be calculated using the blackbody radiation model[136]. The ease of this method as a means of estimating temperature, and that it provides no worse estimations of temperature than those methods described above, are likely some of the reasons for its wide spread use in flash sintering[100,116,136]. Its drawbacks however include, the errors associated with green body emissivity values and that it assumes a uniform temperature distribution across the sample's surface, which modelling has shown not to be the case during flash sintering[116].

2.5 Summary and research aims

SiC is an important structural ceramic with many uses in industry, but the energy consumed by the current processing methods is significant and can make production prohibitively expensive. This chapter has discussed how SiC can be sintered conventionally without pressure and using B,C liquid phase sintering aids, and that the hardness of SiC may not be entirely dependent on the average grain size of the material.

Flash sintering is a novel manufacturing technique that can densify ceramic materials in seconds, without the need for applied pressure during sintering. This reduces the cost and energy exhausted during manufacturing significantly. This literature review has shown that while the fundamental mechanisms that initiate the phenomenon are disputed, consensus is building around the process sharing similar electrical and thermal characteristics to thermal runaway. It also shows that while the novel technique has successfully densified a wide range of ceramics, the bulk of the research has focused on oxide materials. There is a large, unmet need to better understand how the novel manufacturing technique affects the properties of a non-oxide ceramic and improve the density attained in pressureless flash sintering of these materials.

The aims of this thesis were to assess the feasibility of using flash sintering to manufacture a non-oxide material, SiC, and to understand how the technique affects its microstructure; how the material behaves during flash sintering; to optimise that processing route to achieve high density SiC; and then compare the mechanical properties of flash sintered SiC against those of the conventionally sintered material. Bar shaped specimens will first be attempted, but the challenge of scaling up the process will also be investigated. These aims are performed under the umbrella investigation into whether flash sintering could be used to manufacture SiC for armour applications in the Defence sector.

Chapter 3

Materials and Methods

A list of all flash sintering parameters that were tested is given in Table. A.2

3.1 Sample preparation

All samples were made from H.C. Starck Starceram SQ pre-mix, consisting of UF-15 α-SiC (d_{50} $\sim$0.75 μm), sintering additives (2.5–3.5 wt% C, 0.5 wt% B). A list of powder properties are given in Table. A.1. The powder was uniaxially pressed into bars or discs and cold isostatically pressed at 200 MPa. The green bodies had relative densities of $\sim$60%. Typical dimensions of the volume of the green body bars between the flash sintering electrodes were: 22 mm × 6 mm × 2 mm (lxbxh). The height was increased to 3 mm and 4 mm to investigate the effect of sample thickness. Disc shaped sample dimensions were: 11 mm dia. and 4 mm height.

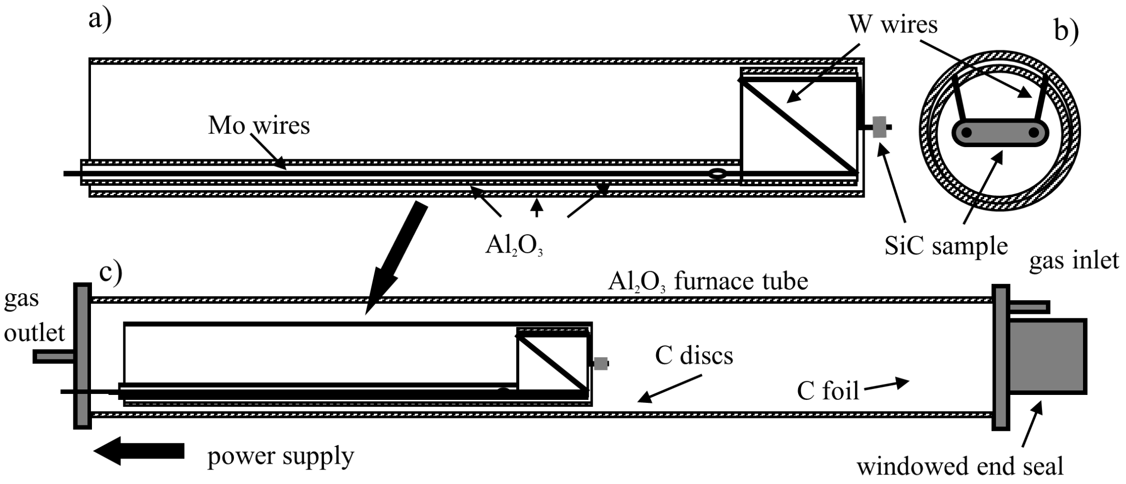

Figure 3.1: Flash sintering rig schematic from a) side elevation and b) end view perspectives, c) the flash sintering rig mounted inside a horizontal alumina tube furnace. Carbon discs and foil additions were added to understand their effect on microstructure but did not form part of the standard apparatus

3.2 Flash sintering apparatus

3.2.1 Tube furnace apparatus

Samples were preheated in a modified alumina tube furnace with a windowed end. Holes were drilled at both ends of the sample, which were then threaded onto tungsten wires mounted on a removable flash sintering rig (Fig. 3.1b). PELCO© High Temperature Carbon Paste was applied at the ends of the sample and the areas of the sample directly around the electrodes to reduce contact resistance. The whole rig was then sealed in the tube furnace. The current carrying wires protruded through one of the furnace end seals and were connected to the Direct Current (DC) power supply (EA PS9750-60A-3W, EA Elektro-Automatik, Viersen, Germany). Data were recorded via a LabView script.

3.2.2 Carbon additions in the furnace tube

To investigate the effect of a carbon rich atmosphere on sample properties, a stack of three carbon discs was placed below the sample and/or, a cylinder of carbon foil could be placed in the furnace near the gas inlet valve. The positions of these carbon additions are shown in Fig. 3.1. Heating rates followed the 400 W and 550 W power schedules (section 3.3).

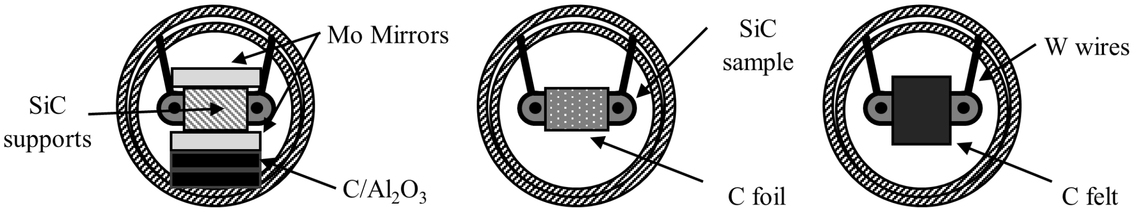

Figure 3.2: Various thermal insulations a) Mirror 2 set up, with carbon discs only, b) carbon foil (insulation), and c) carbon felt. All specimens were produced using the 550 W heating schedule (section 3.3).

3.2.3 Carbon insulation

The electrode configuration used in this work has been modelled previously and shown to produce non-homogeneous temperature distributions throughout the volume of a YSZ sample[116]. This is caused by current localization through the centre of the sample, between electrodes, and radiative heat loss from the sample's surface. To mitigate these heat losses, various thermal insulations were investigated (Fig. 3.2): thermal mirrors, C felt and C foil. This will test which, if any, of the insulations most effectively prevent heat loss from the sample's surface to increase the temperature of the sample's edge and create a more homogeneous microstructure. If net heat flow from the sample's surface to the environment is reduced, bulk sample temperature may increase as well. The constituents of the mirror set up were tested individually (mirror 1, 2 and 3), to assess the affect of each on sample microstructure and properties.

Three types of insulation were wrapped or placed around the specimen in separate insulation tests: a mirror system comprising of molybdenum mirrors above and below the sample and polished SiC supports that face the samples largest flat surface areas (lxb face); a cylinder made of carbon foil; and a folded length of carbon felt. Schematics of the insulations are shown in Fig. 3.2. The entire mirror set up was supported by a stack of three discs made from either carbon or alumina. Note the distinction between carbon foil used as insulation and that added at the gas inlet valve (Fig. 3.1). Variations of the mirror set up are given in Table 3.1.

Mirror 1	Mirror 2	Mirror 3
Carbon foil	No foil	Carbon foil
Alumina discs	Carbon discs	Carbon discs
Mo mirrors	Mo mirrors	Mo mirrors

Table 3.1: Variations of the mirror set up.

3.2.4 Modified hot press apparatus

The same modified hot press used by Zapata-Solvas et al. in the preliminary investigation into flash sintering SiC was also used in this work to flash sinter SiC discs[16]. A schematic of the apparatus can be found in their publication. Furnace heating was provided by an induction heated cylindrical graphite susceptor, with the specimen situated in its central cavity, sandwiched between two vertical graphite rods. The top rod was connected to a DC power supply (EA PS9750-60A-3W, EA Elektro-Automatik, Viersen, Germany) and electrically insulated from the rest of the apparatus by a concentric alumina tube. This forced the current through the sample once it was sufficiently conductive. The force of the top electrode (top graphite rod) on the sample corresponds to a compressive stress on the order of 0.1 MPa.

3.3 Flash sintering process

The furnace was heated at a rate of 300 °C h^{-1} in all experiments. Prior to flash sintering, samples were subjected to an isothermal hold at 800 °C in flowing N_2 (0.7 L min^{-1}) for 1 h to carbonise the binder in the powder premix. Afterwards, the furnace ramp continued to a designated furnace temperature. Thirty minutes before

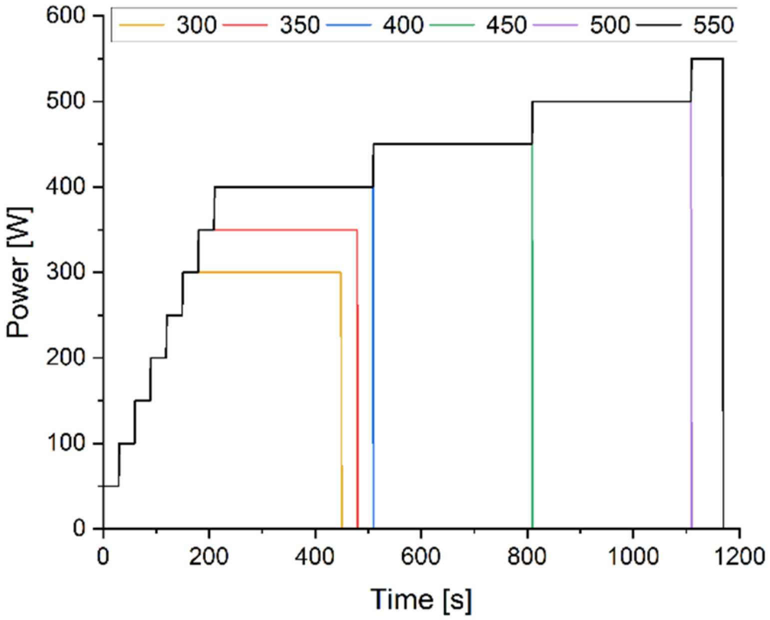

Figure 3.3: Electrical power schedules in isothermal tests.

the electric field was applied across the sample, the gas supply was switched from N_2 to He to ensure an inert sintering atmosphere. The He gas also suppressed plasma formation upon application of the electric field, which occurred in some conditions when N_2 or Ar was used.

The electrical schedules investigated are split into two groups: constant voltage and stepped power experiments. The former experiment is the archetypal flash sintering experiment, whereby a constant voltage is initially applied across the sample in a furnace with gradually increasing temperature. Once the critical temperature was reached and runaway occurred, as described in Section 6.1.1, the furnace temperature was held constant. When the electrical power reached 400 W in these experiments, the power was maintained at this level. For consistency, the furnace temperature at which the power supply switched from voltage to power control was defined as the

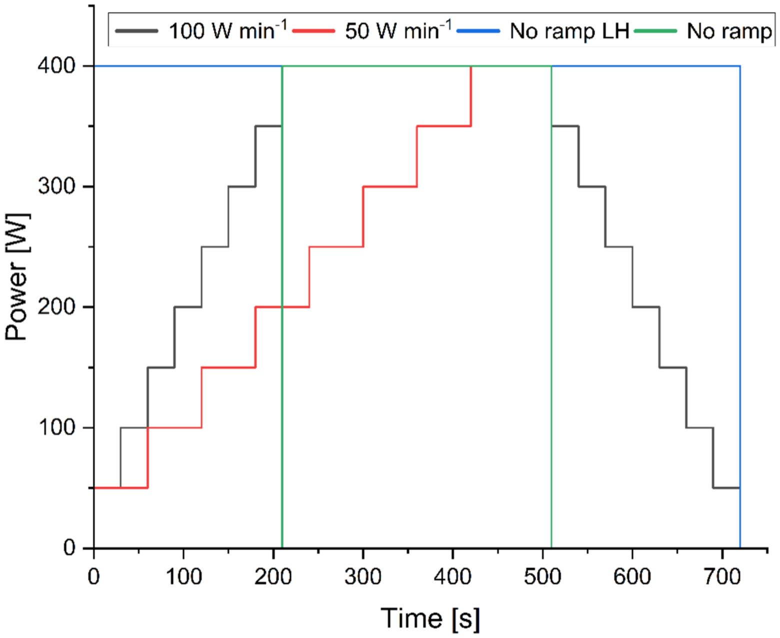

Figure 3.4: Electrical power ramp schedules in isothermal, stepped power tests.

critical furnace temperature.

Differing from the constant voltage experiments, the stepped power tests used a constant furnace temperature while the power was increased in a stepwise manner to the maximum power limit specific to that test. A schematic of the power schedules is shown in Fig. 3.3. The maximum power limits investigated were 300 W, 350 W, 400 W, 450 W, 500 W and 550 W. Those experiments using a 300 W, 350 W and 400 W limit had an average ramp rate of 100 W min^{-1} and an isothermal power hold of 5 min. Using this ramp rate and a furnace temperature of 1500 °C, samples would fracture above a power limit of 400 W. If the electrical heating rate was reduced, this maximum power limit could be extended to 550 W. After 400 W, the rate was dropped to 10 W min^{-1} and ramped up to a maximum of 550 W for 1 min.

Variations of the stepped power experiment were used to investigate the effects that maximum power limit, furnace temperature, hold time and power ramp rate had on sample properties. For all these tests, an average power ramp of 100 W min^{-1} was used. Maximum power limits of 460 W, 430 W and 400 W were used when investigating furnace temperatures of 1200 °C, 1350 °C and 1500 °C, respectively, to maintain similar sample temperatures between all tests. A hold time of 5 min at these power limits was used for all such experiments. Additional hold times were investigated (0.5, 5, 15 and 30 min) using a furnace temperature of 1500 °C and maximum power limit of 400 W. Figure 3.4 shows the stepped power ramp rates that were investigated: stepped power ramp rates that averaged 100 W min^{-1} and 50 W min^{-1}, and then two tests without any power ramp (fastest heating rates). Two hold times were investigated, 5 min and 12 min (referred to as Long Hold ramp rate schedule (LH)). All tests were performed in a furnace at 1500 °C and the maximum power limit reached was 400 W. The only ramp schedule with a ramp down after the hold period was the 100 W min^{-1} profile, for the other schedules, the power simply returned to zero.

The effect of sintering atmosphere was investigated using the 400 W power schedule (Fig. 3.3) and switching to either Ar + 5% H_2, He, RGAr or N_2 after the binder burnout stage.

3.4 Sample temperature estimation

The blackbody radiation model was used to estimate the surface temperature of the sample[136]. The SiC emissivity was taken as 0.85[137]. The high currents required to raise the sample temperature to the sintering temperature of SiC meant that a significant proportion of the electrical power was dissipated in the tungsten wires. To account for this, the energy loss in the wires was measured at the relevant currents and furnace temperatures and subtracted from the total power in the system to deduce the power dissipated in the specimen. Sintering shrinkage of the specimen was measured from video recordings. Both factors were accounted for when calculating sample temperatures and other quantities affected by them. The resistivity of a dense specimen was used to calculate the current required during flash sintering to maintain a constant power per unit of surface area between samples of different thicknesses. This method was used to maintain a similar surface temperature between samples.

3.5 Conventional sintering

Control samples, labelled “fire 1”, were conventionally sintered using the powder manufacturer’s recommended sintering specifications. After the initial carbonisation described in section 3.3, specimens were transferred to a graphite crucible and heated in Ar with a 300 °C h^{-1} ramp to 2200 °C for a 2 h hold before ramping down at the same rate. Additionally, a second conventional heating profile with a shorter hold time and a faster ramp rate was investigated. The green body of the “fire 2” specimen was produced in the same manner as the fire 1 sample, but the heating rate during sintering was increased to 960 °C h^{-1} and the hold time at 2200 °C was limited to 5 min.

3.6 Specimen characterisation

The sample ends were removed, and the resulting cuboids were sectioned on the plane midway between the electrodes (Fig. 3.5a). The edges of the resultant cuboid face are labelled and shown in Fig. 3.5b. SEM images in this work were taken at edge 1, unless otherwise stated.

Six density measurements were made on each specimen half using the Archimedes method, according to ASTM B962 (2017)[138]. All densities are relative to the Theoretical Density (TD) of SiC: 3.21 g cm^{-3} and are given as bulk densities. The relative local density of a sample in each micrograph is different to that of the bulk specimen. There is no quantitative measure of local densities, but a qualitative description is given where required in the appropriate results or discussion sections.

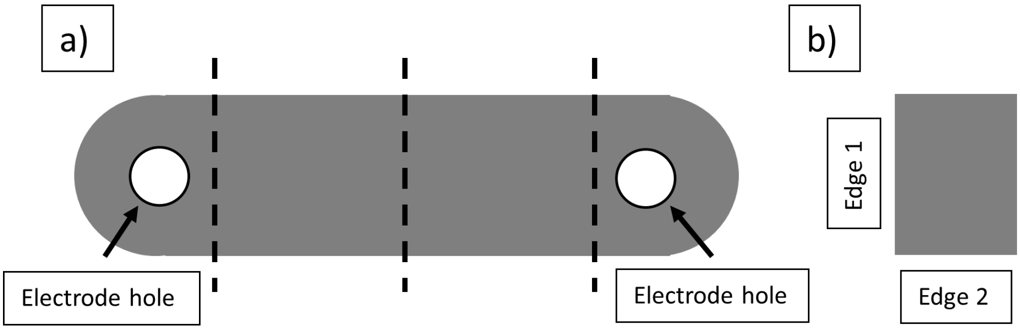

Figure 3.5: a) SiC specimen showing the sectioning lines (dashed) and b) the cross section of the sectioned sample with the labelled edges.

3.6.1 Microstructural analysis

The central cross sections of samples were polished with diamond suspensions down to 1 μm and finished with colloidal silica. Murakami's reagent (3 g potassium hydroxide, 30 g potassium ferricyanide and 60 g water) was used to chemically etch the polished surface; etching was performed at 90 °C for 45 min.

SEM images the surface of a specimen by collecting and analysing a variety of electron signals from an electron beam rastered over the surface of interest[139,140]. The SEM images in this work were captured using A Zeiss Merlin SEM and using the following settings: a working distance of ~5 mm; an accelerating voltage of 5 kV; and a 5 pA current. Samples were coated with ~4 nm of Pt to reduce surface charging. Grain size estimations were made through the linear intercept method (using a multiplier of 1.56), using a minimum of 300 intercepts for each estimation.

EDX in this work was performed at a working distance of 8 mm, an accelerating voltage of 10 kV and a beam current of 200 pA.

XRD data were collected using a Rigaku Miniflex Cu Kα diffractometer operated at 40 kV and 15 mA (0.01 °step, 6 s step^{-1}). Analysis was performed on cross sections of samples before they had been etched. Rietveld refinement was performed using MAUD software[141] and crystallographic phase data taken from The Cambridge Structural Database[142]. To improve the Signal to Noise Ratio (SNR) of the raw XRD data, the spectra were smoothed using the adjacent averaging function on Origin software[143], but the low SNR of the scans in this work resulted in relatively high weighted profile R-factor values, R_{wp} (all were less than 25).

The process of Rietveld refinement involves fitting a function to a set of peaks/ reflections that represent the characteristic scattering angles and intensities of a given crystallographic lattice. The relative height and position (scattering angle) of these peaks can be found in crystallographic databases. The resultant function is then compared with the raw XRD scan taken of the surface of the specimen to be examined. A least squares approach is used to minimize the difference between the data points of the function and the scan. Low residual errors of the fit then give confidence that the crystallographic lattice under investigation is present in the material. The key benefit of Rietveld analysis in this work is that allows the relative amounts of different constituent elements in the sample to be approximated.

Atom Probe Tomography (APT) was performed by Dr Jaspreet Singh. A full description of the atom probe diagnostic settings can be found in his thesis[144], but the main operating conditions are given in Table. A.5. Bulk clustering analysis was performed on SiC tips that were taken from the centre of grains in samples produced using both conventional sintering schedules (fire 1 and 2) and two flash sintering heating schedules (550 W with carbon discs and foil, section 3.2.2, and a 400 W schedule with a ramp rate of 50 W min^{-1}, section 3.3). The Gibbsian excess of grain boundaries in SiC samples were calculated from APT data in accordance with the work of Jenkins[145], adapted from that of Hellman[146].

3.6.2 Mechanical characterisation

Three equally spaced Vickers hardness indentations were made near the centre of the cross-sections using a 5 kgf load using a Future Tech Vickers Hardness Tester Model 110B, Japan. The samples were reground sufficiently to remove the first row of indents and the damage beneath them (approximately 1.5 mm), polished and indents were made a second time for a total of six indents per specimen. Vickers Hardness was calculated using Eqn. 3.1[147,148].

$$HV = 1.8644\frac{L}{d^2} \tag{3.1}$$

where d is the average length of the indent diagonals, and L is the load applied by the indenter on the sample's surface.

Bar shaped specimens that were used in the 3-point bend strength and toughness tests were made from three sets of specimens: conventionally sintered fire 1 and 2 sets, and an optimised flash sintered set (550 W, C discs and foil, section 3.2.2). A set of five samples was made for each strength estimation and sets of three for the toughness tests. Specimens were cut and ground into bars approximately 1.0 mm x 1.5 mm x 15.0 mm and then polished to a 1 μm finish. Notches were made in the specimens for the SEVNB toughness tests by first sawing a shallow guide notch in the centre of each specimen's length. A secondary, sharper notch was then made in this guide notch by using a steel razor blade coated with diamond slurry that was made progressively finer (beginning at 9 μm down to 1 μm with the blade replaced as the slurry became finer). Due to the small size of the samples and the brittle and hard nature of SiC, the edges of the samples were not chamfered. Both strength and toughness tests were performed using a 3-point bend test rig with a 12 mm span, which was mounted in a Shimadzu AGS-X Universal Test Frame. A loading rate of 0.5 mm min^{-1} was used for all tests. The flexural strength of each specimen was calculated using Eqn. 3.2[149].

$$\sigma = \frac{3F_m l}{2bh^2} \tag{3.2}$$

where F_m is the maximum force applied, l the support span, b the width of the test piece and h, its height. The stress intensity factor for a SEVNB in 3-point bending is given by Eqn. 3.3 (ASTM C1421-18139):

$$K_I = \frac{F_m l}{bh^{3/2}} f(\frac{a}{h}) \tag{3.3}$$

where K$_I$ is the stress intensity factor, F_m is the maximum load, l is the span of the rig, b is the width of the specimen and h its height, and $f(a/h)$ is a dimensionless correction factor:

$$f(\frac{a}{h}) = \frac{3(\frac{a}{h}^{1/2})(1.99 - \frac{a}{h}(1 - \frac{a}{h})(2.15 - 3.93\frac{a}{h} + 2.7(\frac{a}{h})^2)}{2(1 + 2\frac{a}{h})(1 - \frac{a}{h})^{3/2}} \tag{3.4}$$

The critical flaw size was calculated using Eqn. 3.5, assuming a semi-circular edge crack (Eqn. 3.6) and α value of 1.12.

$$K_I = \phi \sigma \sqrt{c} \tag{3.5}$$

$$\phi = \alpha \frac{2}{\sqrt{\pi}} \tag{3.6}$$

where $\mathrm{K}_I c$ is the critical stress intensity factor for a given critical flaw size c, ϕ is a geometrical form factor, determined from the shape of the crack and alpha from the semi-circular edge-shape of the crack, and σ, the flexural strength.

3.7 Estimation of experimental uncertainty

The standard errors associated with density, grain size, hardness, strength, and toughness measurements were estimated from statistical distributions associated with the measurements collected in this work. Those associated with sample temperature, resistivity and critical field strength were estimated from the systematic and statistical errors associated with the electrical measurements, furnace temperatures, shrinkage from video recordings and the uncertainty in emissivity.

Chapter 4

Effect of flash sintering parameters on the densification and microstructure of silicon carbide

This chapter presents the broad, systematic analysis of how each flash sintering parameter (defined in Chapter 3) affected the density and microstructure of SiC. It then discusses their influence in terms of the thermal effect of the electrical current, thermal gradients with the sample and the impact of sintering atmosphere during flash sintering. It also defines the optimum flash sintering schedule (in terms of density and microstructure) that was used to create samples for mechanical and electrical comparisons with conventionally sintered SiC (Chapters 5 and 6).

4.1 Results

4.1.1 Effect of power limit

4.1.1.1 Densification

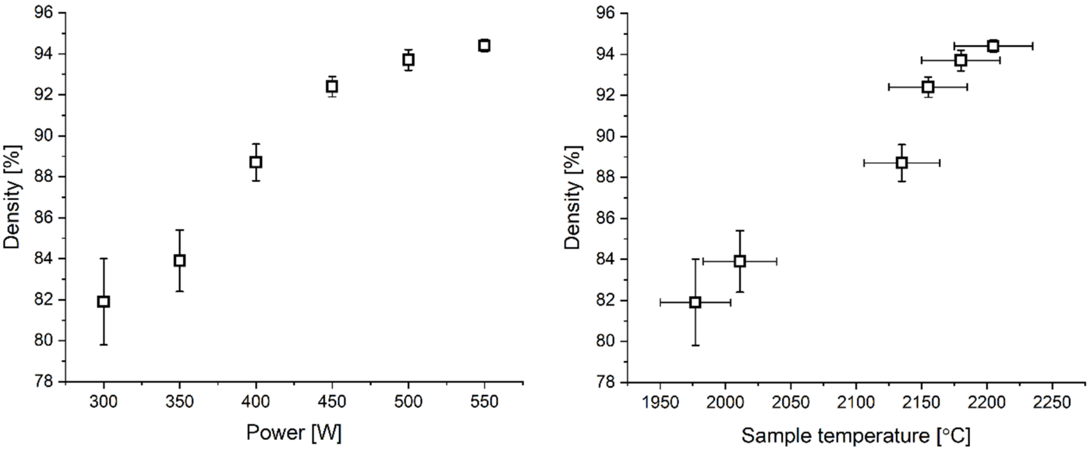

Figure 4.1: Final sample density against a) nominal power limit and b) maximum sample temperature (corrected for power in wires). The furnace temperature was 1500 °C and power schedules are shown in section 3.3.

Figure 4.1 shows the effect of electrical power limit and resulting sample temperature on sample density at various stages throughout the heating schedule. Increasing the power limit from 300 W to 400 W increased the relative density from approximately 80% to 90%. Increasing sample temperatures beyond this power limit resulted in higher densities still, up to a maximum of 94.4 % ± 0.3 % with specimen temperature of 2205 °C ± 28 °C. Exceeding 550 W or holding this limit for longer than 1 min resulted in sample fracture.

4.1.1.2 Microstructure

Measurement	300 W	350 W	400 W	450 W	500 W	550 W
G_{av}(μm) [Centre]	2.0 ± 0.1	2.4 ± 0.1	3.1 ± 0.1	3.9 ± 0.2	5.3 ± 0.3	5.9 ± 0.5
G_{av}(μm) [Edge]	1.7 ± 0.1	1.9 ± 0.1	2.6 ± 0.1	3.3 ± 0.2	4.8 ± 0.2	5.2 ± 0.2
Gav (μm) [Edge2]						2.1 ± 0.1

Table 4.1: Effect of power limit on specimen grain sizes. (Edge 2 data only available for the 550 W specimen.)

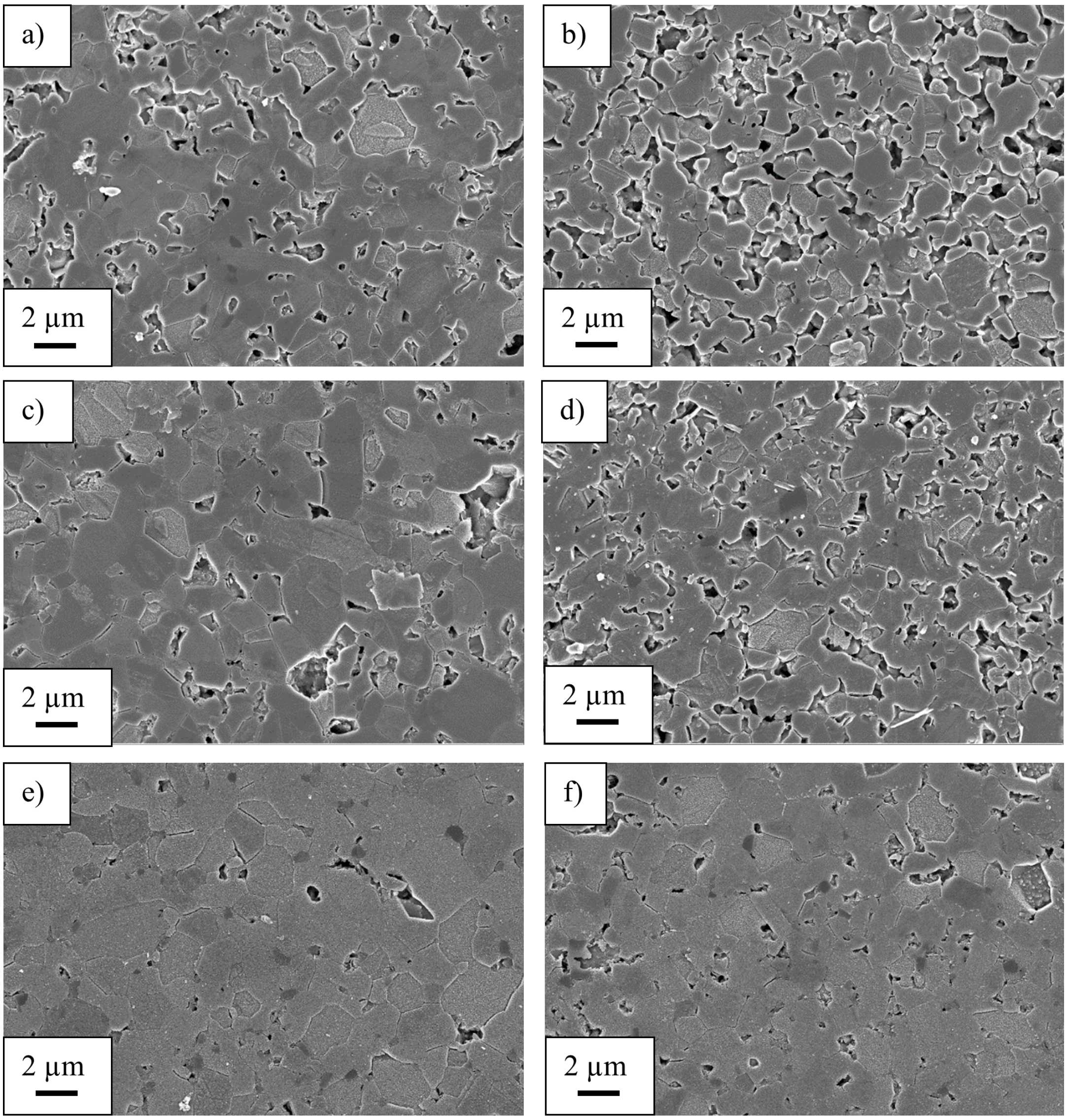

Figure 4.2: SEM images of samples produced with different power schedules (section 2.3). Left column images are taken of the centres of the specimens and right column images of the samples' edges. A sample produced with a 300 W limit is shown in a) and b); 350 W in c) and d); 400 W in e) and f

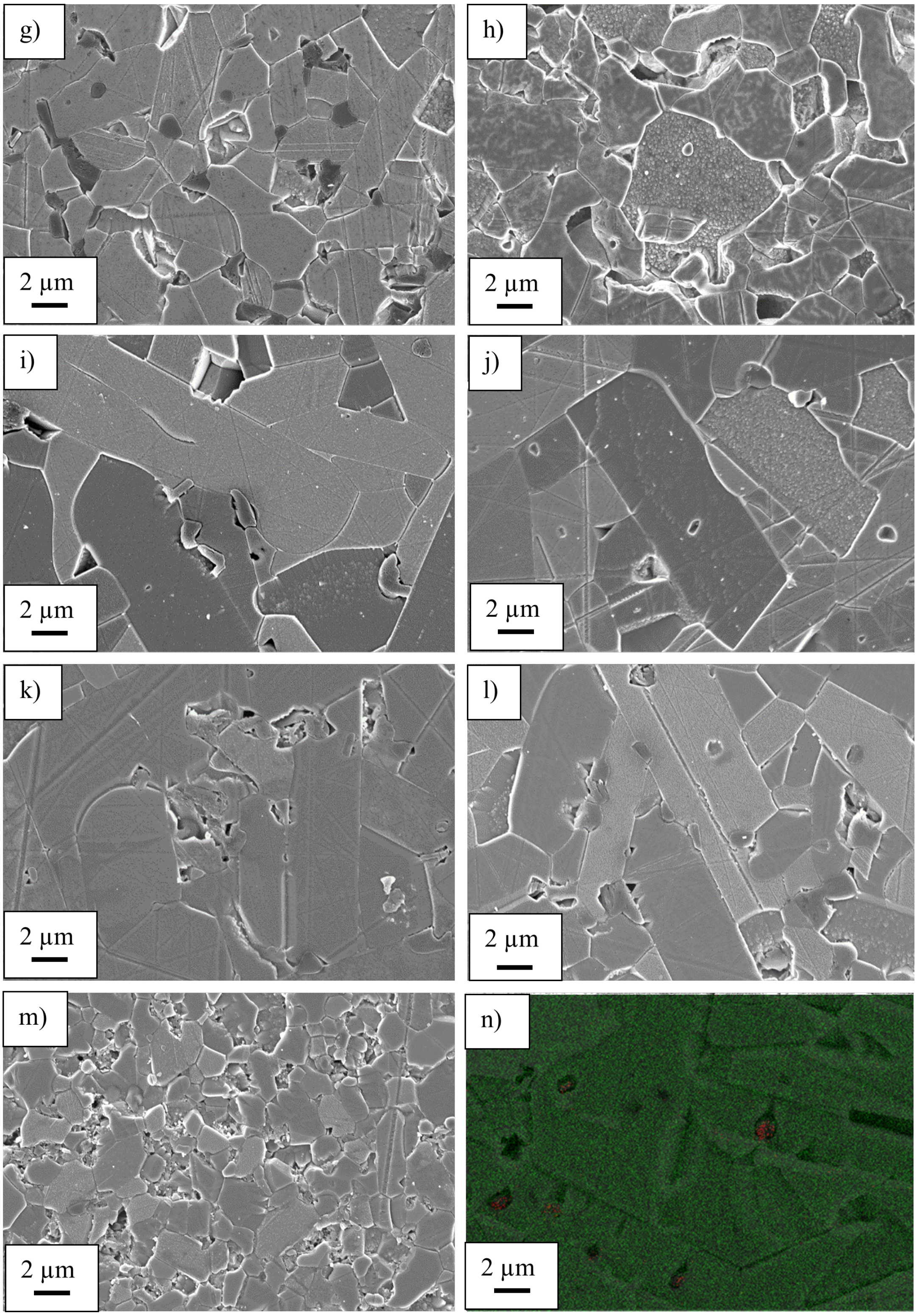

Figure 4.3: A sample produced with a 450 W limit is shown in g) and h); 500 W in i) and j); 550 W in k) and l); the bottom edge (facing the bottom of the furnace, edge 2) of the 550 W specimen in m) and an EDX map of a 550 W sample (C is indicated in red and Si in green).

Figs. 4.2 and 4.3 show micrographs taken of the centre and edge of specimens that were heated to a range of maximum power limits; starting from 300 W to 550 W. The figures show that increasing the electrical power dissipated within the sample increased the average grain size and qualitatively decreased porosity at the centre and at the edge of the specimen. Grain size measurements from these specimens are given in Table 4.1. The largest grain sizes were measured from the sample produced at the highest power (550 W, 5.9 µm ± 0.5 µm and 5.2 µm ± 0.2 µm at the centre and edge 1, respectively); the smallest grain sizes from the sample produced at the lowest (300 W, 2.0 µm ± 0.1 µm and 1.7 µm ± 0.1 µm at the centre and edge, respectively). The average grain size at edge 2 of the sample that was produced with the 550 W heating schedule was significantly smaller than the grain size at edge 1 of the sample (5.2 µm ± 0.2 µm vs 2.1 µm ± 0.1 µm, respectively). The edges nomenclature is defined in section 3.1. For all tests, grain sizes at the edge of the specimens were smaller than those in the centre. Carbon rich pores and inclusions are indicated as red points in Fig. 4.3n; Si is shown in green. The EDX map is from an area on the polished surface of a 550 W specimen, but C rich pores and inclusions were a feature of all specimens. Grain growth was limited in samples produced using low power tests (300 W – 400 W) and grains are fine and equiaxed. As the power and sintering time were increased (450 W - 550 W), the grains became larger and elongated.

4.1.1.3 XRD Analysis

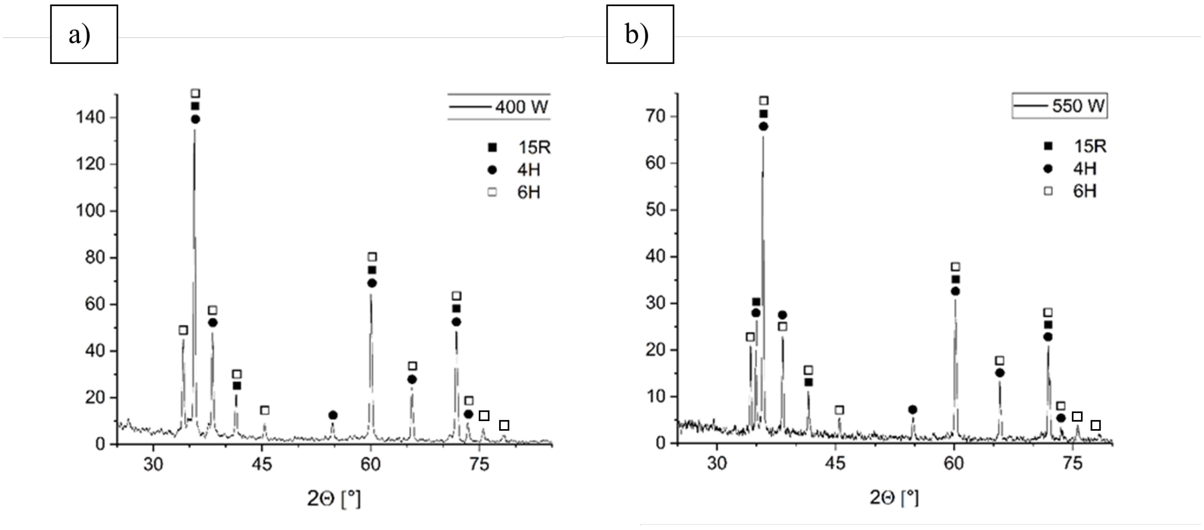

Figure 4.4: XRD scans of samples produced using the a) 400 W and b) 550 W heating schedules (section 3.3).

From Fig. 4.4, the XRD spectra show typical SiC peaks in both samples. The Rietveld analysis results in Table 4.2 indicate that the 6H polytype was the most prevalent polytype in both samples, but that increasing the power limit (and therefore sample temperature, Fig. 4.1) during flash sintering from 400 W to 550W resulted in a significant increase in the abundance of the 4H polytype.

Sample	6H (%)	4H (%)	15R (%)
400 W	92.3 ± 1.1	1.9 ± 0.5	5.8 ± 0.8
550 W	78.4 ± 1.4	18.3 ± 0.6	3.3 ± 0.4

Table 4.2: Effect of power limit on final polytypic composition of flash sintered SiC.

4.1.1.4 Sample fracture

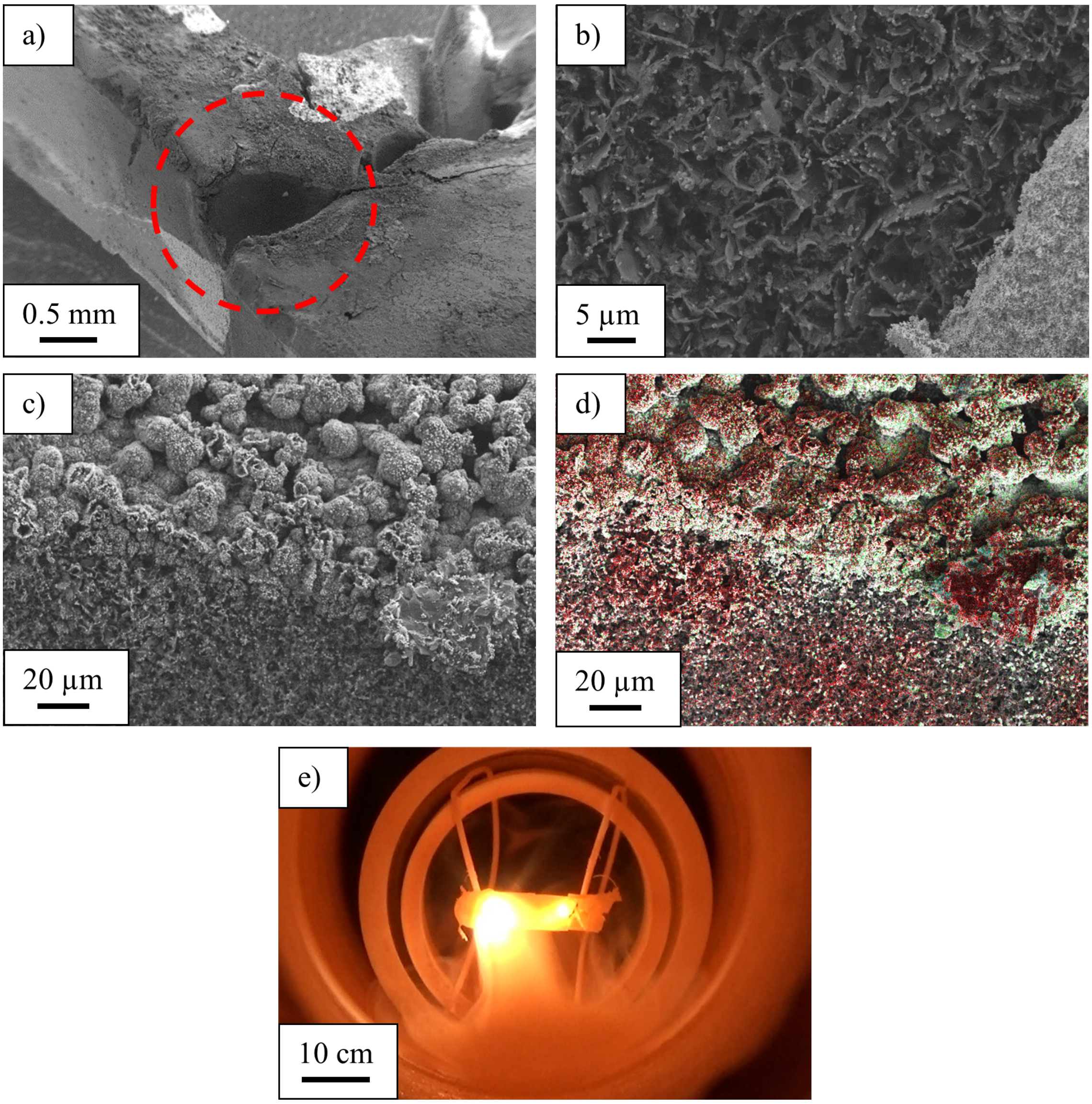

Figure 4.5: a) SEM image of a SiC sample mid "fracture", the hole indicated in the red circle is where the vapours were ejected from, b) shows the C structure inside the hole, c) and d) show the boundary between the hole and the surface and the complementary EDX map, respectively; C is indicated in red, Si in green; (e) a still from a video during fracture

If the SiC sample was heated above 2205 °C (power limits greater than 550 W), vapour would be ejected from the volume of the sample nearest the electrodes (Fig. 4.5a and 4.5e) and if left for a long enough period, sufficient material would be ejected such that the sample would fracture. The hole left in a sample that was heated beyond 2205 °C (but which was cooled before the sample could fully fracture) is shown in Fig. 4.5a. The structures of the materials that are left around the hole are shown in Fig. 4.5b and 4.5c. The EDX map of the boundary shown in Fig. 4.5d indicates that there was a Si deficiency in the hole, where a flaky C rich was observed.

4.1.2 Effect of ramp rate

4.1.2.1 Densification

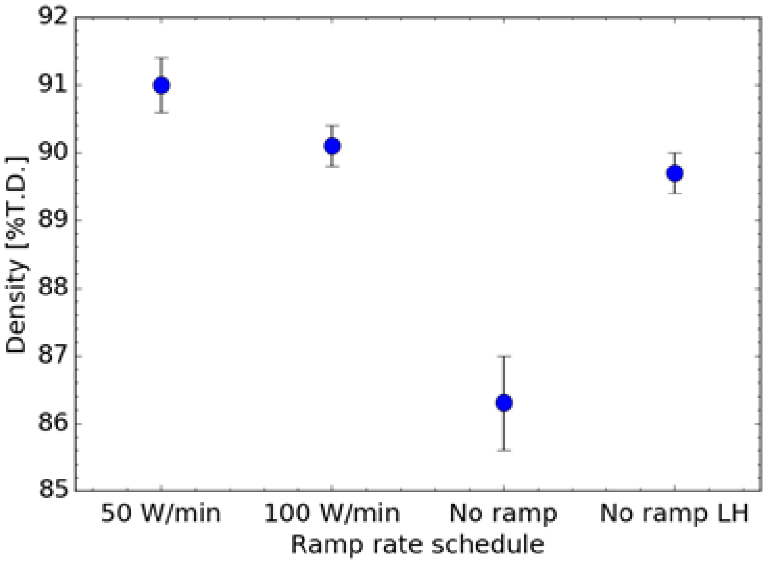

Figure 4.6: Dependence of sample density on power ramp rate at a furnace temperature of 1500 °C, and a maximum power limit of 400 W (section 3.3).

The effect of power ramp rate schedule (section 3.3) on specimen density is shown in Fig. 4.6. Bulk density increased with decreasing ramp rate. The sample produced with no power ramp, i.e. the fastest heating rate, had the lowest density (86.3% ± 0.5%) and the sample produced with the slowest ramp rate had the highest density at

91.0% ± 0.4%. The samples produced using slower ramp rate schedules spent longer times at sintering temperatures than those with slower ramp rates. Using no ramp but extending the hold time to 8.5 min (No ramp LH, section 3.3) increased sample density to within experimental uncertainty of the 100 W min^{-1} sample, which also had a total schedule time of 8.5 min.

4.1.2.2 Microstructure

Figure 4.7 shows SEM images taken of the centre and the edge of specimens produced using different ramp rate schedules (section 3.3). Porosity is observed in all images and grain sizes are fine and equiaxed. As shown in Table 4.4, grain sizes at both the centre and the edge of specimens increased by using slower ramp rates. The smallest grain sizes were measured from the sample produced with no ramp (fastest heating) (2.5 µm ± 0.1 µm and 1.8 µm ± 0.1 µm at the centre and edge, respectively). If the same heating rate is used but the hold time is extended (No ramp (LH)), grain sizes increased in the centre and the edge of the specimen, to within experimental error of 100 W min-1 specimen. The largest grain sizes were measured from the 50 W min^{-1} sample (3.3 µm ± 0.2 µm and 2.2 µm ± 0.1 µm at the centre and edge, respectively). For all tests, grain sizes at the edge of the specimens were smaller than those in the centre.

	50 W min^{-1}	100 W min^{-1}	No ramp	No ramp (LH)
G$_{av}$(μm) [Centre]	3.3 ± 0.2	2.9 ± 0.1	2.5 ± 0.1	3.0 ± 0.1
G$_{av}$(μm) [Edge]	2.2 ± 0.1	2.0 ± 0.1	1.8 ± 0.1	2.1 ± 0.1

Table 4.3: Effect of ramp rate on average grain size at the specimen's centre and edge.

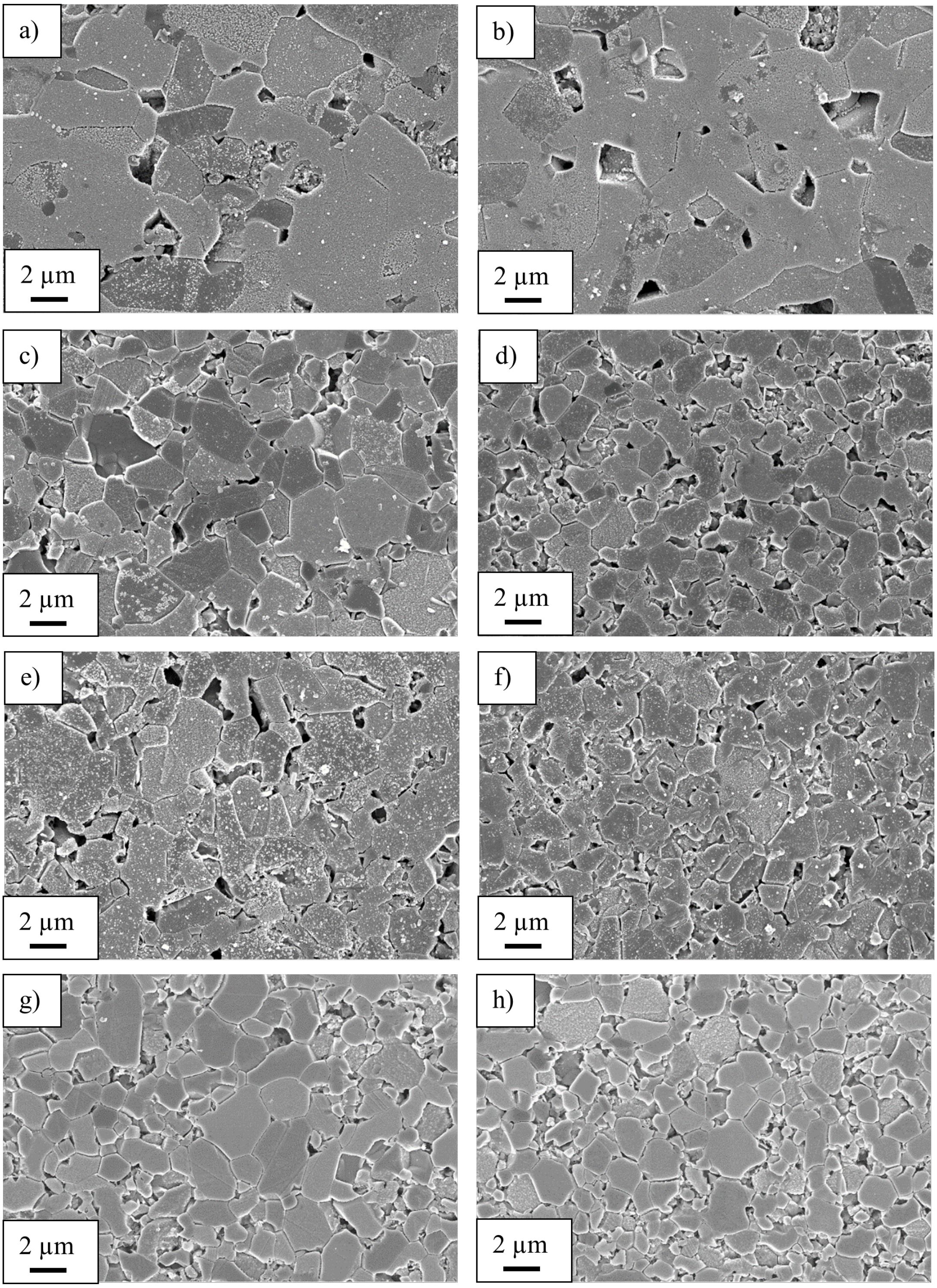

Figure 4.7: SEM images of samples produced using different power ramp rates (section 3.3). Left column images are taken of the centres of the specimens and right column images of the samples' edges. A sample produced with a ramp rate of 50 W min^{-1} is shown in a) and b); a ramp rate of 100 W min^{-1} in c) and d); no power ramp (fastest heating) and a hold time of 5 min in e) and f) and again without a power ramp but with a 12 min hold in g) and h).

4.1.3 Effect of hold time

4.1.3.1 Densification

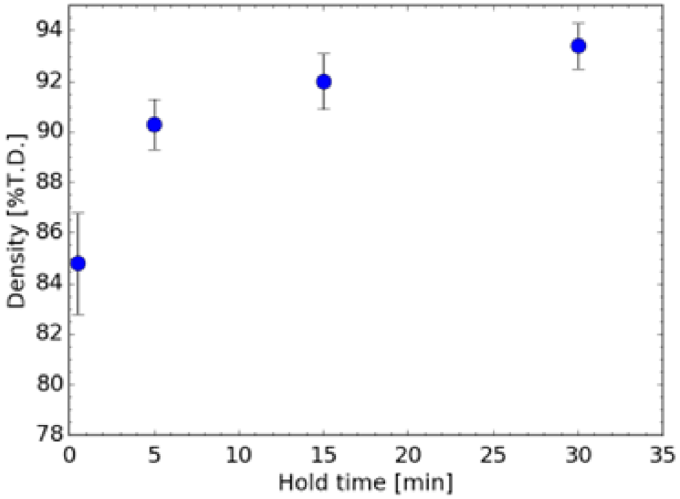

Figure 4.8: Relative density against hold time with a furnace temperature of 1500 °C and a power limit of 400 W (section 3.3).

Figure 4.8 shows how relative density varies with hold time. The power followed the 400 W stepped heating schedule (section 3.3). Longer sintering times increased the density, although the effect of longer hold times reduced as higher densities were reached. The lowest recorded density was 84.8% ± 2.0% for a hold time of 0.5 min, which increased to 93.4% ± 0.9% for a 30 min hold time.

4.1.3.2 Microstructure

	0.5 min	5 min	15 min	30 min
G_{av}(μm) [Centre]	1.5 ± 0.1	2.9 ± 0.1	3.3 ± 0.2	3.4 ± 0.2
G_{av}(μm) [Edge]	1.3 ± 0.1	2.0 ± 0.1	2.2 ± 0.1	2.4 ± 0.1

Table 4.4: Effect of hold time on average sample grain size.

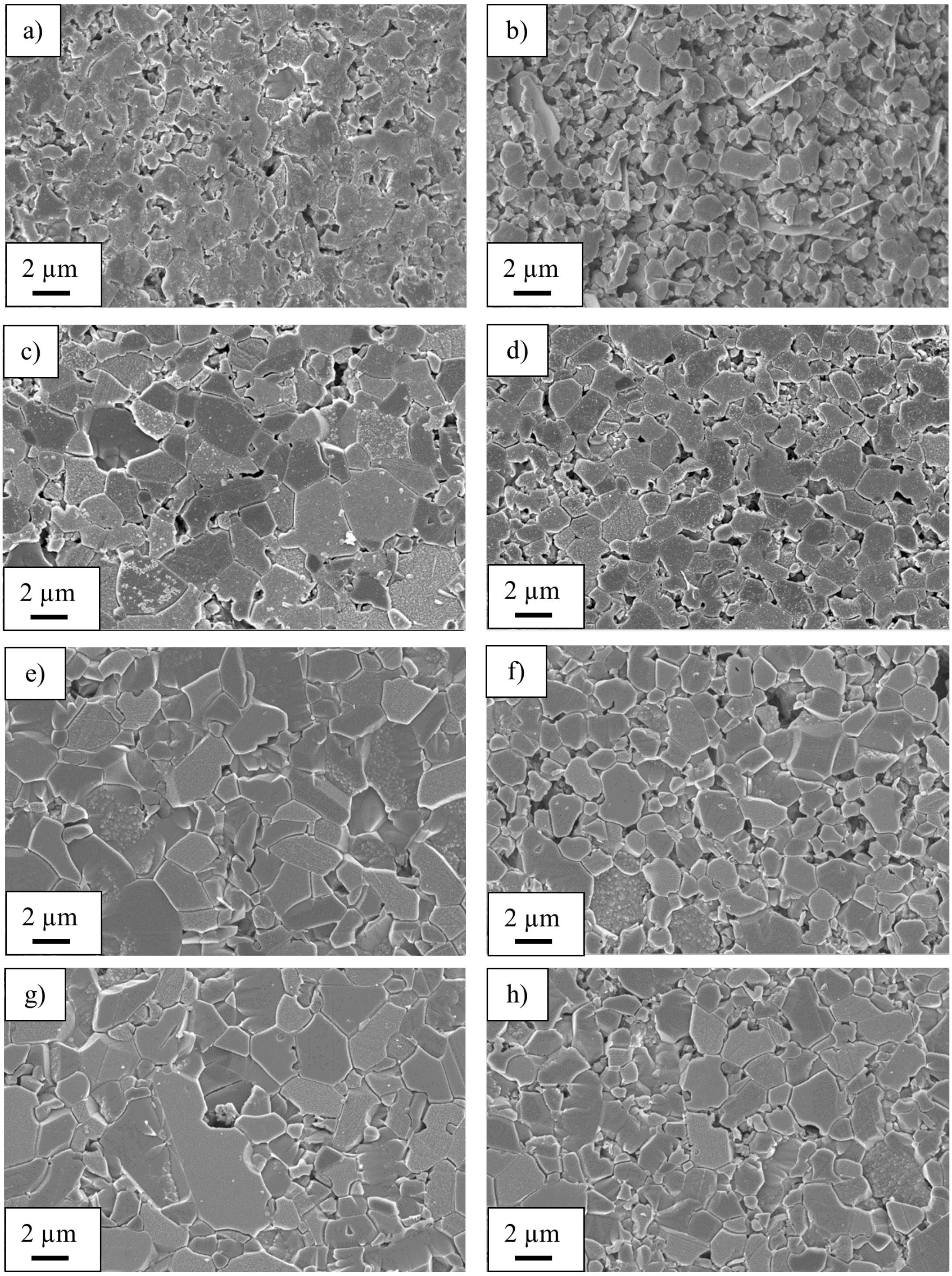

Figure 4.9: SEM images of samples produced with similar sample temperatures but different hold times (section 3.3). Left column images are taken of the centres of the specimens and right column images of the samples' edges. A sample produced in 0.5 min is shown in a) and b); 5 min in c) and d); 15 min in e) and f); 30 min in g) and h).

Table 4.4 shows that grain sizes at both the centre and the edge of specimens increased by using longer hold times. However, the effect of longer hold times on average grain size diminished as higher densities were reached. For all tests, grain sizes at the edge of the specimens were smaller than those in the centre.

Figure 4.9 shows SEM images taken of the centre and the edge of specimens produced using different hold time schedules (section 3.3). Little densification occurred at the edge of the 0.5 min test (Fig. 4.9b). Porosity is observed in all images in Fig. 4.9. Grain sizes are fine and equiaxed for all tests bar the last, the 30 min sample, where some elongated grains were seen in the centre of the specimen (Fig. 4.9g).

4.1.4 Effect of furnace temperature

4.1.4.1 Densification

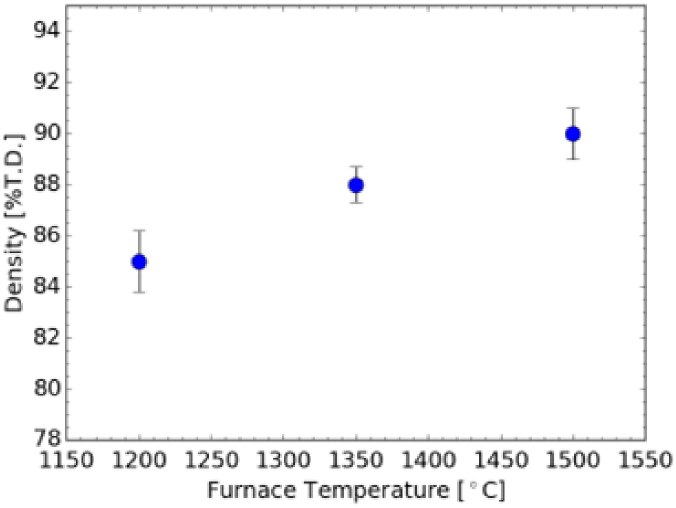

Figure 4.10: Relative density against furnace temperature for a hold time of 5 min and a constant specimen temperature of ~2135 ° C (section 3.3).

All samples in the furnace temperature tests (Fig. 4.10) had similar sample temperatures (~2135 °C). Despite this, Fig. 4.10 indicates that sample density increased with furnace temperature, from 85.0% ± 1.2% at a furnace temperature of 1200 °C to 90.1% ± 1.0% at 1500 °C.

4.1.4.2 Microstructure

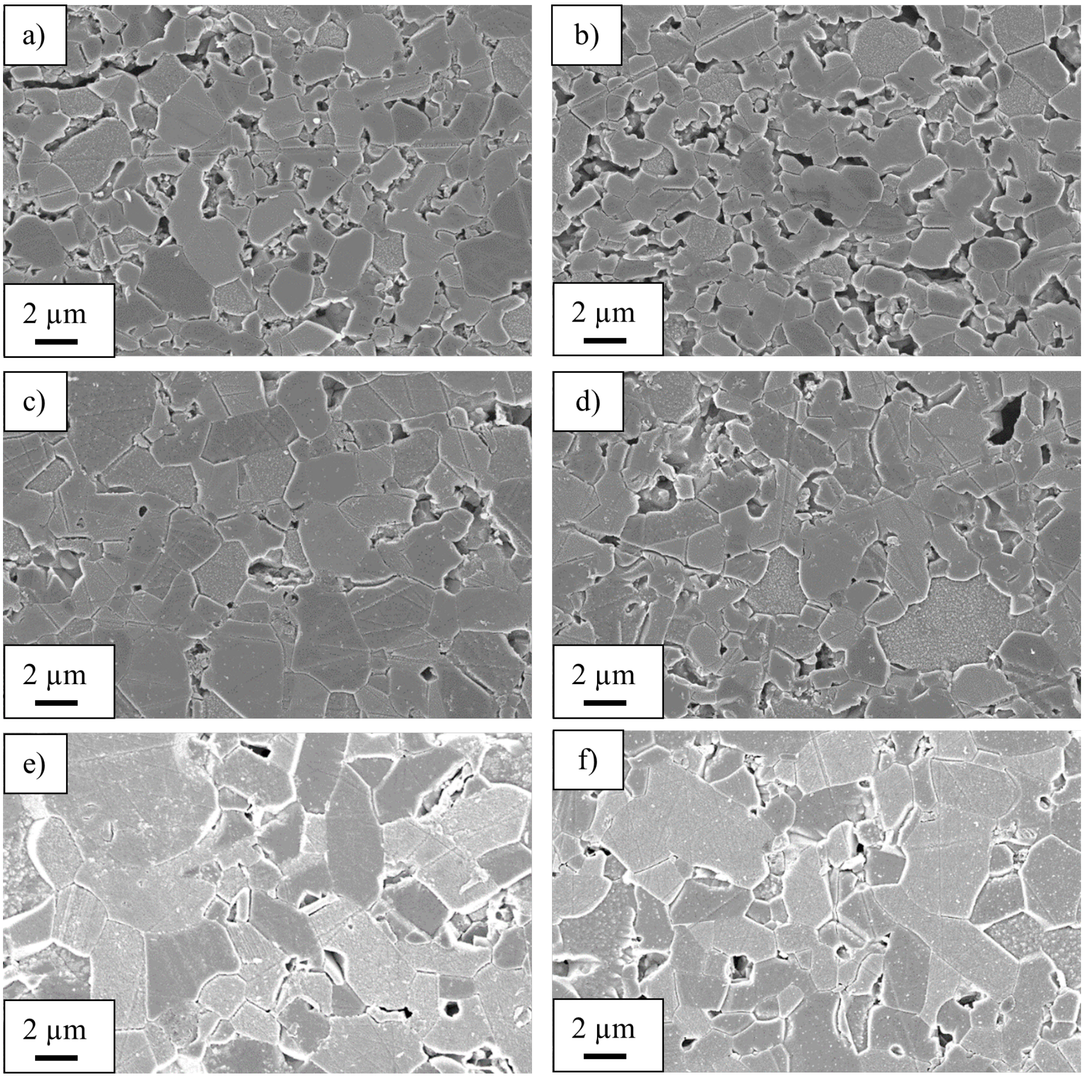

Figure 4.11: SEM images of samples produced with similar sample temperatures but different furnace temperatures. Left column images are taken of the centres of the specimens and right column images of the samples' edges. A sample produced in a furnace at 1200 °C is shown in a) and b); at 1350 °C in c) and d); at 1500 °C in e) and f).

	1200 °C	1350 °C	1500 °C
$G_{av}(\mu m)$ [Centre]	2.0 ± 0.1	2.5 ± 0.1	3.3 ± 0.2
$G_{av}(\mu m)$ [Edge]	1.5 ± 0.1	1.9 ± 0.1	2.2 ± 0.1

Table 4.5: Effect of furnace temperature on average specimen grain size.

The SEM images in Fig. 4.11 shows the effect of furnace temperature (section 3.3) on specimen microstructure at the centre and the edge of the sample. Porosity is observed in all samples, but it decreased as the furnace temperature was increased. Grains are fine and equiaxed at both the centre and the edge of the 1200 °C and 1350 °C samples but become slightly elongated in the 1500 °C specimen.

From Table 4.5, the smallest grain sizes were measured from the sample produced at a furnace temperature of 1200 °C and sizes increased with increasing furnace temperature.

4.1.5 Effect of insulation

4.1.5.1 Types of insulation

4.1.5.1.1 Densification results

Figure 4.12 shows how different types of insulation affected bulk sample density. The highest density achieved was 94.4% ± 0.3% when no insulation was used and the lowest was 82.2% ± 1.2% by the sample insulated by C felt. Out of the samples produced with insulation, the highest density was achieved by using the mirror set up with C discs (mirror 2) at 93.5% ± 0.5%.

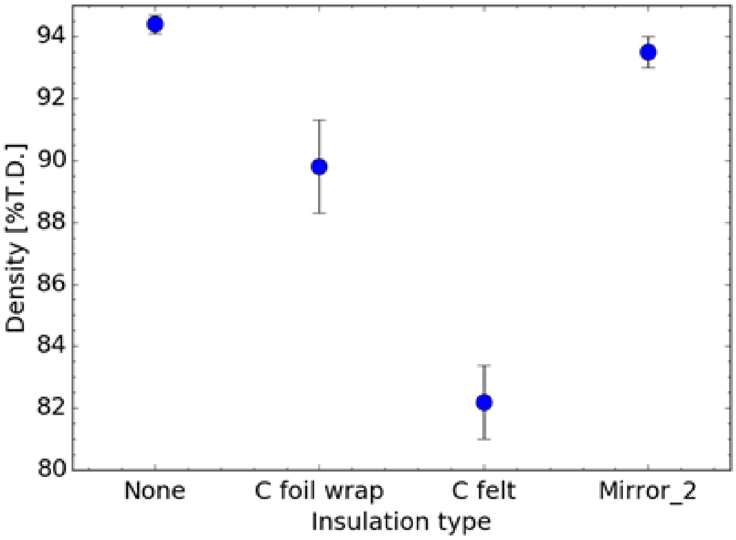

Figure 4.12: The effect of insulation type on sample density. Samples were produced using the 550 W heating schedule (section 3.3) and at a furnace temperature of 1500 C and surrounded with different insulating materials. Mirror 2 set up consisted of mirror sounding the sample which were mounted on C discs.

4.1.5.1.2 Microstructural results

Figure 4.14 shows the effect of different insulation on sample microstructure. Large, elongated grains are present in all samples. All insulations increased the average grain size in the centre of all samples above those measured from the sample produced with no insulation. Using C felt and C foil also increased grain sizes (Table 4.6) at the edge of the specimen. Although mirror 2 set up (with C discs) did increase the average grain size at the centre of the sample, it decreased the sizes at the edge of the specimen, compared to a sample produced without insulation. There was no grain size gradient between the centre and the edge of the sample produced with C foil wrap. The largest

	No insulation	C foil wrap	C felt wrap	Mirrors (no foil)
$G_{av}(\mu m)$ [Centre]	5.9 ± 0.5	6.0 ± 0.4	12.4 ± 1.4	6.6 ± 0.5
$G_{av}(\mu m)$ [Edge]	5.2 ± 0.2	6.0 ± 0.5	9.8 ± 0.7	4.4 ± 0.2

Table 4.6: Effect of insulation on average specimen grain size.

grains were measured from the centre of the C felt sample (12.4 µm ± 1.4 µm) and the smallest from the edge of the specimen produced with mirror 2 set up, at 4.4 µm ± 0.2 µm. It should be noted that when the C foil was wrapped too tightly around the sample, the specimen fractured. This was only observed when using C foil.

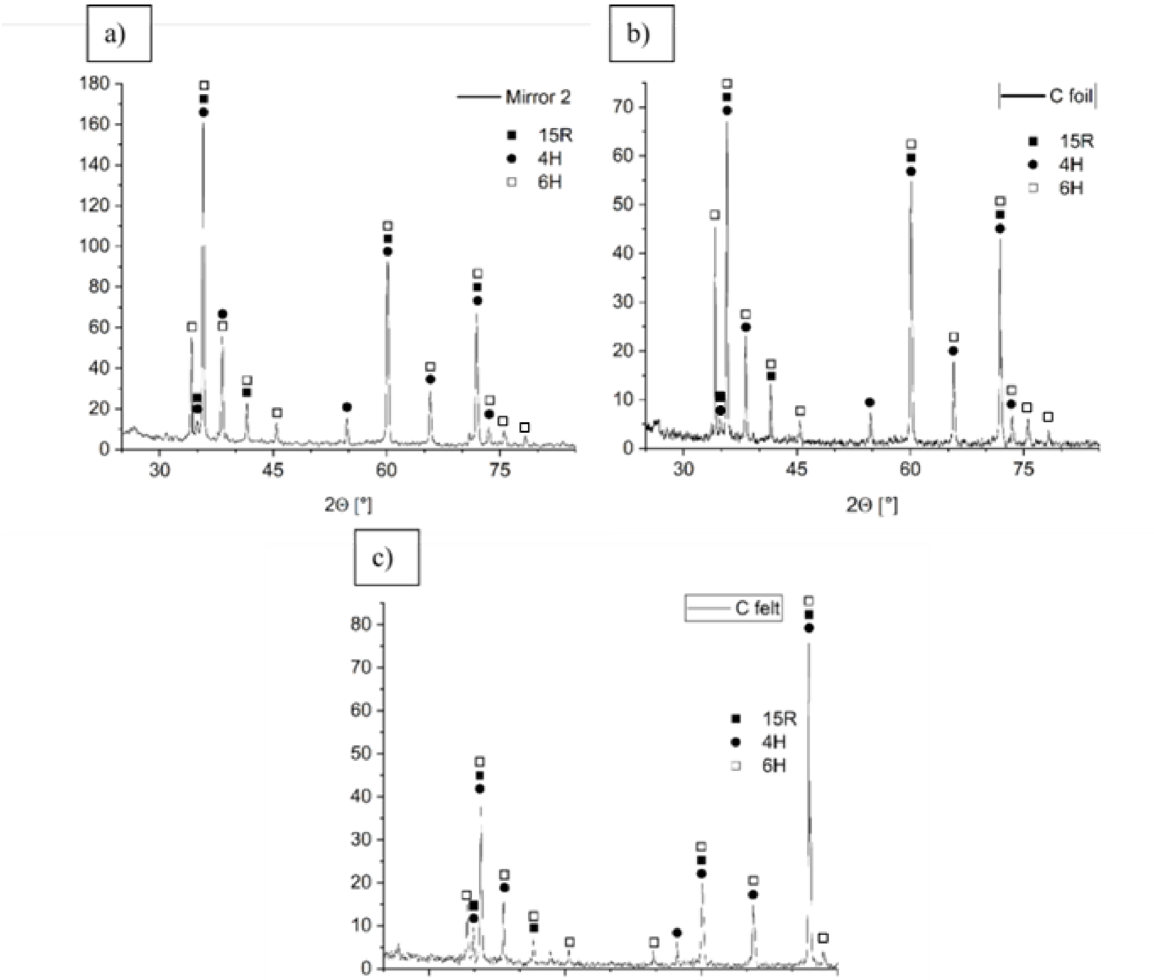

Figure 4.13: XRD spectra of SiC samples flash sintered with a) mirror 2 set up, b) the C inlet foil wrap and c) the C felt wrap.

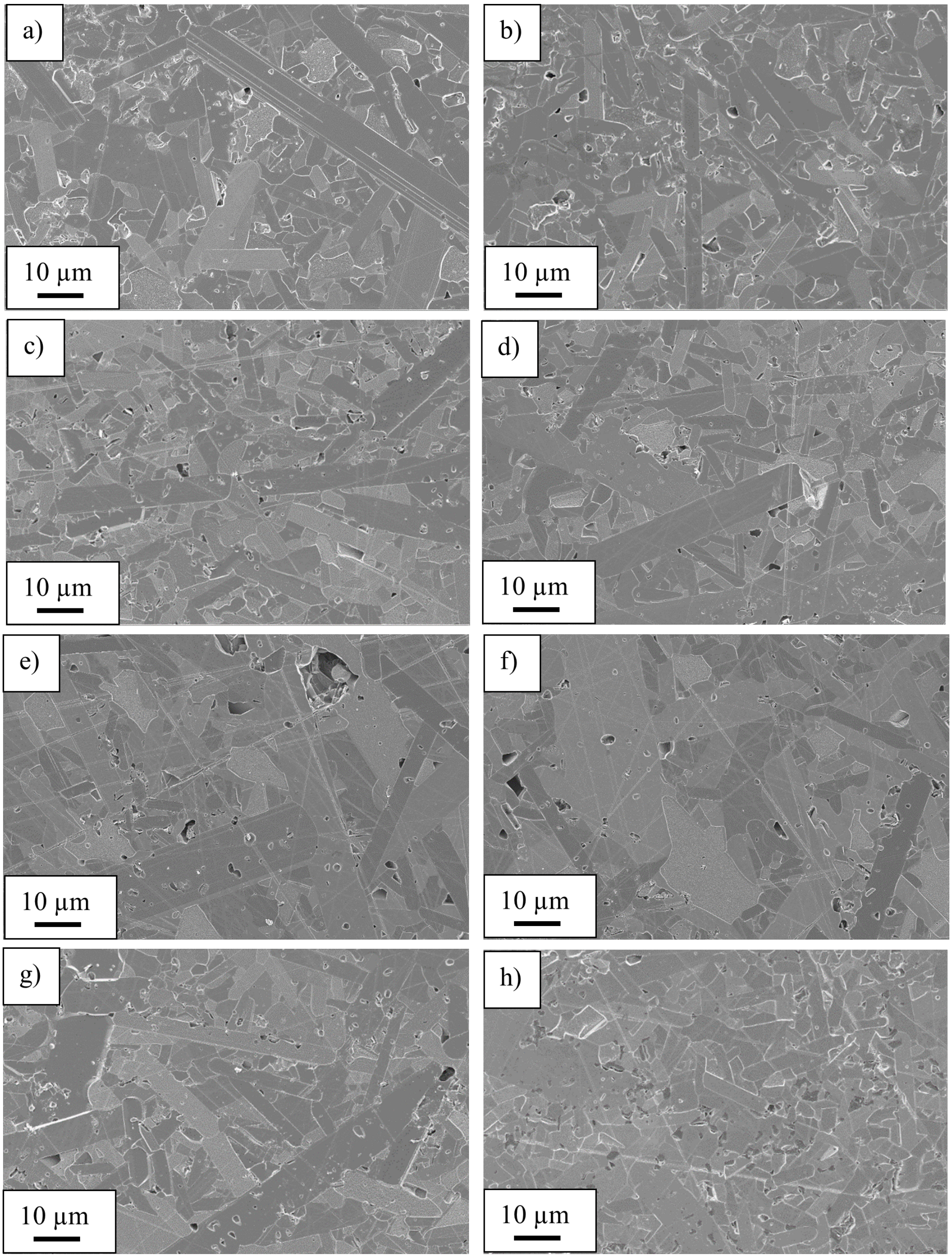

Figure 4.14: SEM images of sample produced at 550W with different insulations (section 3.2.2). Left column images are taken of the centre of the specimens and right column images of the samples' edge. No insulation is shown in a) and b); C foil is shown in c) and d); C felt is shown in e) and f); mirror 1 (no foil) is shown in g) and h).

	6H (%)	4H (%)	15R (%)
Mirror 2	86.5 ± 0.8	7.4 ± 0.4	6.2 ± 0.4
C foil wrap	89.8 ± 1.0	6.5 ± 0.4	3.7 ± 0.4
C felt wrap	74.0 ± 0.9	24.1 ± 1.4	1.9 ± 0.7

Table 4.7: Effect of insulation on SiC polytype composition in flash sintered samples.

The XRD spectra of SiC specimens that were flash sintered with different forms of insulation are shown in Fig. 4.13, with the corresponding Rietveld analysis in Table 4.7 showing polytypic concentrations of each sample. The differences in peak heights between spectra indicate that the different types of insulation may have influenced crystal structure; the Rietveld analysis suggests that the C felt led to a large amount of the 4H polytype in the specimen (∼25%). However, these anomalous spikes could be an artefact that arose from a small fraction of abnormal grains in a larger volume of finer grains[150]. The large area of these grains might reflect more of a specific bragg peak than the surrounding matrix of randomly orientated fine grains, and hence the large grains may have disproportionally contributed to the scans shown in Fig. 4.13.

4.1.5.2 Furnace carbon additions

4.1.5.2.1 Densification

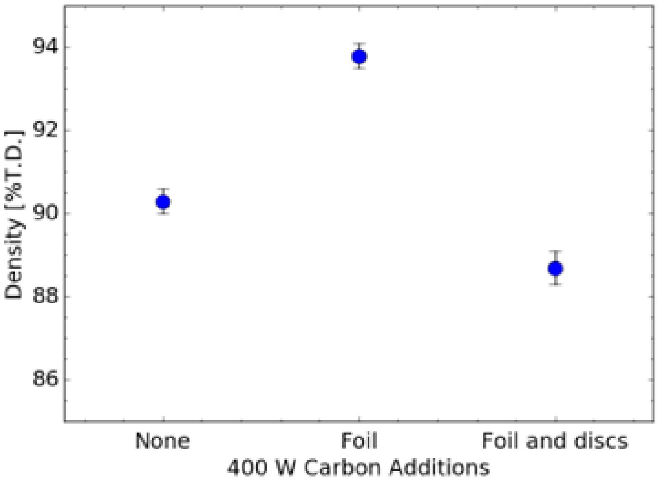

Figure 4.15: Effect of C impurities, following the 400 W heating schedule and C additions (Section 3.3).

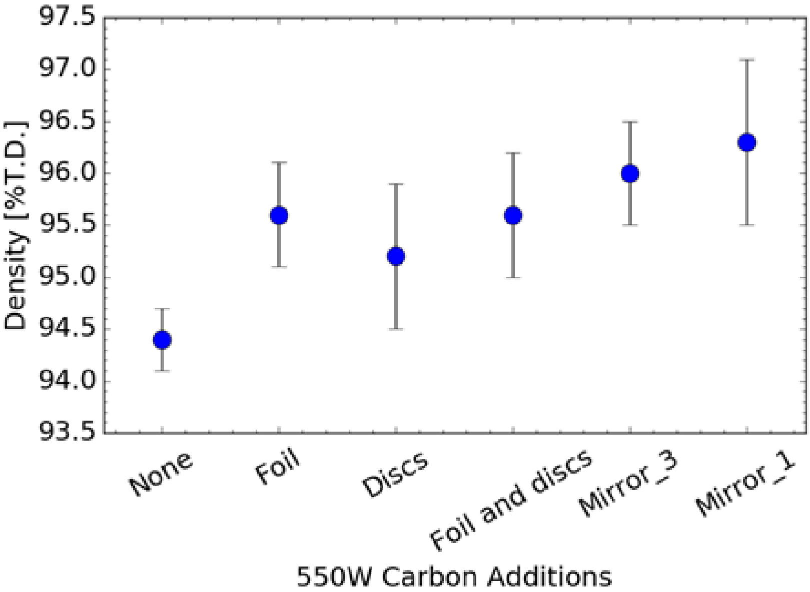

Figure 4.16: Effect of C impurities, following the 550 W heating schedule and C additions (Section 3.3).

The C additions that were added within the furnace while sintering are defined in section 3.2.2, and are different from C that is typically added to SiC powder as a sintering additive, which is dispersed throughout the sample during specimen preparation.

At low power (400W, section 3.3) the inclusion of C foil increased sample density from 90.1% ± 0.3% (without any C) to 93.8% ± 0.3%, the highest in the 400 W test series, as shown in Fig. 4.15. The addition of the C discs as well as the foil, decreased sample density to 88.7% ± 0.4%, the lowest in the series of tests. Fig. 4.16 shows the density of samples sintered with different carbon sources in the furnace and using the 550 W heating schedule. The C inlet foil increased bulk density from 94.4% ± 0.3% to 95.6% ± 0.5%, compared with a sample produced without any furnace additions. For all other tests in this series, the addition of more C or mirrors did not appreciably affect bulk density; the final specimen densities remained within experimental uncertainty.

4.1.5.2.2 Microstructure

	No C	C inlet foil	C inlet foil and discs
$G_{av}(\mu m)$ [Centre]	2.9 ± 0.1	3.8 ± 0.2	2.9 ± 0.1
$G_{av}(\mu m)$ [Edge]	2.0 ± 0.1	3.4 ± 0.1	2.2 ± 0.1

Table 4.8: Effect of C additions on average grain size at low power (400 W Schedule, section 3.2.2).

	No C	C inlet foil	C discs	C foil and discs	Mirror 3	Mirror 1
G_{av}(μm) [Centre]	5.9 ± 0.5	4.5 ± 0.2	4.7 ± 0.2	3.9 ± 0.1	7.7 ± 0.5	5.2 ± 0.3
G_{av}(μm) [Edge]	5.3 ± 0.2	3.6 ± 0.2	4.1 ± 0.2	3.3 ± 0.1	7.4 ± 0.5	4.7 ± 0.2

Table 4.9: Effect of C additions and mirrors on average grain size at 550 W (section 3.2.2). Mirror 3 used C disc supports while mirror 1 used Al_2O_3.

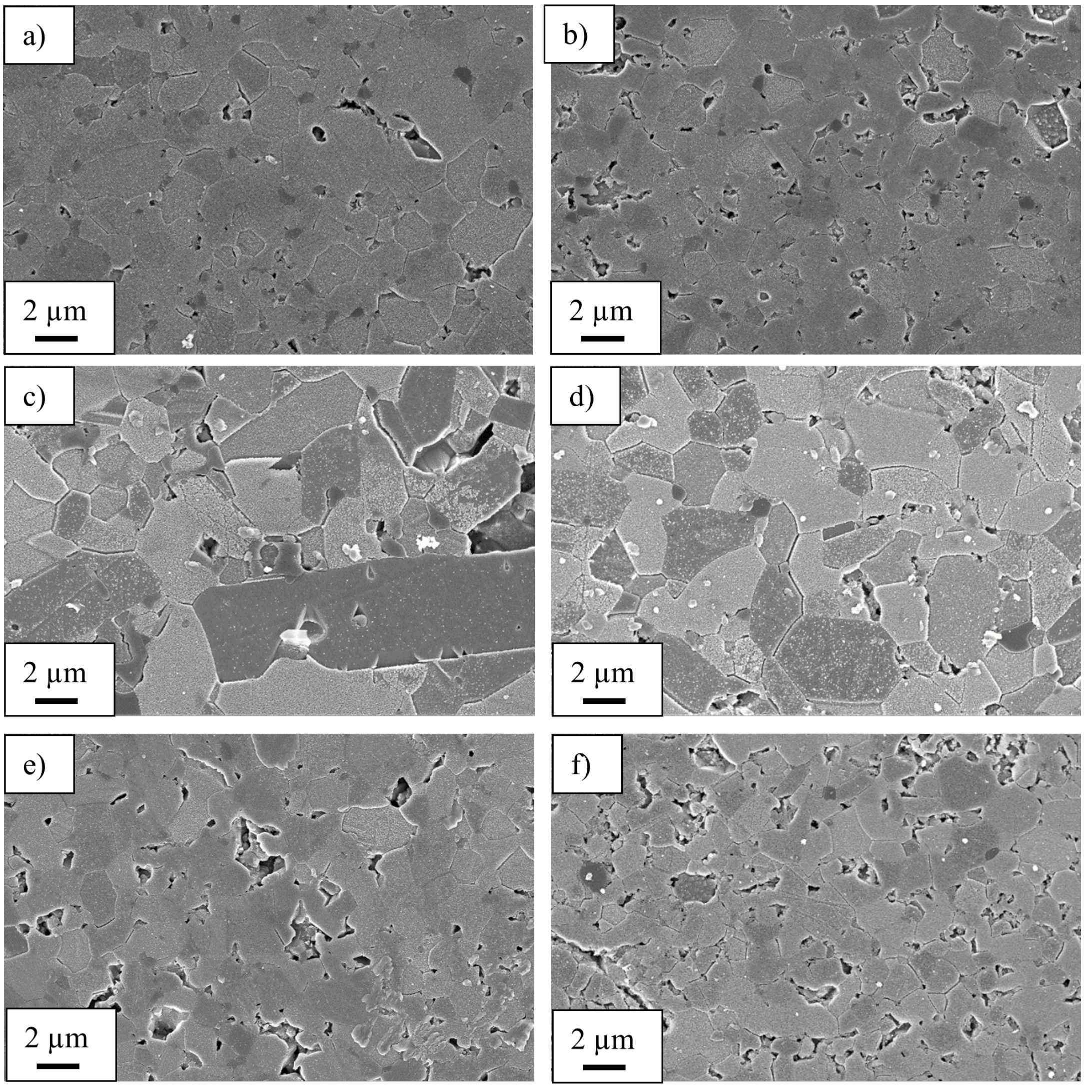

Figure 4.17: SEM images of samples produced at 400 W with C additions (section 3.2.2). Left column images are taken of the centres of the specimens and right column images of the samples' edges. No C addition is shown in a) and b); C inlet foil is shown in c) and d); C inlet foil and C discs shown in e) and f).

As can be seen from Figs. 4.17, 4.18 and 4.19, sample microstructure is highly dependent on the amount of C and mirror configuration in the furnace tube during flash sintering. Average grain sizes of the low (400 W) and high (550 W) power tests are summarised in Tables 4.15 and 4.16, respectively.

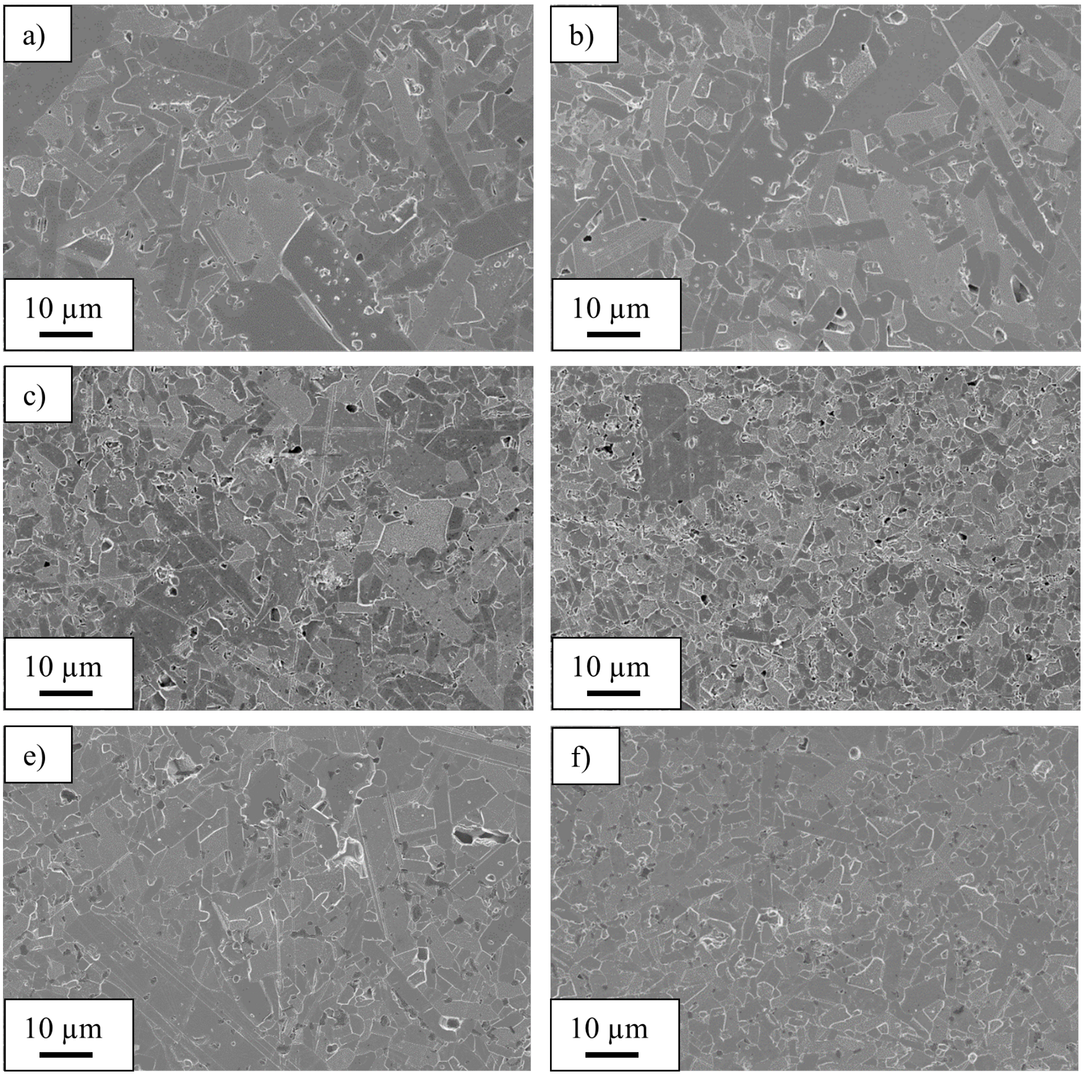

Figure 4.18: SEM images of samples produced at 550 W with C additions (section 3.2.2). Left column images are taken of the centres of the specimens and right column images of the samples' edges. No C addition is shown in a) and b); C inlet foil is shown in c) and d); C discs shown in e) and f).

At low powers, the addition of the C inlet foil increased the average grain size and resulted in more elongated grains in the centre of the sample, compared with the sample produced without C additions. The maximum amount of C in the tube (C foil and discs combination), however, produced a sample with average grain sizes comparable with the sample produced without any C additions (Table 4.8).

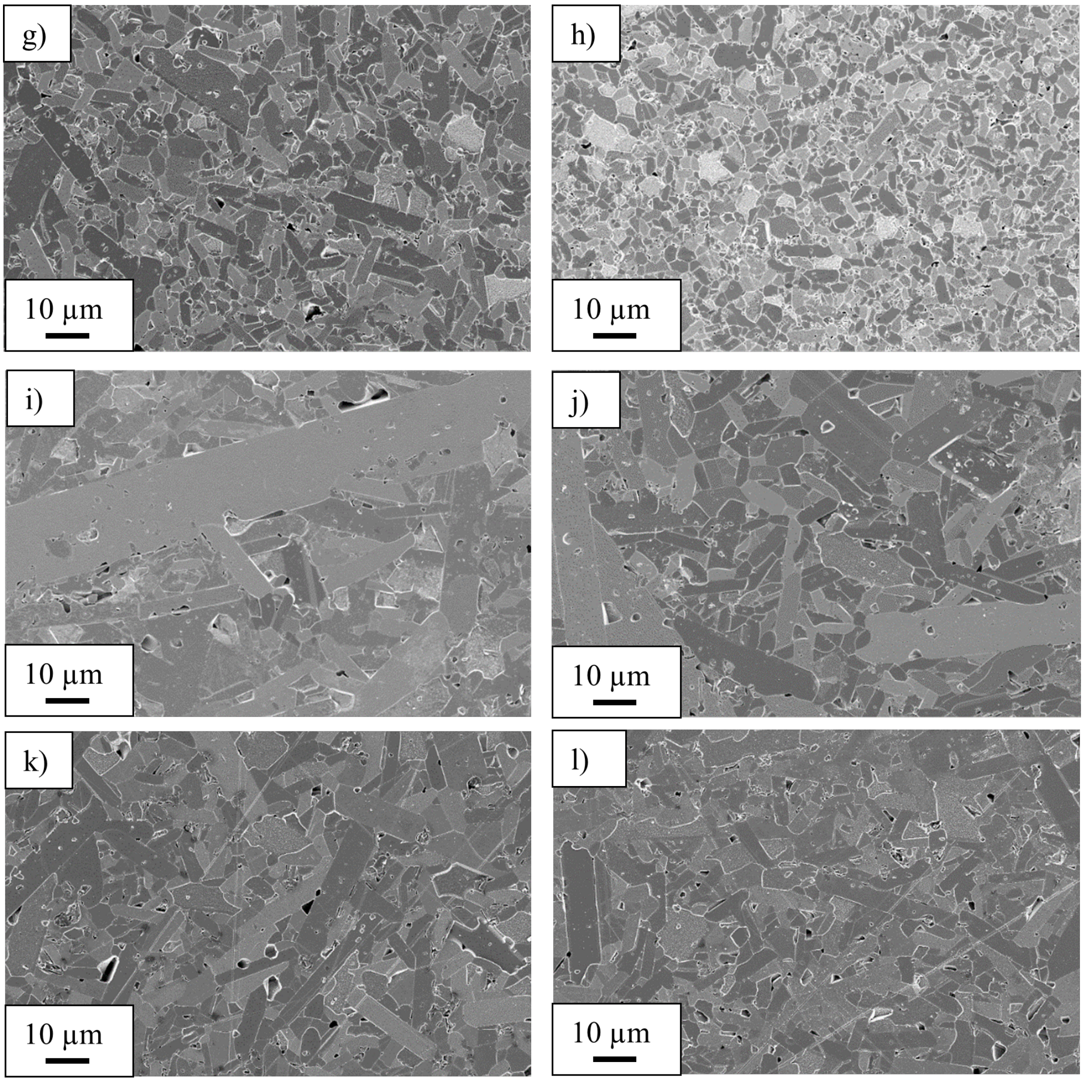

Figure 4.19: SEM images of samples produced at 550 W with C additions (section 3.2.2). Left column images are taken of the centres of the specimens and right column images of the samples' edges. C inlet foil and C discs is shown in g) and h); Mirror 3 shown in i) and j.); Mirror 1 shown in k) and l).

Figures 4.18 and 4.19 shows the effect of C additions and mirrors on sample microstructure for those samples produced using the 550 W heating schedule. The addition of the C inlet foil or the C discs decreased grain sizes compared with those of the sample produced without any additions, the combination of the foil and the discs resulted in the smallest grain sizes of the tests (3.9 µm ± 0.1 µm and 3.3 µm ± 0.1 µm, at the centre and edge of the specimen, respectively). The addition of the mirror 3 set up (C discs, inlet foil and mirrors, section 3.2.2) created elongated grains and the largest of the tests (7.7 µm ± 0.5 µm and 7.4 µm ± 0.5 µm, at the centre and edge of the specimen, respectively) but without a grain size gradient between the centre and edge of the sample. Replacing the C discs with those made of Al_2O_3 (mirror 1) reduced grain sizes at the centre and edge of the sample compared with mirror 2 set up.

4.1.5.2.2 XRD Analysis

The XRD spectra shown in Fig. 4.20 indicate slight differences in peak intensities between samples produced with different C additions in the furnace tube during flash sintering. The corresponding Rietveld analysis in Table 4.10 suggests that C rich sintering atmosphere suppressed the growth of the 4H polytype.

	6H (%)	4H (%)	15R (%)
No C	78.2 ± 0.7	18.5 ± 0.6	3.3 ± 0.4
C inlet foil	86.6 ± 0.5	7.3 ± 0.4	6.3 ± 0.4
C discs and foil	92.2 ± 1.2	2.7 ± 0.4	4.0 ± 0.3
Mirror$_3$	86.7 ± 1.0	7.5 ± 0.5	4.8 ± 0.5

Table 4.10: The effect of C additions on polytypic composition of flash sintered SiC samples (Rietveld analysis of XRD scans in Fig. 4.20).

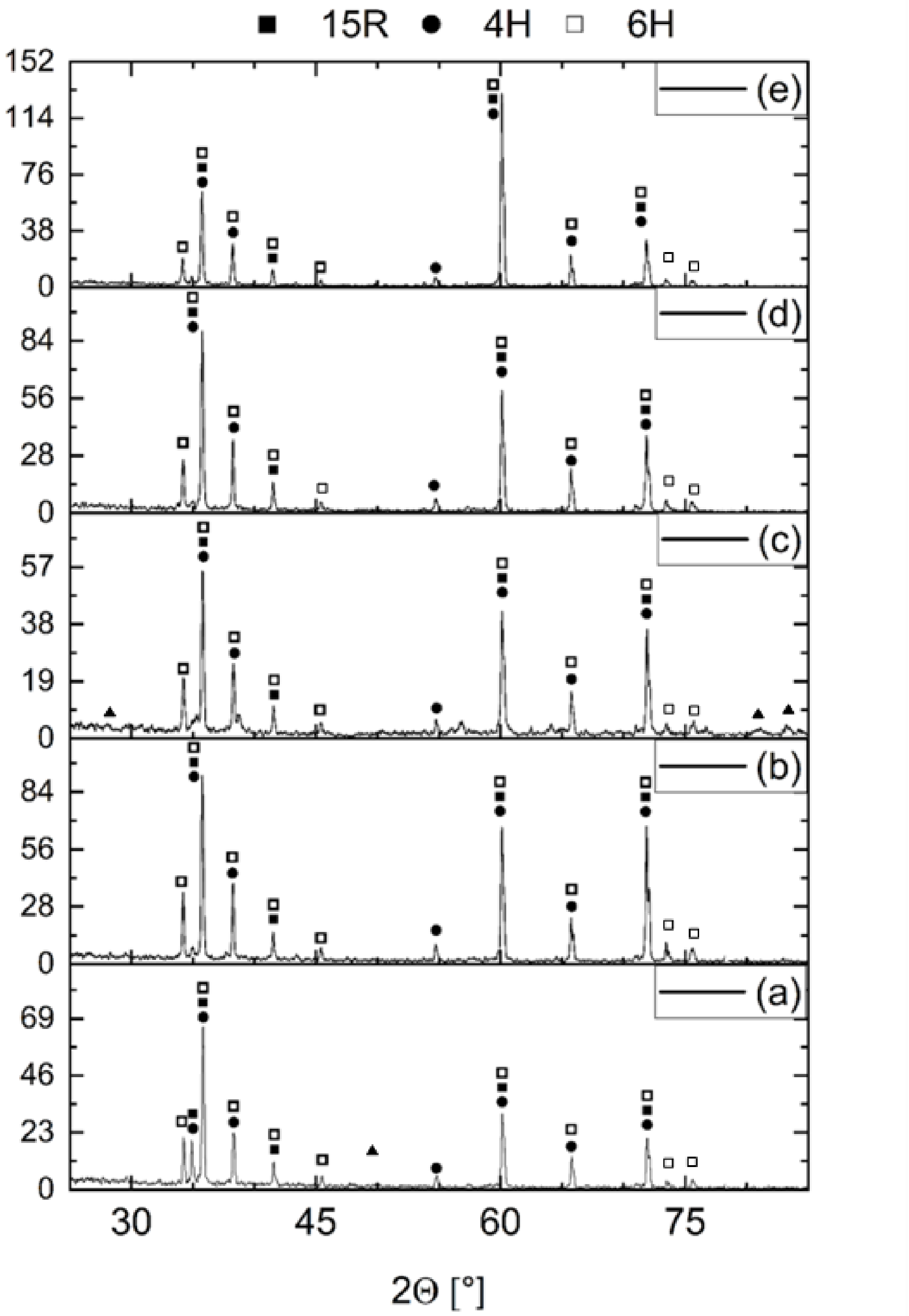

Figure 4.20: XRD spectra of SiC specimens flash sintered at a power limit of 550 W with a) no C additions, b) C inlet foil, c) C discs, d) discs and foil and e) discs, foil and mirrors (mirror 2 set up).

4.1.5.3 Thermal decomposition of SiC

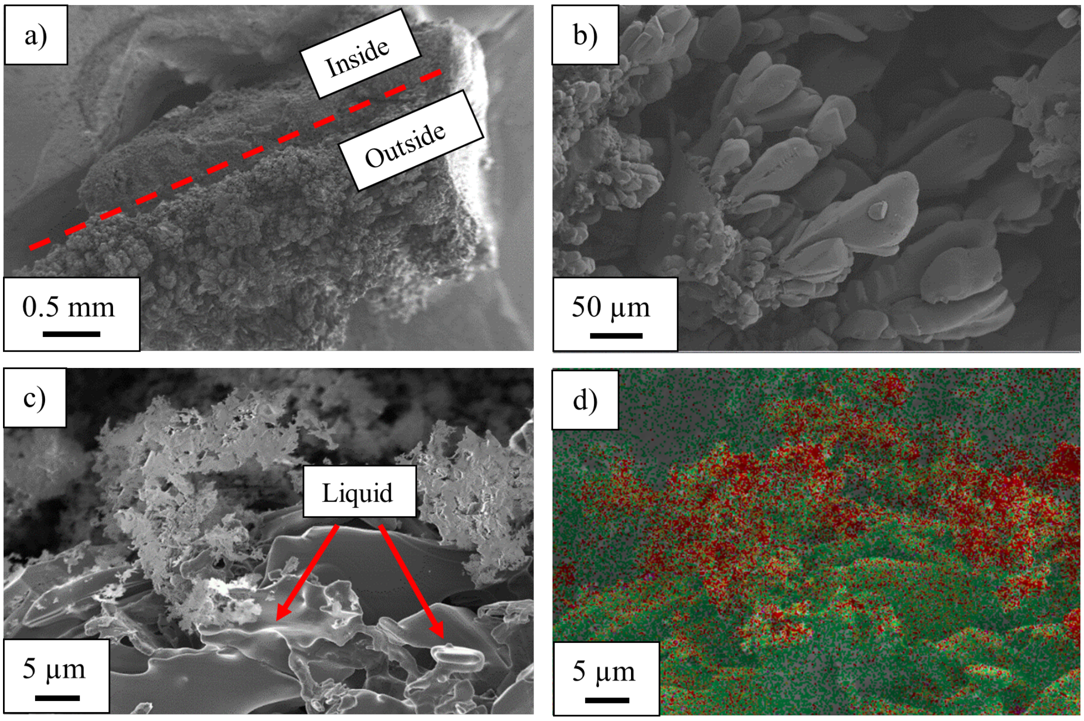

Figure 4.21: a) SEM image of a SiC sample flash sintered for ~1.5 h, b) structure on the surface of the sample, c) the interface region between the phases inside and outside the sample and d) an EDX map of the SEM image in c). C is indicated in red and Si in green.

Figure 4.21 shows SEM images of a sample produced with C discs and inlet foil and held at a power limit of 550 W for about 1.5 h. The outside of the sample in Fig. 4.21a), with respect to the image, is the surface of the specimen, while above it was the central part. Due to the complex topography of the specimen, shadowing may have caused some drop in signal to the detector, but it is clear from the EDX map in Fig. 4.21d) and shape of the structures inside the specimen, that two distinct phases are present. The central, porous part of the specimen was rich in C while the surfaces closer to the outside edge of the specimen were rich in Si, and due to the shape of the structures may have been, at one point, a liquid.

4.1.6 Effect of sintering atmosphere

4.1.6.1 Types of gas

4.1.6.1.1 Densification

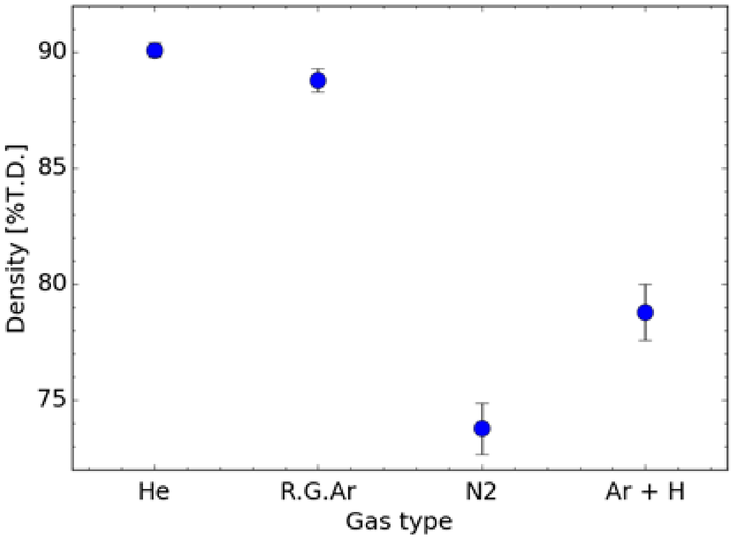

Figure 4.22: Effect of gas type on specimen density. Samples were produced using the 400 W schedule (section 3.3)

Figure 4.22 shows the effect that the sintering atmosphere had on final sample density.

A He atmosphere resulted in the highest bulk sample density at 90.3% ± 0.3%, with RGAr slightly lower (88.8% ± 0.5%). The N_2 test had the lowest density of the tests at 73.8% ± 1.1%.

4.1.6.1.2 Microstructure

	He	RGAr	N_2	Ar + 5% H_2
$G_{av}(\mu m)$ [Centre]	2.9 ± 0.1	2.9 ± 0.1	5.0 ± 0.2	2.4 ± 0.1
$G_{av}(\mu m)$ [Edge]	2.0 ± 0.1	1.9 ± 0.1	4.3 ± 0.1	1.6 ± 0.1

Table 4.11: Average sample grain size dependency on sintering gas type.

Figure 4.23 shows how sample microstructure depended on gas type used when flash sintering; the average grain sizes of the samples are summarised in Table 4.11.

The grain sizes of the samples created in He and RGAr remain within experimental uncertainty of each other. The largest grains were measured from the sample created in N_2 (5.0 µm ± 0.2 µm and 4.3 µm ± 0.1 µm, at the centre and edge, respectively). The N_2 atmosphere also resulted in elongated grains and large pores in the centre of the specimen. The smallest grains of any sample were measured from the specimen created within the reducing atmosphere of Ar +5% H_2 (2.4 µm ± 0.1 µm and 1.6 µm ± 0.1 µm, at the centre and edge of the specimen, respectively).

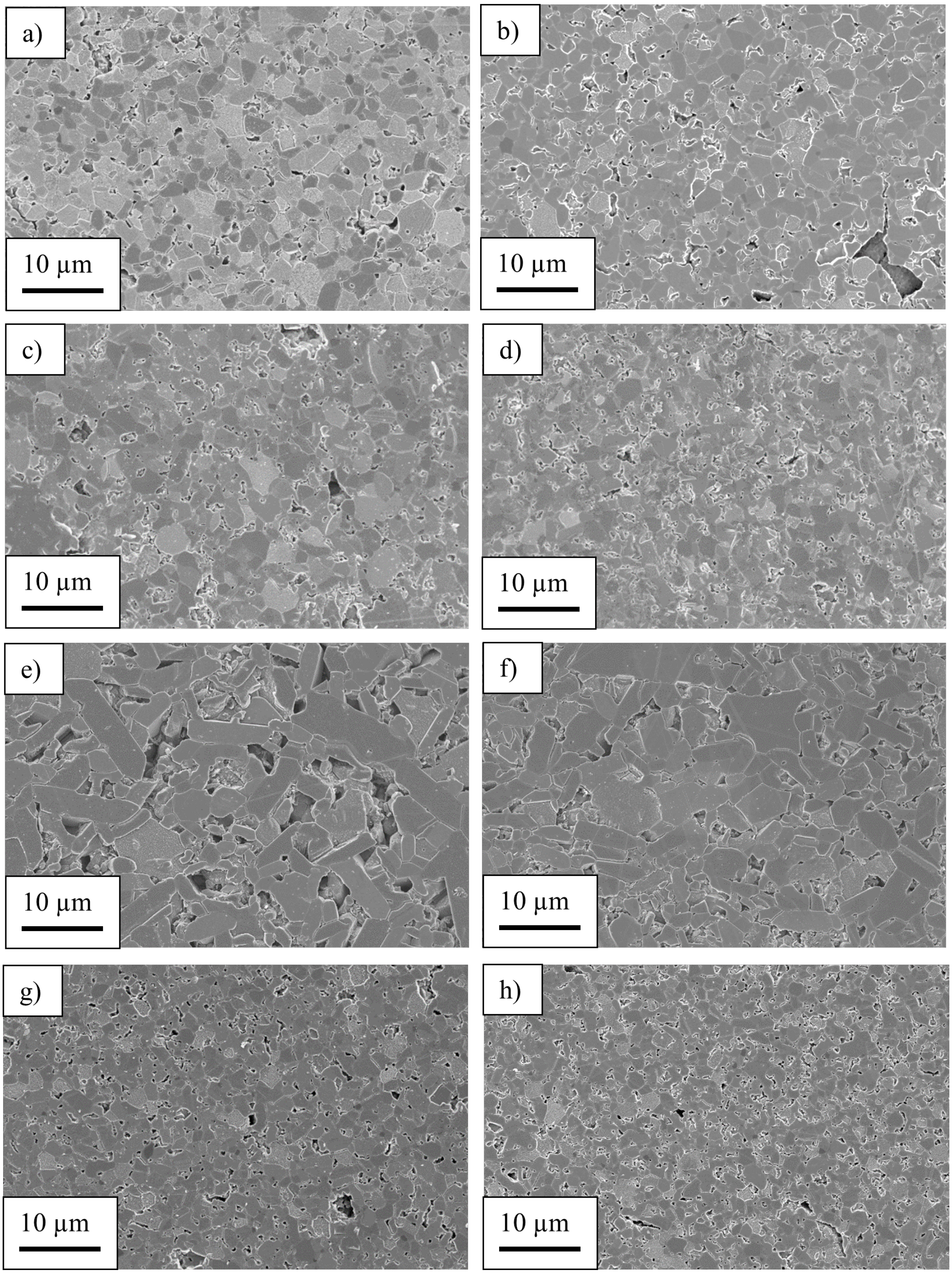

Figure 4.23: SEM images of sample produced at 400 W in different sintering atmospheres (section 3.3). Left column images are taken of the centre of the specimens and right column images of the samples' edge. A He sintering atmosphere is shown in a) and b); RGAr is shown in c) and d); N_2 is shown in e) and f); Ar +5% H_2 is shown in g) and h).

4.1.6.1.3 XRD Analysis

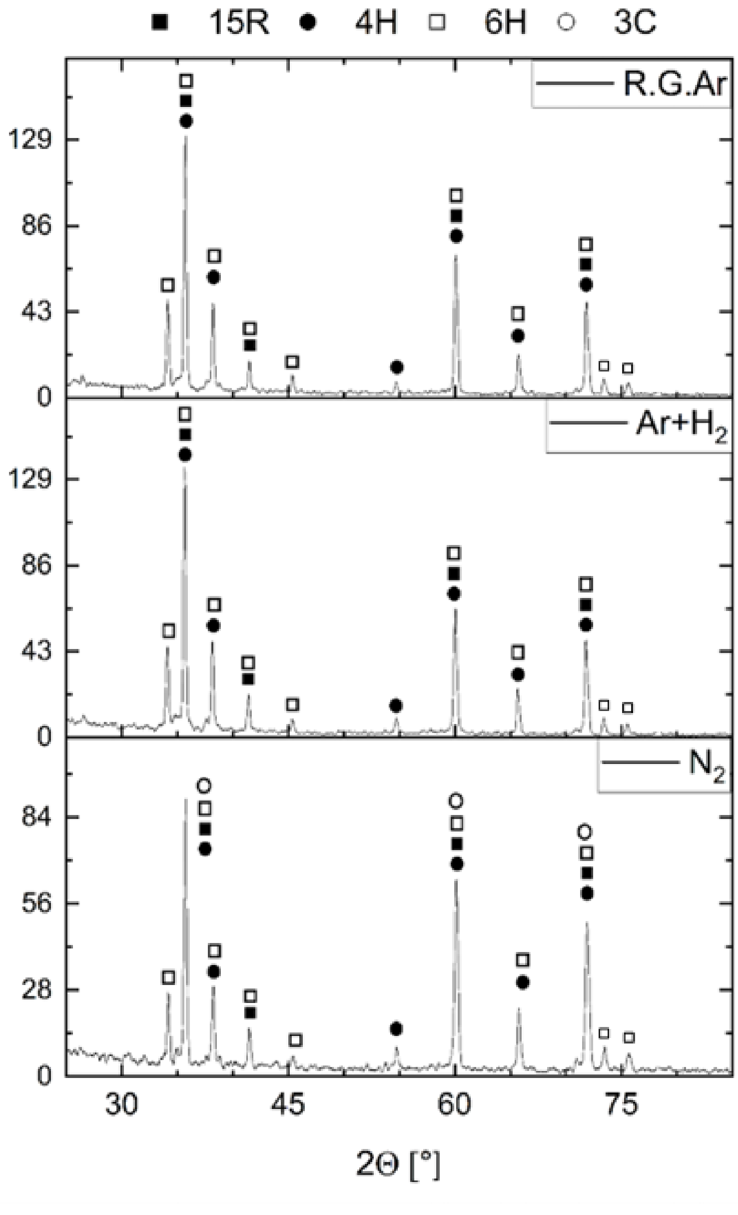

Figure 4.24: XRD scans of samples produced in N_2, Ar +5% H_2 and RGAr.

	6H (%)	4H (%)	3C (%)	15R (%)
N_2	77.3 ± 0.5	4.7 ± 0.4	10.9 ± 0.8	7.1 ± 0.5
Ar +5% H_2	89.7 ± 0.9	3.1 ± 0.2	-	7.2 ± 0.3
RGAr	89.5 ± 0.6	1.6 ± 0.5	-	8.9 ± 0.8

Table 4.12: The effect of sintering atmosphere on polytypic concentration in flash sintered SiC (400 W power limit, section 3.3).

The XRD scans and the corresponding Rietveld analysis of samples flash sintered in different sintering atmospheres are shown in Fig. 4.24 and Table 4.12, respectively. All spectra indicate the bulk of the materials were the 6H polytype. There were slight differences in the relative concentrations of 4H and 15R SiC polytypes in the samples produced with RGAr and Ar +5% H_2 atmospheres. The XRD scan of the sample produced in the N_2 atmosphere suggests that this sample was the only one to contain the 3C polytype (~10% of total polytype concentrations). XRD peaks associated with Si_3N_4 were not identified in the sample produced in a N_2 atmosphere. B_4C was not found in any sample.

4.1.7 Conventional sintering

4.1.7.1 Densification

Table 4.13 shows the effect that conventional sintering schedules had on final sample density. The conventionally sintered fire 1 sample was denser than fire 2 specimen.

	Fire 1	Fire 2
Density (% T.D.)	97.1 ± 0.2	96.1 ± 0.1

Table 4.13: Effect of recommended (fire 1) and fast (fire 2) conventional sintering on sample density. Heating schedules given in section 3.5.

4.1.7.2 Microstructure

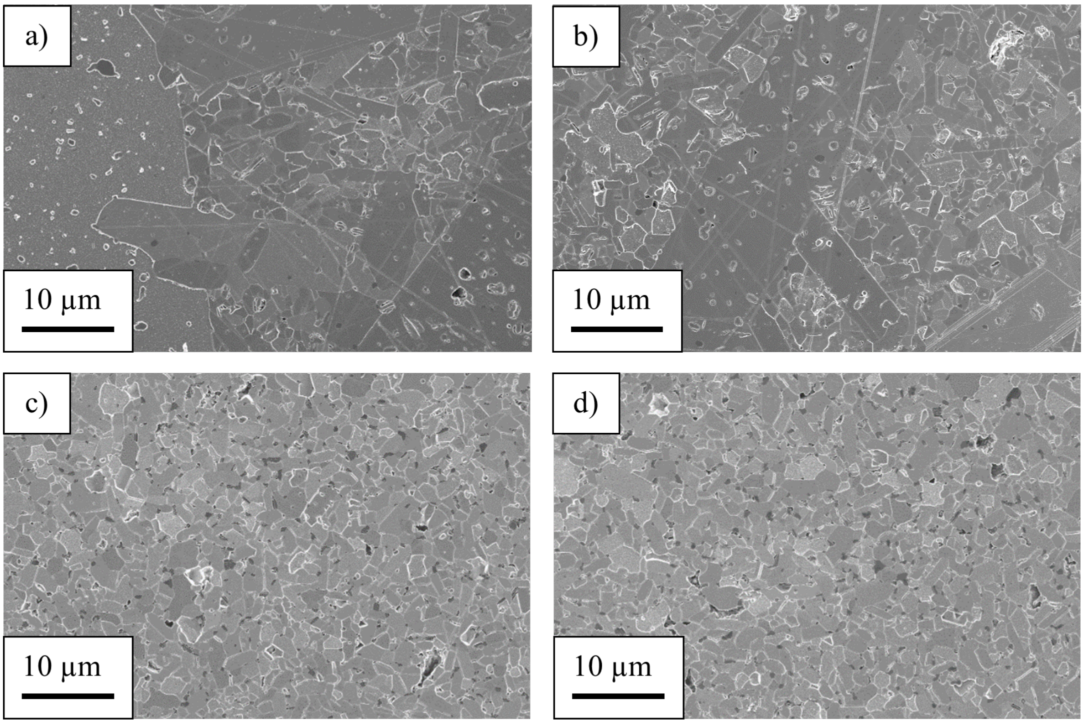

Figure 4.25: SEM images of conventionally sintered SiC specimens (section 3.5). Left column images are taken of the centre of the specimens and right column images of the samples' edge. Fire 1 is shown in a) and b); fire 2 is shown in c) and d).

	Fire 1	Fire 2
G_{av}(μm) [Centre]	10.2 ± 1.1	9.9 ± 1.3
G_{av}(μm) [Edge]	4.4 ± 0.1	4.5 ± 0.1

Table 4.14: Average grain size measurements of conventionally sintered samples.

The effect of fast and slow conventional sintering (section 3.5) on sample microstructure and average grain size are shown in Fig. 4.25 and Table 4.14, respectively. The longer sintering times and slower ramp rate of fire 1 led to large, elongated grains within the specimen, while the fire 2 sample had far smaller, equiaxed grains. Neither sample exhibited a grain size gradient from centre to edge. From Fig. 4.25, the fire 2 sample had more residual, C rich pores than fire 1 (C content shown in Fig. 4.26c). The Rietveld analysis of the XRD scans shown in Fig. 4.26a and 4.26b is given in Table 4.15. The longer hold times of the fire 1 schedule resulted in significantly more of the 4H polytype in this sample (17.7% ± 2.2%) than detected in the fire 2 specimen (5.4% ± 0.7%).

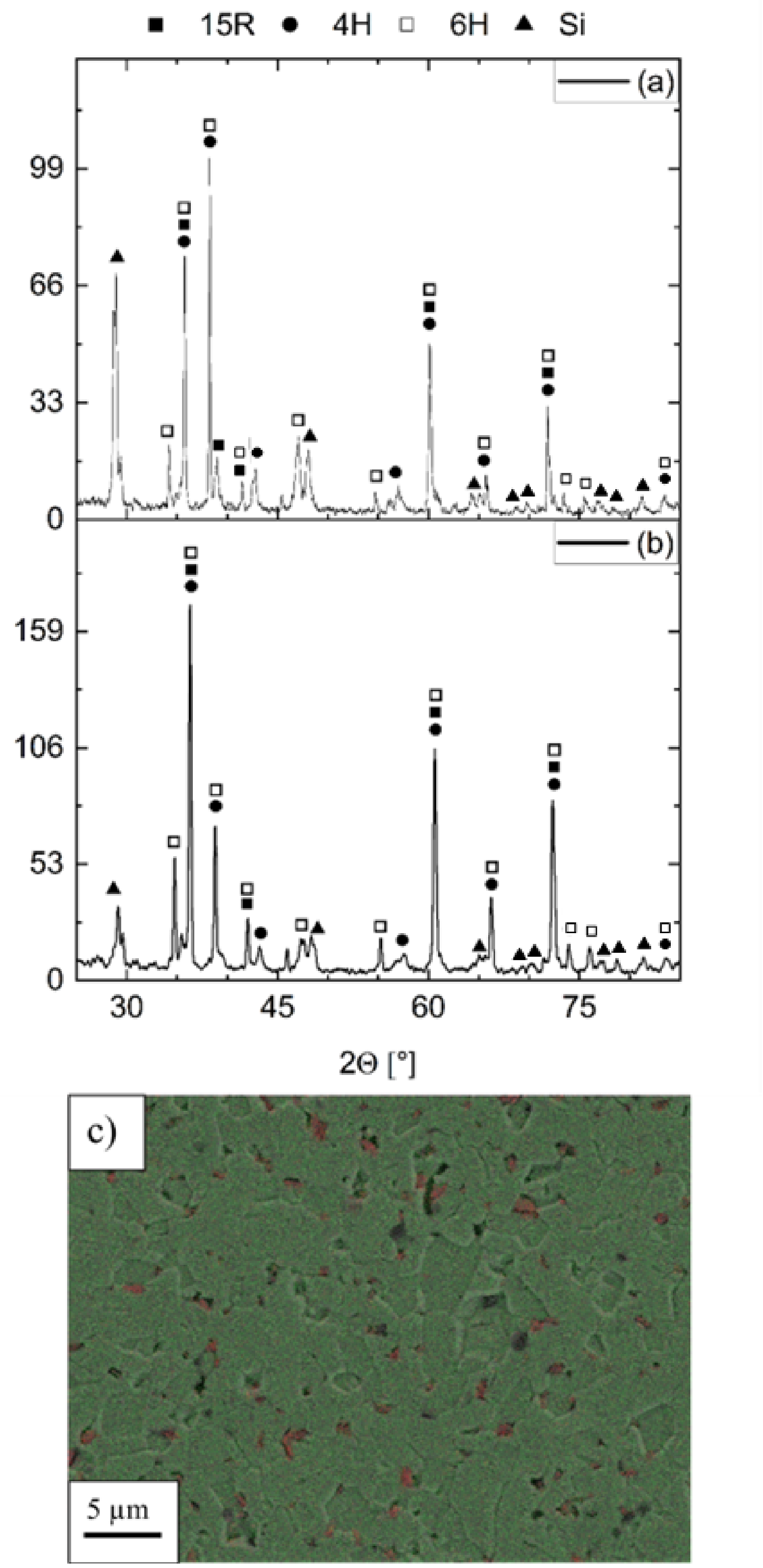

Figure 4.26: XRD spectrum of conventional a) fire 1 and b) fire 2 specimens. c) EDX scan of the fire 2 sample. Red denotes C; Si in green.

	6H (%)	4H (%)	15R (%)
Conventional 1	72.7 ± 1.5	17.7 ± 2.2	9.6 ± 1.3
Conventional 2	87.5 ± 1.0	5.3 ± 0.7	7.2 ± 1.2

Table 4.15: Polytypic composition of conventionally prepared samples.

4.1.8 Effect of sample geometry

4.1.8.1 Bar shaped specimens: sample thickness

4.1.8.1.1 Densification

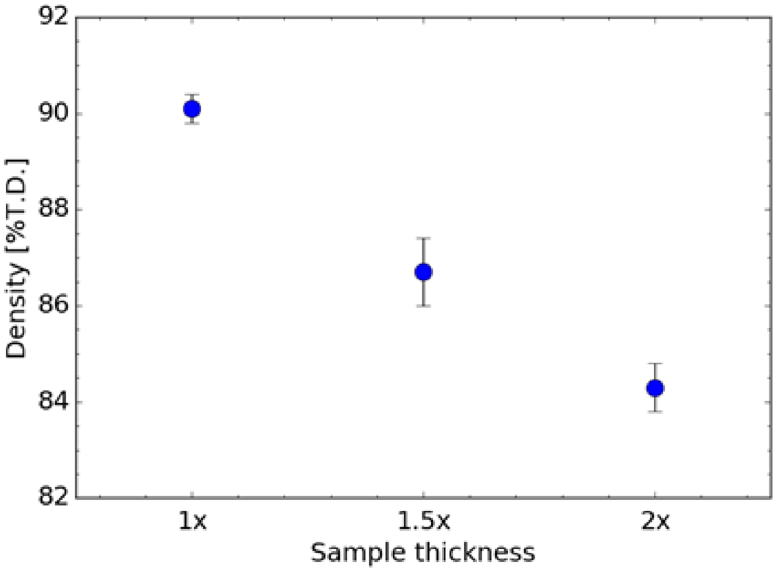

Figure 4.27: Density of samples of different thicknesses. The samples were produced using the 400 W heating schedule and appropriate power levels to maintain similar sample temperatures (section 3.1).

Figure 4.27 shows that increasing specimen thickness decreased final specimen density, despite similar calculated sample temperatures between specimens (2135 °C ± 27 °C). The maximum density achieved was 90.1% ± 0.3% from the sample of standard thickness and the lowest from the specimen with a thickness of two times the standard (84.3% ± 0.5%).

4.1.8.1.2 Microstructure

	1x Sample thickness	1.5x Sample thickness	2x Sample thickness
$G_{av}(\mu m)$ [Centre]	2.9 ± 0.1	2.6 ± 0.1	2.5 ± 0.1
$G_{av}(\mu m)$ [Edge]	2.0 ± 0.1	1.6 ± 0.1	1.3 ± 0.1

Table 4.16: Average grain size measurements of samples with different thicknesses and processed with the appropriate power schedules (section 3.4).

Increasing sample thickness resulted in a decrease in specimen density (Fig. 4.27) and increase in porosity (Fig. 4.28) despite similar nominal surface temperatures between each specimen. The average grain sizes of each sample are summarised in Table 4.16 and show that the grain size at the centre and edge of each specimen also decreased as sample thickness was increased. The largest grains were measured from the sample of standard thickness (2.9 µm ± 0.1 µm and 2.0 µm ± 0.1 µm) and the smallest from the sample that was twice the standard the thickness (2.5 µm ± 0.1 µm and 1.3 µm ± 0.1 µm). The difference between the average grain size at the centre and the edge, of the double thickness and standard thickness samples were nearly within experimental uncertainty of one another at 1.20 µm ± 0.14 µm and 0.90 µm ± 0.14 µm, respectively. Grains remained equiaxed in all specimens.

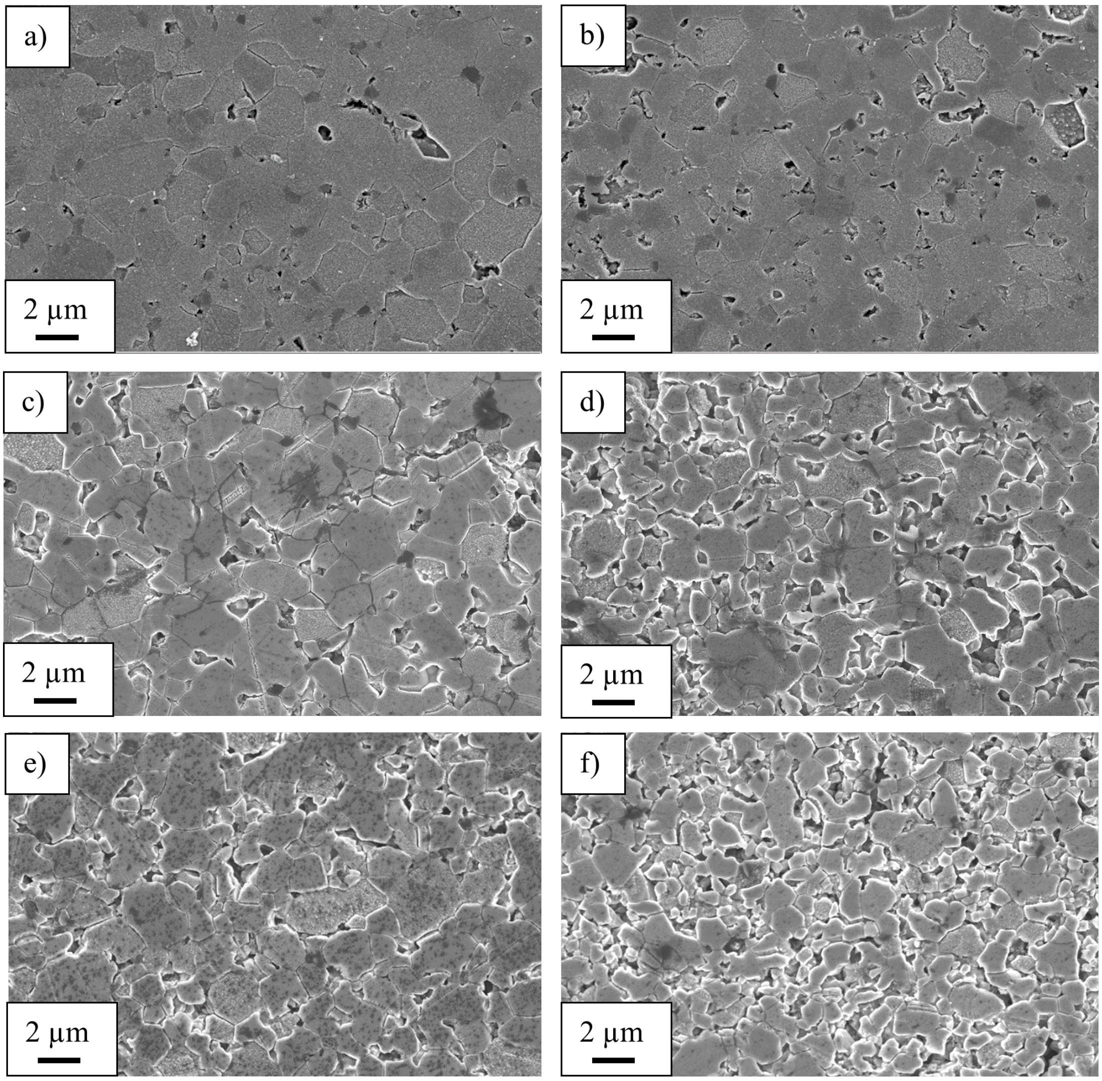

Figure 4.28: SEM images of flash sintered SiC specimens of different thicknesses(section 3.1). Left column images are taken of the centre of the specimens and right column images of the samples' edge. Sample of standard thickness is shown in a) and b); of 1.5x standard thickness is shown in c) and d); of 2x standard thickness is shown in e) and f).

4.1.9 Disc shaped specimens

Using the maximum current of the available power supply, the modified HP technique (section 3.2.4) was used to produce a disc shaped sample that was 65.4% ± 1.0% dense.

To achieve greater densities of disc shaped specimens, a larger power supply should be sought. Figures 4.29 and 4.30 show low and high magnification (respectively) SEM images of the polished sample's centre and at four symmetrically disposed points around the edge of the specimen. Sufficient material was removed during polishing such that the SEM images in Figs. 4.29 and 4.30 show the bulk of the specimen ($\sim$0.5 mm from the surface). Due to the high porosity of the sample, grains could not be identified sufficiently accurately to be measured. As can be seen in Fig. 4.30, in all areas of the sample there are SiC features (light grey) that are greater than 2 µm and signs of neck formation between SiC particles. However, from the low magnification images in Fig. 4.29, densification was not homogeneous.

4.1.9.1 Densification and Microstructure

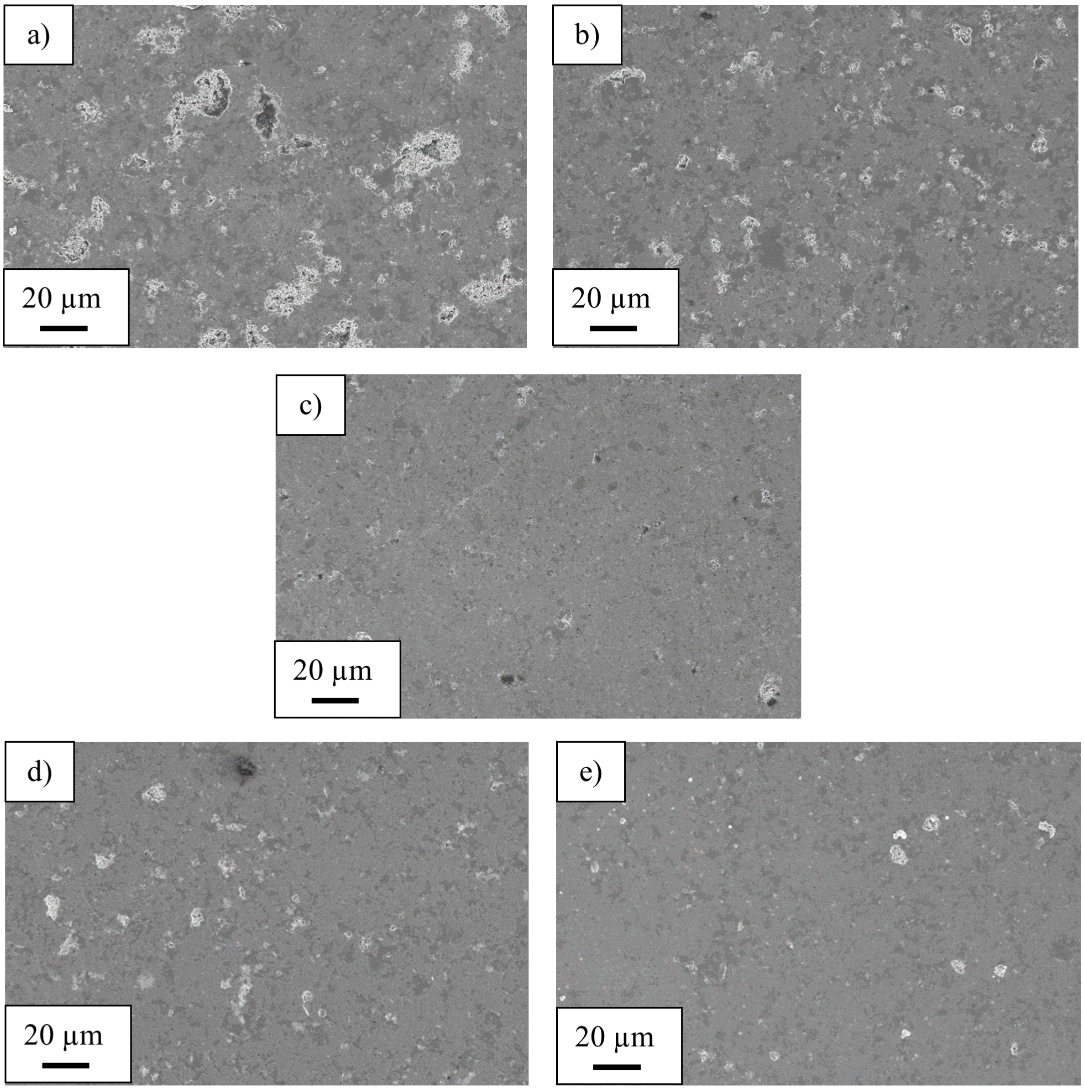

Figure 4.29: Low magnification (500x) SEM images of a SiC disc shaped specimen that was flash sintered in a modified HP (section 3.2.4). The images were taken from an aerial view of the flat area of the disc. The centre of the disc is shown in c) and images from its edge at 4 opposite points are shown in (a,b,c,d).

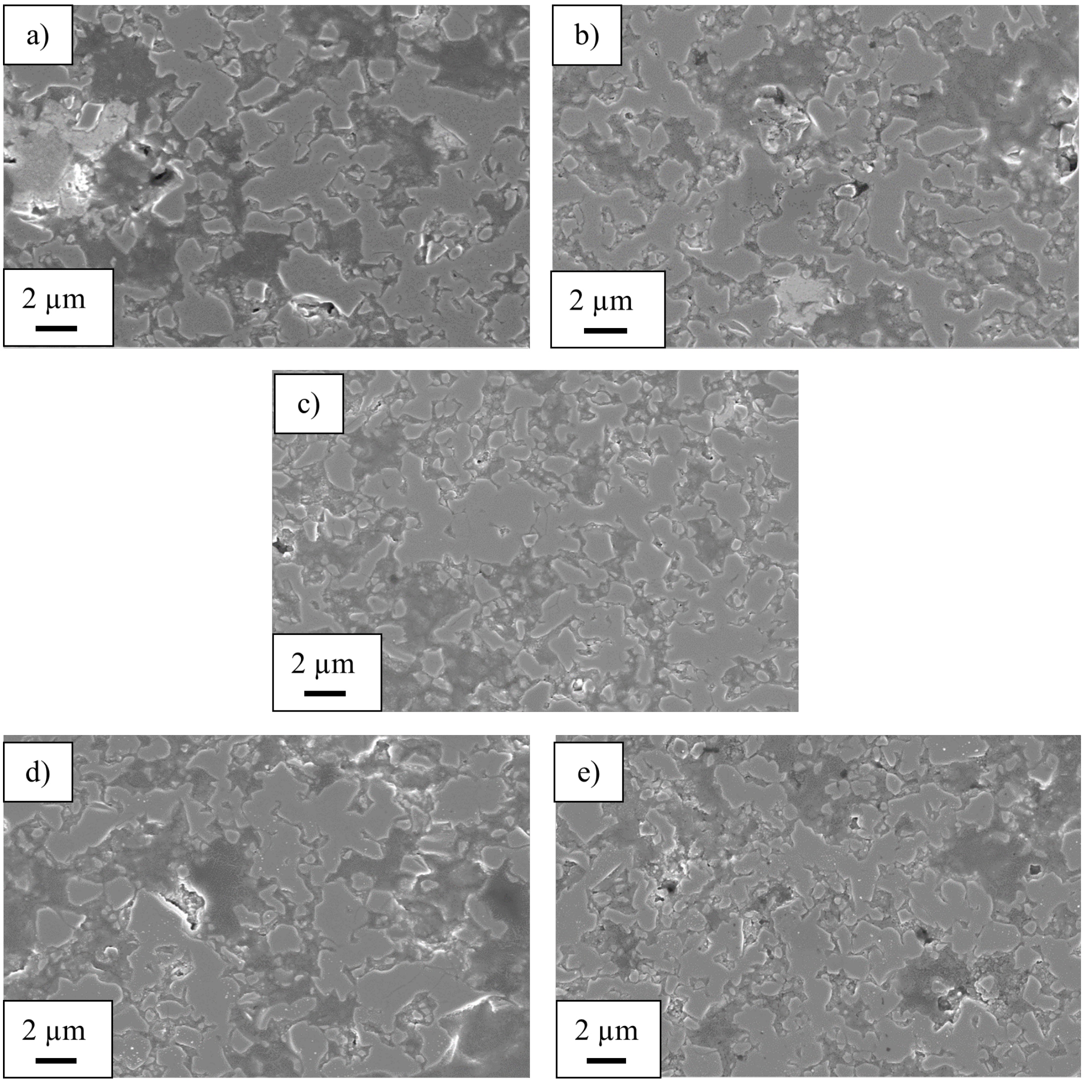

Figure 4.30: Higher magnification view of SEM images in Fig. 4.29.

4.1.10 Shrinkage

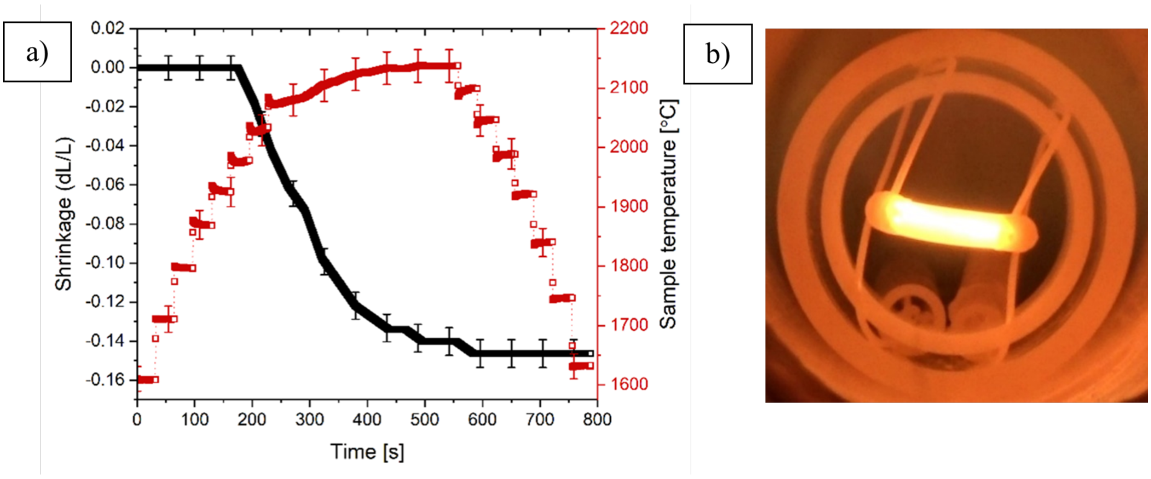

Figure 4.31: a) Specimen shrinkage (black squares) and sample temperature (red squares) against time during a 400 W stepped power experiment (section 3.3). b) visual still of SiC during flash sintering.

From Fig. 4.31a, noticeable shrinkage begins at 180 s, at which point the specimen temperature is ∼1975 °C. Most of the shrinkage occurred before the power was ramped down, roughly 400 s after the onset of shrinkage. Figure 4.1a indicates that a peak sample temperature of 2135 °C was reached and a maximum isotropic shrinkage of 15% was achieved. Figure 4.31b shows an image of the flash sintering SiC sample, at approximately 400 s in Fig. 4.31a. The image shows no obvous signs of asymmetric heating.

4.2 Discussion

4.2.1 Thermal effects of current: similarities with conventional sintering

4.2.1.1 Densification and microstructural comparisons

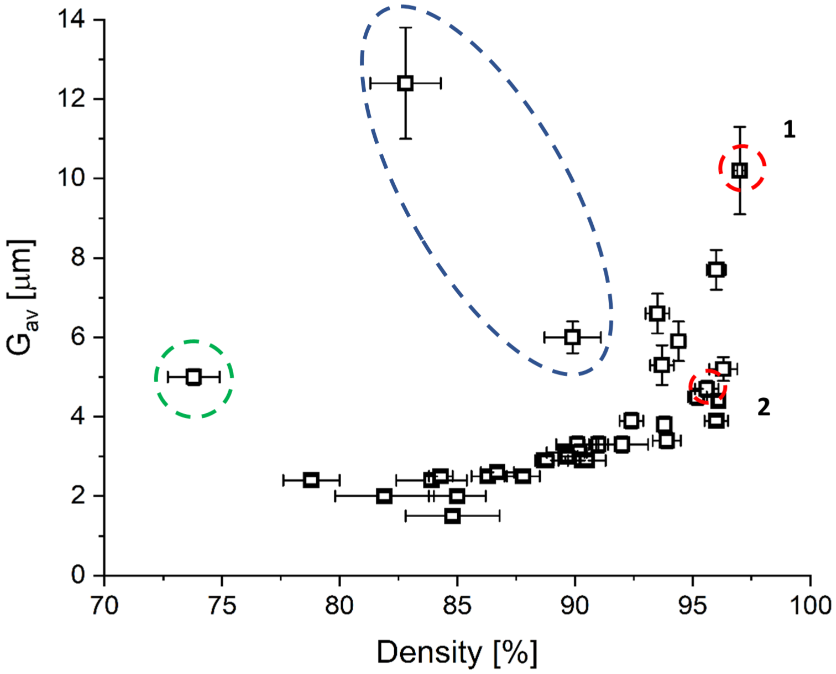

Figure 4.32: Effect of density in average grain size for all flash sintered specimens in this work. Conventional samples are circled in red. Samples with abnormal microstructures due to effects of the sintering atmosphere that was tested are shown in green and blue ellipsis.

Figure 4.32 shows a broad trajectory of average grain size that is typical of a polycrystalline material that was sintered to different densities[151]. It should be noted that the stated density is the bulk density of the sample. Grain size increased with density, weakly at first but once high densities were reached the grain size increased rapidly and without much further increase in density as pore elimination slowed and grain boundary migration continued. The outliers that are highlighted in blue and green ellipses were the result of different sintering atmospheres and are discussed in sections 4.1.5 and 4.1.6, respectively. The conventionally sintered fire 1 and fire 2 samples are shown in the red dashed circles, marked 1 and 2, respectively.

It can also be seen in Fig. 4.32 that there is a slight clustering of data points around 95% density and 5 µm grain size, near the fire 2 ellipse. This cluster contains samples that had C additions in the tube during sintering, and samples that had no such additions and were only affected by heating. Even samples that were "only affected" by heating still had C present as a sintering additive, as it is vitally important to successfully sinter SiC without pressure. As C affects this broad sintering trajectory, it is not surprising that different sintering conditions or slightly changing the C content of the atmosphere could slightly alter the sintering trajectory and create this cluster of samples seen in Fig. 4.32.

Comparisons between the microstructures of flash sintered and conventionally sintered samples show remarkable similarities. Large and small average grain sizes were detected in samples produced using both techniques, grains could be equiaxed or elongated and there was no evidence that could be detected in the SEM images of secondary phases at grain boundaries. However, APT analysis (Fig. 4.33) did show that a phase consisting of Si, B and C was present at grain boundaries in both flash and conventionally sintered SiC.

Additionally, throughout all tests in this work, samples with larger grain sizes typically had greater concentrations of the 4H polytype (tables 4.2, 4.7, 4.10, 4.12). Higher sample temperatures during sintering have been shown by Jepps and Page[29] to increase the amount of the 4H polytype in B doped SiC. All the above suggest that the heat dissipated by the current affected sample density and microstructure in a similar manner to conventional heating methods.

4.2.1.2 Effect of sample temperature and hold time

As for conventional sintering, higher sample temperatures and longer hold times resulted in higher specimen densities (Figs. 4.1 and 4.9, respectively). Bulk densities of approximately 94% could be achieved in 30 min at 400 W, corresponding to a sample temperature of 2135 °C ± 27 °C. However, the same density could be obtained in a total of 16 min by continuing to step up the power to 550 W, corresponding to a maximum specimen temperature of 2205 °C ± 28 °C (Fig. 4.1). Sample temperature could not be increased further without the specimen fracturing. Sample temperatures were within standard error of the recommended sintering temperature of the powder (2150 °C ± 50 °C). The higher density reached by the fire 1 conventionally sintered specimens was due to the longer times spent at sintering temperatures than any of the flash sintered specimens.

4.2.1.3 Liquid phase sintering mechanisms

With sufficient B, a liquid phase can be formed at normal sintering temperatures of SiC (~2150 °C), well below the B_4C-SiC eutectic temperature[45,46]. Stobierski and Gubernat showed that this increases the rate of sintering and, above a certain level of B, can also cause the growth of abnormal, elongated grains such as those seen here in the centre of the specimens (Fig. 4.3k)[41]. The SiC powder used in this work is the same as that used by Stobierski and Gubernat[41,48], and the amounts of C and B are close to the maximum amount reported to give effective sintering without causing abnormal grain growth at 2150 °C. The nominal maximum surface temperature of the specimens created using the 550 W heating schedule (2205 °C ± 28 °C) was slightly higher than this and the observation of elongated, abnormal grains, associated with liquid phase formation in the central part of the specimens in this work can be attributed to the even higher temperature experienced in the interior. Despite this, the average grain size at the centre of the flash sintered specimen was a little over half that of the conventionally sintered, fire 1 sample sintered at 2200 °C. This is likely a consequence of the much shorter hold times used for the flash sintered specimens.

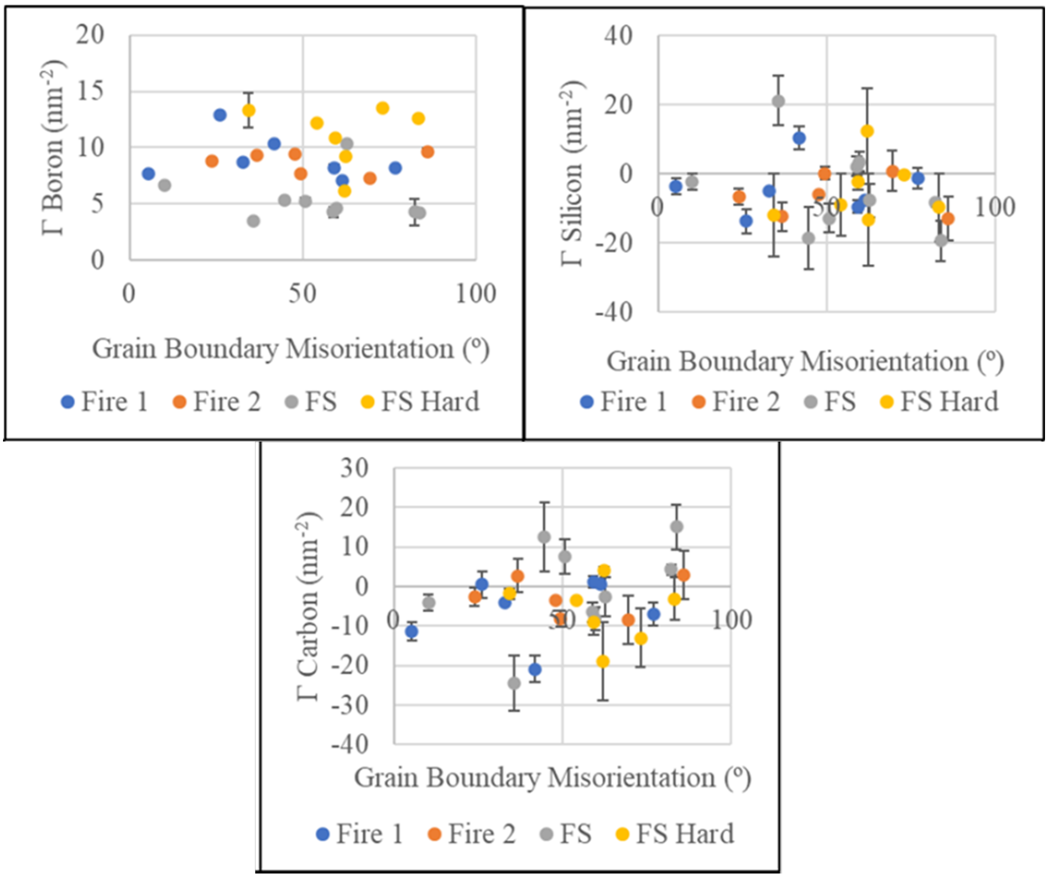

Figure 4.33: Gibbsian interfacial excess values of chemical species in flash sintered and conventionally SiC. Fire 1 and 2 refer to samples that were conventionally sintered.FS refers to SiC that was flash sintered using the 400 W heating schedule without carbon additions. FS Hard refers to samples heated with the 550 W flash sintering schedule, and using the mirror 2 set up (section 3.2).

Gibbsian excess denotes the excess atoms of a particular species found within a feature as compared to the surrounding matrix[146]. Figure 4.33 shows Gibbsian interfacial excess measurements for B, Si, and C for 29 SiC grain boundaries plotted versus grain boundary misorientation. The measurements indicate that flash sintered and conventionally sintered SiC samples had similar grain boundary phases to one another: a slight Si and C deficit and a greater concentration of B than found in the SiC grains.

De Jonghe et al. show that liquid phase sintering aids result in complex phases in

HP ABC-SiC; various phase compositions and both amorphous and crystalline structures were detected at triple grain boundaries, grain boundary films and in inter-grain inclusions[44]. This shows that this degree of grain boundary complexity is encountered in SiC produced through more conventional heating techniques that do not directly heat the sample using electrical current and although they may be complicated, the results of Fig. 4.33 are unlikely a direct consequence of flash sintering.

4.2.1.4 Densification rate

It is difficult to entirely separate the effect of power ramp rate from that of total hold time on sample properties. Faster ramp rates resulted in lower bulk densities, but this is likely a consequence of shorter times at sintering temperatures, rather than any effect of the ramp rate. For example, samples produced with and without a ramp but similar hold times (100 W min^{-1} ramp vs. LH, respectively) had densities and grain sizes that were within experimental uncertainty of one another. Although these results do not entirely separate the effects of power ramp rate from those of total schedule time on sample properties, they suggest that any effect of ramp rate is not as influential on sample microstructure or density as the effect of total schedule time.

The effect of heating rate on SiC microstructure and density was studied by Gephart et al. using an SPS machine[152]. Using the same pressure, final furnace temperature and hold time for each test (45 MPa, 2100 °C and 5 min, respectively), they tested ramp rates from 50 °C min^{-1} to 400 °C min^{-1}. Akin to the results of this work, they show that the fastest heating rates result in the lowest bulk densities and smallest grain sizes, which they attribute to the shorter total times spent at sintering temperatures of the samples that are subjected to the highest heating rates.

The sintering rate of SiC doped with B,C sintering additives was studied by Stobierski and Gubernat who were able to sinter green bodies with similar compositions to the samples in this work to ~92% density in ~40 s at 2150 °C by plunging the specimens into a ready-heated furnace[41]. The flash sintered specimen in this work with the same nominal temperature took 240 s to reach the same density and so, whilst also sintering very rapidly, was slightly slower than in the isothermal experiments of Stobierski and Gubernat. In this work, higher densities were achieved by the conventionally sintered, fire 2 specimen compared with that of a flash sintered sample using the 550 W heating schedule, (96% vs 94%, respectively) despite both samples spending similar times above sintering temperatures. All of the above demonstrates that, as with oxides such as YSZ[99] and ZnO[153], the electric field was not directly responsible for the rapid sintering.

This faster densification rate recorded by Stobierski and Gubernat than those in this work is unlikely to be consequence of heating rate, which, as discussed above, was shown to have little effect on the densification rate of SiC during sintering. It is instead suggested that the slightly slower rates in this work were a consequence of unoptimized sintering additives, caused by the mildly oxidising atmosphere of the Al_2O_3 furnace tube. As can be seen from the ternary phase diagram of B-Si-C at 2230 °C in Fig. 4.34, only a slight change in additive concentration could affect the amount of liquid in the sample. As Stobierski and Gubernat show, densification rates are highly dependent on additive content and hence amount of liquid phase[41]. This might explain the slower densification in this work and is something that could be expected during the conventional, pressureless sintering of SiC.

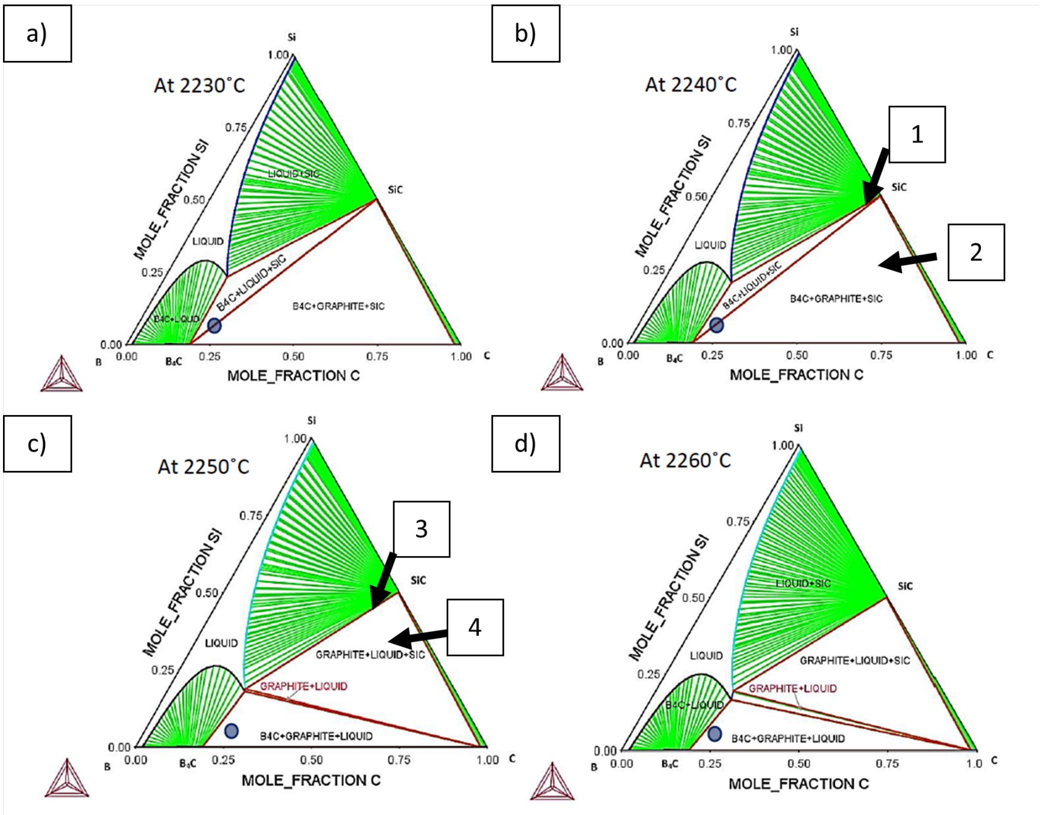

Figure 4.34: Isothermal ternary phase diagrams of the B-Si-C system at a) 2230 °C, b) 2240 °C, c) 2250 °C and d) 2260° C. Diagram produced by Asadikiya et al.[46]. The numbers 1 to 4 represent different phases

.

Todd et al. show that the opposite is true of 3YSZ[99]. They demonstrate that high heating rates can accelerate sintering rates by over two orders of magnitude compared with those achieved with slow, conventional heating rates. 3YSZ can also be flash sintered to near theoretical density in seconds[11]. From Fig. 4.31 it seems unlikely that high density SiC could be reached in the timescale of a few seconds achievable with YSZ. It stands that SiC is fundamentally a different material to YSZ, and it may be that the achievable sintering rate is more limited by grain boundary chemistry than is the case for oxides. This being the case, heating rate, or power ramp rate, may play a less important role in sintering of SiC. However, this is also the case for conventional heating methods and is not a distinct effect caused by flash sintering. High density SiC was achieved using the conventional fire 2 schedule, which was shorter than the manufacturers recommended heating schedule by ∼5 h. Similarly, compared with the fire 1 heating schedule, the production time of the flash sintered sample was reduced by ∼6 h but also with a furnace temperature lower by 700 °C.

4.2.1.5 Thermal decomposition of SiC

Thermal decomposition of SiC has been shown to occur at temperatures about 2500 °C[72] and Stobierski and Gubernat expect thermal decomposition of SiC to occur above 2000 °C[48]. Zapata-Solvas et al. also showed that large areas of the surface of their flash sintered SiC were rich in either Si or C[16]. Given that the temperature of the edge of a specimen produced using a 550 W power limit was 2205 °C and the non-uniformity of temperatures throughout the specimen during flash sintering, it is suggested that thermal decomposition temperatures may have been reached in the hotter portions of the sample, like the hot centre and near the electrodes where contact resistance is high. These sections of the sample have been shown through finite element modelling to be hotter than the edges of the sample during flash sintering of YSZ[116].

Dolloff[72] reported that, at ambient pressures, SiC melts incongruently with Si melting and a C solid remaining in the microstructure. It is suggested that this is what has happened in Fig. 4.21. Due to its higher melting temperature C is left in the centre of the specimen, while some of the Si melts and is pushed to the sample's surface by thermal gradients and some is ejected as vapour. This process continues until it eventually compromises the structural integrity of the specimen and leads to fracturing near the electrode.

4.2.1.6 The role of oxygen during flash sintering

To best of the author's knowledge, there is no evidence in the literature to suggest that O promotes densification during sintering of SiC with B,C sintering additives. The consensus in the literature states that free C is added to the starting SiC powder primarily to remove the O present in the passive layer of SiO_2 on the surface of the SiC powder; typically by adding 3wt.% C[48,82,84,154]. Stobierski and Gubernat show that the optimum amount of C that should be added to the starting powder to achieve the highest density after sintering without pressure is 3wt.%[48]. Their SiC powder was nominally the same as that used during this DPhil project. The starting powder used in this work had an initial carbon content of 3.3wt.%, but this content is very likely to have increased after the 1 h carbonisation stage at 800 C, which was recommended by the manufacturer, to which every sample was subjected. The accepted equation that describes the carbothermal reduction reaction that dominates the removal of SiO_2 from the surface of SiC between 1300 °C - 1400 °C is[154]:

$$SiO2 + 3C = SiC + 2CO \tag{4.1}$$

This demonstrates that the molecular ratio of 3C to SiO_2 is 36/60, and that 5% SiO_2 would require 3% of C to complete the reaction. Given that the samples in this work did, at a minimum, contain 3.3wt% free C, it is highly likely that any SiO_2 was reduced completely over this temperature range. Furthermore, Clegg also found that even without any free C, SiC on its own can react with SiO_2 and remove it at high enough temperatures[154]. Evidence of these carbothermal reduction reactions occurring within samples is implied in Fig. 6.6. Undulations in the samples' resistivity as they are heated through 1300 °C - 1400 °C are suggested to be a consequence of the chemical reactions between the SiC, C, and SiO_2. All samples in this work were slowly heated over this temperature range and as a result, any surface SiO_2 in the sample would likely have been carbothermally reduced before the SiC samples were flash sintered. Furthermore, various carbon sources were also added to the furnace to increase the amount of C in the sintering atmosphere. This would have further aided the reduction of O in the sample at all stages of heating. For the above reasons, it is not anticipated that there was enough of O in the SiC samples in this work for O to have played a dominant role in the densification mechanisms during flash sintering.

4.2.1.7 Errors in temperature estimation

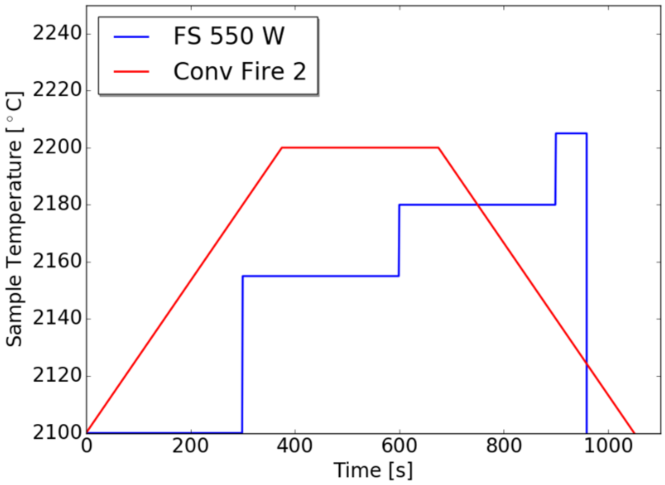

Figure 4.35: Schematics of the conventional fire 2 (red) and 550 W (blue) sample temperature profiles, comparing the time spent by each sample above the lower limit of the recommended sintering temperature of the powder (2150 °C ± 50 °C). The flash sintering schedule was overall shorter than the conventional by approximately 1 h.

Despite the similar times spent at sintering temperatures of the conventionally sintered fire 2 sample and a sample produced with a 550 W heating schedule (Fig. 4.35), the fire 2 specimen had a density of ∼96% whereas the flash sintered specimen only reached ∼94%.

Comparisons between the SEM images taken at edge 1 and edge 2 of the 550 W flash sintered specimen (Figs. 4.3k and 4.3m, respectively) show significant differences in average grain size. Clearly, the two edges were not at the same surface temperature, which is a key assumption of the blackbody radiation model and introduced error into the estimate of the temperature at the sample's surface. The temperature at the surface of edge 2 was likely colder than, and that at edge 1 was likely hotter than, the temperature of the conventionally sintered fire 2 specimen. This was a consequence of sample geometry: edge 2 was initially 3 mm from the centre of the sample while edge 1 was only 1 mm from the centre. Current localisation meant that most of the heat was dissipated in the centre of the specimen. Consequently, surface temperature was highly dependent on distance from the centre of the sample. The colder temperature at edge 2 of the flash sintered specimen resulted in porosity at the sample's edge and hence it had a lower density compared to that of the conventionally sintered fire 2 specimen. The conventional sintering technique resulted in more homogeneous sintering throughout the sample.

Although it is clear from Fig. 4.31 that shrinkage did occur and that the sample did reach sintering temperatures, given the error associated with the assumption of uniform sample temperature, the blackbody radiation model can only provide an indication of sample temperature. This is the case for other flash sintering studies using this method of temperature estimation[100,111,136].

A further source of error when comparing sample temperatures was the measurement of furnace temperature during the conventional sintering of the SiC powder. Above 1200 °C the furnace temperature was measured using a pyrometer. The manufacturer supplied an error of ± 0.01 °C at 2200 °C. It is suggested that this is an underestimate, and likely the instrumental error rather than the total error associated with the furnace temperature measurement. Without further information, it is assumed that the error on the manufacturer's furnace is not any greater than that associated with the error on the temperature of the flash sintered specimen through the blackbody radiation model.

4.2.2 Thermal gradients

Grain size gradients exist between the centre and the edge of almost all samples in this work. This is a consequence of the sample's cooler edge and the current's tendency to localise in the centre of the specimen as a result. This been discussed in previous flash sintering studies, both experimentally[16,101] and through simulation[116,134].

Sample density increased with increasing furnace temperature (Fig. 4.11) despite the moderation of the electrical power to maintain similar sample surface temperatures in this series of tests. A significant difference between tests is the temperature gradient within the sample, which will be greater for a lower furnace temperature owing to the greater heat loss from the surface. This is exacerbated by current localisation in the centre of the sample owing to the NTC of resistivity[108]. A lower furnace temperature also resulted in greater heat losses from the ends of the specimen, beyond the electrodes, which were not included in the calculation of the specimen surface temperature, resulting in a slightly lower sample temperature than intended. A further contribution to this may be that the samples with lower furnace temperature experienced less pre-heating treatment before flash sintering took place. Zapata Solvas et al.[16] showed that pre-treating SiC samples reduced the critical flash sintering temperature (i.e. lowered resistivity). Any reduction of the pre-heat period may also encourage current localisation.

All the above effects cause temperature in the sample interior to be greater than at the edge. This leads in turn to differential sintering, in which the hot interior of the sample sinters faster than the outside. The main consequence of differential sintering is apparent from Fig. 4.11, namely that porosity remained in the cooler, exterior region of the sample when the interior of the sample was already dense. This led to constrained sintering and was the main limitation on the bulk density achieved. It was clearly more pronounced with the higher temperature gradients resulting from a lower furnace temperature. The higher temperature and lower porosity in the interior of the specimen were also responsible for the larger grain size in the centre than at the edge. Despite having a higher density, this is still apparent in samples produced at higher furnace temperatures (Fig. 4.11). This effect can be managed by the use of insulation[133] around the specimen and by more sophisticated electrode geometries[134] that concentrate the current towards the edge of the specimen. Similar conclusions can be drawn regarding the low density results from samples that were thicker than the standard size (Fig. 4.28) or disc shaped specimens (Fig. 4.30).

An error while predicting sample temperatures could also have arisen from assuming the same emissivity value to predict the power needed for each test. Balat-Pichelin and Bousque show that rougher surfaces tend to increase the emissivity of SiC[137]. As the surfaces of the samples produced with lower furnace temperatures, thicker dimensions and that of the disc shaped specimen all had porous edges, the emissivity at the edge of these samples may have been higher than the emissivity value that was originally accounted for. This would result in greater radiative heat losses, and hence an underestimate of the power necessary to heat the edge of the sample to the temperatures that were initially sought (those of the benchmark 400 W test, ∼2135 °C).

The greater extent to which the current localised in all the above samples might have led to the expectation of higher central sample temperatures, as the power would have been dissipated in a smaller volume of the sample. However, this does not appear to be the case in any of the samples that excessively suffered from thermal gradients. A more detailed study of the porosity distribution across the cross section of the samples may provide more clarity as to the extent of current localisation in each instance. It is likely that numerical modelling will be required to understand the thermal gradients inside the SiC during flash sintering, as it has been done for 3YSZ flash sintering studies.

4.2.3 Sintering atmosphere

Outliers in Fig. 4.32 were the consequence of additional chemical reactions caused by the sintering atmosphere. These reactions altered sample properties beyond what could be expected from the thermal effect of the current during flash sintering.

4.2.3.1 Gas type

While Helium and RGAr gas types provided similar, inert sintering atmospheres, N_2 and Ar + 5% H_2 gas types had a significant effect on sample density and grain size (are highlighted in Fig. 4.32 by green ellipses). The N_2 atmosphere resulted in larger, more elongated grains than those in samples produced in inert atmospheres (~5 µm in the centre vs ~3 µm, respectively) and the lowest bulk density of the atmosphere tests (~78%). The effect of N_2 doping on α-SiC with B,C sintering aids has been studied previously by Kondo et al.[30]. They show that the incorporation of N_2 in the SiC lattice stabilizes the 3C (beta) phase of SiC, and Jepps et al. demonstrated that a N_2 atmosphere promotes the reverse phase transformation of alpha to beta SiC[29]. This is corroborated with the results in this work, where the Rietveld analysis shows that the sample flash sintered in a N_2 atmosphere was the only sample to exhibit the cubic, 3C phase of all the tests. It is concluded that the flash sintering technique did not alter how N_2 affects SiC sample microstructure during sintering.

The reducing atmosphere created by using Ar + 5% H_2 gas during flash sintering restricted grain growth and lowered sample density when compared to samples produced in helium or argon. The effect of O_2 partial pressures on active and passive oxidation of SiC has been studied by Raj et al.[155]. They show that reducing the partial pressure of O_2 at sintering temperatures of SiC (>2000 °C), can lead to active oxidation of SiC. Very low O_2 partial pressures (10^{-7} atm) can lead to volatilisation of SiO_2 or thermal decomposition of SiC.

It is proposed that the reducing atmosphere created by the Ar + 5% H_2 gas lowered the partial pressure of O_2 in the furnace tube to an extent where the SiC sample actively oxidised during flash sintering. This resulted in a lower bulk density, compared to the samples created using RGAr or He atmospheres. Grain growth was also restricted compared with the RGAr or He tests.

4.2.3.2 Role of carbon in the atmosphere

Unfortunately, there is no quantitative measurement of how much C is in any of the samples in section 4.1.5. As a result, the discussion below is to be treated as a broad, speculative argument to explain the clear, empirical effect that the C additions had on the density and microstructure of SiC in this work.

The addition of C sources (inlet foil and discs) in the furnace tube affected sample densification and microstructure in all tests (Figs. 4.1.5). Urretavizcaya et al. showed that graphite discs placed either side of Al_2O_3/SiC_w samples greatly affected sample microstructure during sintering[156]. They propose that graphite discs reduced O_2 partial pressures through CO in the atmosphere which led to the precipitation of graphite on the surface of the samples. It is suggested that the C additions in this work behaved in a similar manner. Additionally, it is more plausible that the C indirectly affected the centre of the samples: additional C on the surface reduced the amount lost in the centre of the sample during heating. However, given the clear effect a N_2 sintering atmosphere had on the microstructure at the centre of a SiC sample during a similar heating schedule, it may be that the effect of atmosphere is more pronounced at low temperatures, before densification takes place. It is also worth noting that while C may have affected sample microstructure in a similar manner to an Ar + 5% H_2 atmosphere, the latter's effect was clearly more pronounced. This could be expected as the small amounts of CO relative to an atmosphere purely of Ar + 5% H_2 would be less reducing.

Broadly, C had two distinct temperature regions in which it affected sample microstructure: below 2240 °C where it restricts grain size, and above where it causes large grain growth.

For most of the results in this work, additional C was not used. In this case, it is suggested that sintering took place in 'phase 1', as is marked on the B-Si-C ternary phase diagram in Fig. 4.34. That is, below 2240 °C and with a small amount of B so as to create a liquid phase, as suggested by Stobierski and Gubernat[41]. In this regime, the C additions in the powder restricted the average pore radius as the sample is heated[48] and reduced the SiO_2 on the surface of SiC[21] which increases powder surface energy and promotes densification.

The addition of C into the atmosphere at this temperature moved the sintering into phase 2 (Fig. 4.34) where there was less liquid phase and more solid phase (B_4C + graphite + SiC). Without a liquid phase, grain growth was restricted compared to the case with lower amounts of CO in the atmosphere or graphite on the surface of the sample (which may have indirectly retained more C in the sample's centre). This can be seen in almost all samples produced with C additions, with more C resulting in smaller average grain sizes (Figs. 4.17 and 4.18). The two exceptions to this are described in the following paragraphs.

First, the addition of C foil to the 400 W heating schedule increased the average grain size compared to a sample produced without C. Stobierski and Gubernat showed that there was an optimum amount of C sintering aid (3 wt.%) needed to achieve the highest bulk density of SiC during sintering[48]. The same is assumed for this SiC powder but as suggested above, due to the mildly oxidising atmosphere of the alumina tube, a greater amount of C might have been necessary to achieve the optimum amount in this work compared to the optimum found by Stobierski and Gubernat, who sintered their SiC in a graphite furnace. It is suggested that the amount of C introduced into the system by the C inlet foil is, within the conditions tested, closer to the optimum amount of C that is required to achieve maximum sample density in this work. Any additional C into the system then reduced grain sizes, as can be seen in Fig. 4.18 and reported by Stobierski and Gubernat.

The second exception was if the sample was heated above 2250 °C. Above this temperature, a liquid phase is present in most of the phases in the B-Si-C ternary phase diagram (Fig. 4.34c). Sample temperatures achieved using the mirror set up shall be considered around this region. No flash sintered sample that displayed abnormal grain growth was investigated using APT.

The mirrors are assumed to have increased sample temperatures as they are made from molybdenum or SiC and both are used as infrared mirrors in space[157] and laser[158] applications (set up shown in section 3.1). Comparing samples produced with the same C foil addition and heating schedule, but sintered with and without mirrors, the mirrors increased the average grain size in the centre and edge of the specimen (550W, C foil vs mirror 1). This suggests that the mirrors did increase sample temperatures and a thermal contribution from the mirrors to grain growth shall be assumed for all mirror tests.

The mirror 3 sample (C foil and discs) was one of the densest and hence hottest of the samples in the mirror tests (above 2250 °C). This resulted in a liquid phase (Fig. 4.34c) at the centre and edge of the sample and hence abnormal grain growth that was not present when the C additions were used without the mirrors.

With respect to the sample produced with the mirror 2 set up (C discs), this specimen may not have been quite as dense as the others (Fig. 4.12) and as a result may have had a slightly lower temperature than those for the same power limit. Given the temperature sensitivity in the phase diagrams, that only 10 °C can result in a large change of phase (Fig 4.34b and 4.34c), even small dimensional changes in the sample could affect specimen temperatures and hence the phase of the sintering additives. It is suggested that the edge of this specimen was in phase 2 (Fig 4.34b), while the hotter centre was in phase 3, shown in Fig. 4.34c. This reduced grain sizes at the edge of the specimen while it resulted in larger, elongated grains in the centre, relative to the 550 W schedule with no C additions.

The sample produced using the mirror 1 set up (C foil) did not suffer from abnormal grain growth but had a similar density to the sample produced with the mirror 3 set up (C foil and discs). A tentative hypothesis could be that the alumina discs on which the mirror set up was placed, resulted in a slightly cooler sintering atmosphere than that created by the mirror 3 set up. This could be caused by the alumina discs absorbing less heat than the C discs due to alumina's smaller emissivity value compared with that of C ($\sim$0.75[159] vs $\sim$0.79[160], respectively). Additionally, the highly anisotropic behaviour of graphite's thermal conductivity may have reduced the amount of heat removed from the molybdenum mirrors and caused the atmosphere around the sample sintered with alumina discs to be cooler. If the sample was cooler, there would be less liquid phase (Fig. 4.34b) and hence would have smaller grain sizes than the sample sintered with C discs.

Carbon as insulation

The outliers in the green ellipse in Fig. 4.32 were the result of samples produced using C felt and foil as insulation. These samples had large average grain sizes and low densities.

If the C foil was wrapped too tightly around the sample, the sample would crumble when removed from the furnace after flash sintering. If wrapped into a cylinder loosely around the sample, the specimen would survive. As discussed in section 4.2.3.2 sample microstructure and density are highly dependent on the proximity of C to the sample surface. It is suggested that the C insulations were mounted too close to the sample, which resulted in lower partial pressures of O_2 than was the case when the C was introduced via the inlet foil or discs below the sample. This proximity of the C source to the sample actively oxidised the surface of the samples and reduced the bulk densities reached.

The very large grains shown in Fig. 4.14 created by the C felt suggests that this insulation overheated the SiC sample during sintering. Akin to the results of the mirror 3 test, these very high sample temperatures (>2250 °C) resulted in a liquid phase which caused abnormal grain growth. The large peaks in the XRD spectra (Fig. 4.13) might not necessarily be indicative of polytypic concentration in these samples and may instead be explained by the increased probability of the detecting these very large grains.

Chemical stability at high temperatures

Additionally, C also allowed longer sintering times to be achieved. The maximum repeatable time that a sample could spend sintering at a power limit of 550 W without any C additions was 1 min without fracturing. With the C inlet foil and discs, the sample remained intact for approximately 1.5 h at this same power limit (Fig. 4.21). Without C, the passive layer of SiO_2 on the surface of SiC reacts with the SiC through the following reaction[48]:

$$SiO_2 + nSiC = Si \uparrow + SiO \uparrow + CO \uparrow + (n-1)SiC \tag{4.2}$$

In presence of excess C, the C bonds with the volatile products (Si and SiO) in Eqn. 4.2 and only CO is transferred to the gaseous phase though Eqn. 4.3:

$$SiO_2 + nSiC + 3C = CO \uparrow + (n-1)SiC \tag{4.3}$$

This reduction in the amount of Si limited ejection of Si vapour that would have otherwise resulted in sample fracture. However, after a 1.5 h hold period, the sample was totally thermally decomposed (Fig. 4.21), with microstructures similar to a sample that was heated beyond 2205 °C without any C (Fig. 4.5). The specimen crumbled when it was removed from the furnace.

It is suggested that all specimens produced in this work at a power limit of 550 W were thermally decomposing, and that C merely delays the inevitable. Although the C additions and the limited sintering times of flash sintering reduced its effect on final sample microstructure, it should be considered in future work.

Chapter 5

Mechanical properties of flash sintered silicon carbide

This section details the mechanical properties of the SiC samples described in Chapter 4. While Vickers hardness values are given of all the samples discussed previously, strength and toughness values are only given of samples that were conventionally sintered with long and short holding times, and those produced using an optimised flash sintering process: 550 W power limit, C discs and foil. This flash sintering heating schedule was chosen as an optimum as it produced samples with small, equiaxed grains, high densities and Vickers hardness values that were higher than conventionally expected of similar SiC. A comparison between the mechanical properties of optimised flash sintered and conventionally sintered SiC is presented and discussed.

5.1 Effect of flash sintering parameters on Vickers hardness

5.1.1 Results

5.1.1.1 Indentations

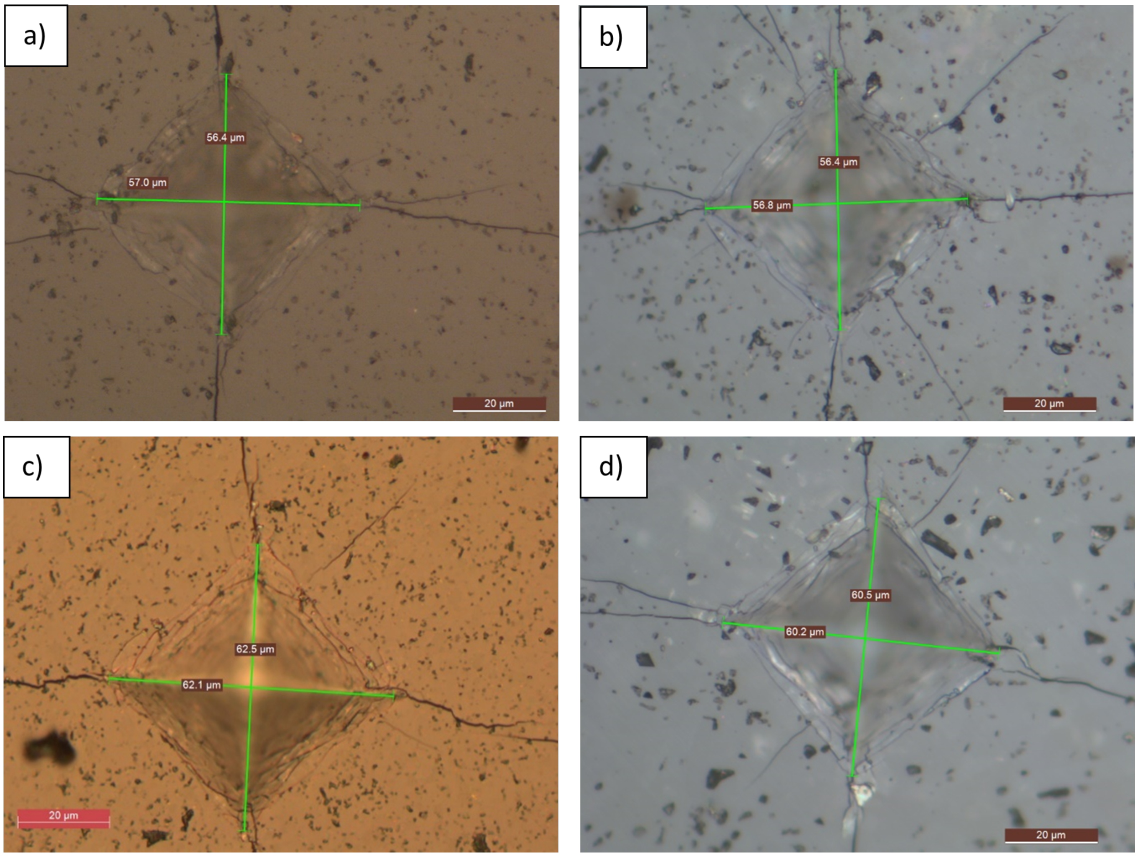

Figure 5.1: Representative micrographs of Vickers indents in a) and b) super hard SiC (∼28 GPa) and c) and d) SiC samples of normal hardness (∼24 GPa). All indentations were made using using a 5 kgf load.

Representative optical images of Vickers hardness indents in flash sintered specimens are shown in Fig 5.1. The indents in Fig. 5.1a and b is representative of samples that exhibited super-hardness, ∼28 GPa, while those in Fig. 5.1c and d are typical of samples that hardness values thata could be expected of SiC, ∼24 GPa.

5.1.1.2 Effect of density on hardness

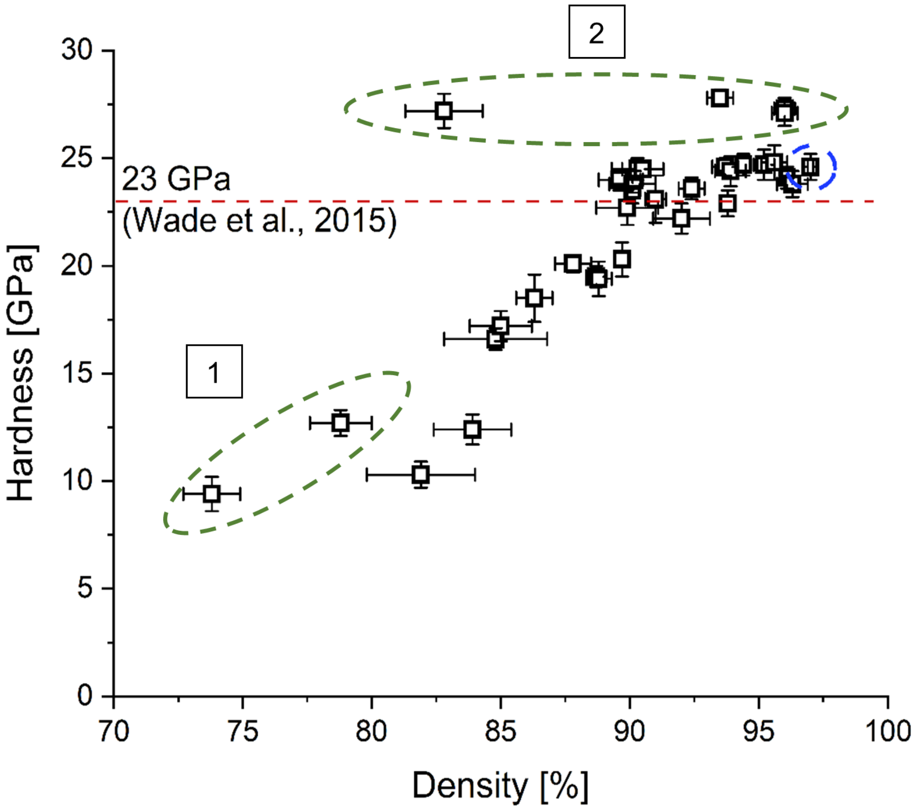

Figure 5.2: Vickers hardness (HV5) against density for all flash sintering parameters tested in this work. The conventionally sintered sample (fire 1) is shown in the blue dashed circle. For reference, the Vickers hardness of SiC (from a test with a similar indentation load) from the literature is indicted by the red dashed line. The green dashed ellipse 1 represent samples whose microstructures were affected by N_2 and Ar+5%H_2 atmospheres, while the samples in ellipse 2 had additional C in the furnace tube while sintering (described in chapter 3)

As shown in Fig. 5.2, the Vickers hardness of a specimen was generally dependent on the sample density that was achieved through use of different flash sintering parameters. This dependency diminished for higher specimen densities; once the sample reached a hardness of ∼24 GPa, or ∼90% density, any further increase in density did not improve the hardness of specimens. This value was just above the hardness expected from the literature of the same SiC powder[73] (red dashed line, Fig. 5.2) and was the same as that achieved by the conventional sintered SiC samples in this work (blue dashed circle). It should be noted that the density of each sample is a bulk density; the indents were made at the centre of the sectioned sample which was almost always denser than its edge.

Outliers in the data are highlighted in green ellipses in Fig. 5.2. The sintering conditions of these tests produced samples with the lowest and the highest hardness values of all the tests. Those in ellipse 1 were produced using N_2 and Ar + 5 %H_2 atmospheres, with the N_2 atmosphere producing the lowest hardness of any sample at (9.4 GPa ± 0.8 GPa). These low values are likely a consequence of the low density of these samples. Those in ellipse 2 had additional C in the system during sintering. These specific samples exhibited significantly (>2 std. err.) higher hardness values than those achieved through conventional sintering of the same powder (24.6 GPa ± 0.6 GPa, fire 1). The highest hardness achieved of all tests was 27.8 GPa ± 0.4 GPa of the sample produced using the mirror 2 set up. The atmospheres that affected the densities and microstructures of these samples are discussed in section 4.1.6. As such, these results should be treated differently from the rest of the results in Fig. 5.2, the microstructures of which were predominantly affected by heating and thermal gradients, and not by additional atmospheric conditions. It should be noted that not all samples with additional C in the sintering atmosphere exhibited this increase in hardness (further discussed in section 5.1.2.3).

5.1.1.3 Effect of grain size on Vickers hardness

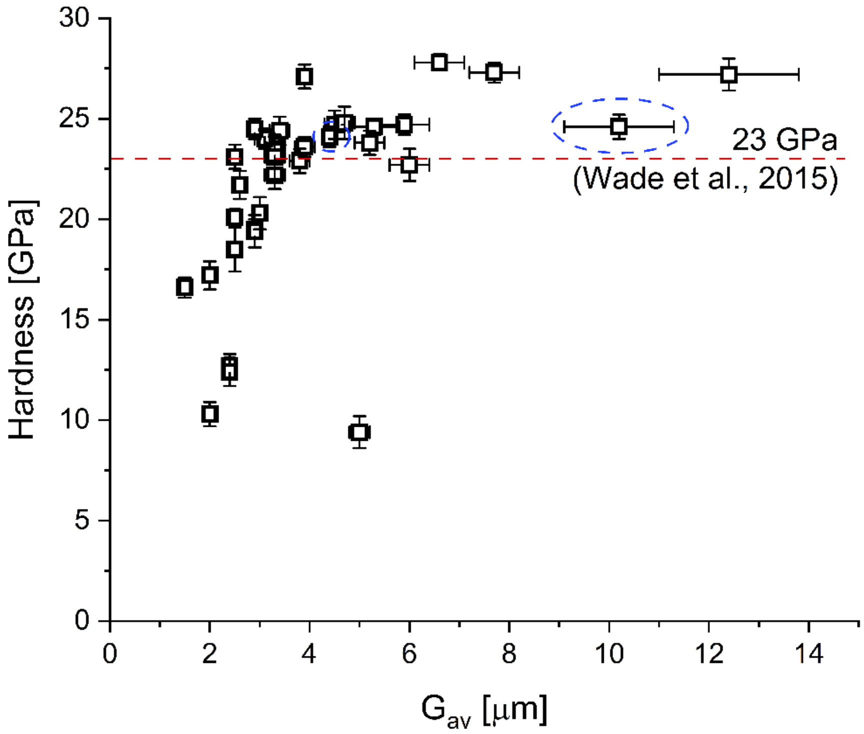

Figure 5.3: Vickers hardness of all flash sintered samples, with samples that were conventionally sintered given in blue ellipsis and super-hard SiC shown in the green ellipsis.

As shown in Fig. 5.4, the Vickers hardness of most of the SiC samples tested in this work increased with grain size until ∼24 GPa (∼90% bulk density), after which there was little dependency between the two. Although the super-hard SiC specimens did surpass this ∼24 GPa threshold, there was still no correlation between the hardness and grain size of these samples (green ellipse). Samples of very low hardness (bottom left in Fig. 5.4) were very porous.

5.1.1.4 Atom probe tomography results

The atom probe tomography results presented here are the work of a previous DPhil student – Dr J. Singh[144] - who performed analysis on the SiC samples produced by the present author.

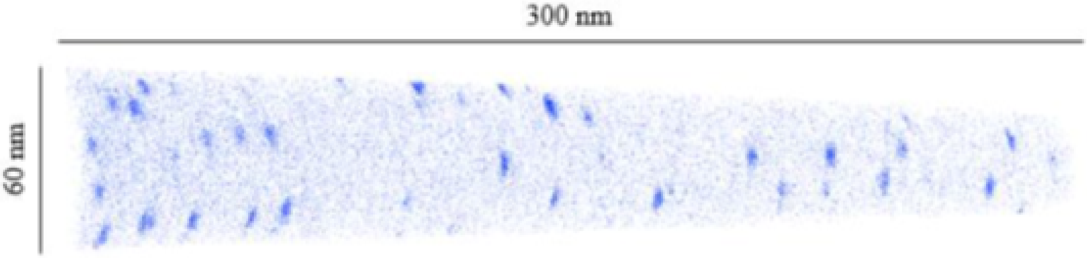

Figure 5.4: A reconstruction of an atom probe tip taken from the centre of a grain in a super-hard SiC sample (produced using mirror 2 set up, also lablled as FS Hard in APT results). Blue data points indicate B atoms, with clear signs of clustering.

Figure 5.4 shows a dispersion of blue clusters in a super-hard SiC specimen (labelled FS Hard in the APT work, but was created using the mirror 2 set up) that were identified as “boron rich clusters”. The nominal composition of these clusters is given in Table 5.1. However, due to atom probe artefacts, the B content of the clusters may have been underestimated. The slight plate-like form of the clusters normal to the analysis direction may be the result of an electric field artefact. While these clusters were observed in conventionally sintered specimens (fire 1 and 2, section 3.5), and in a flash sintered (FS) specimen (400 W, stepped heating, section 3.3), all with “normal” hardness values, their occurrence was far less frequent in these specimens than in the super-hard specimen (FS Hard). This is shown in Fig. 5.5 through binomial grid-based frequency analysis of the boron clusters in the APT tip reconstruction. The small amount of B in the starting powder (0.5wt.%) is below the resolution of

Sample	Silicon (%)	Carbon (%)	Boron (%)
FS Hard	20.6 ± 0.4	21.4 ± 0.5	57.9 ± 0.6

Table 5.1: Averaged, relative atomic composition of clusters in super-hard SiC grains (FS Hard, or Mirror 2).

the XRD technique, which explains why B is not detected in any of the XRD scans in Chapter 4.

APT analysis of the grain boundaries in all SiC samples showed greater concentrations of B at grain boundaries than in the bulk grain. Super-hard Flash Sintering (FS) and conventionally sintered SiC had similar concentrations of B at grain boundaries, while SiC of normal hardness showed a smaller amount: this was attributed to the low density of the sample.

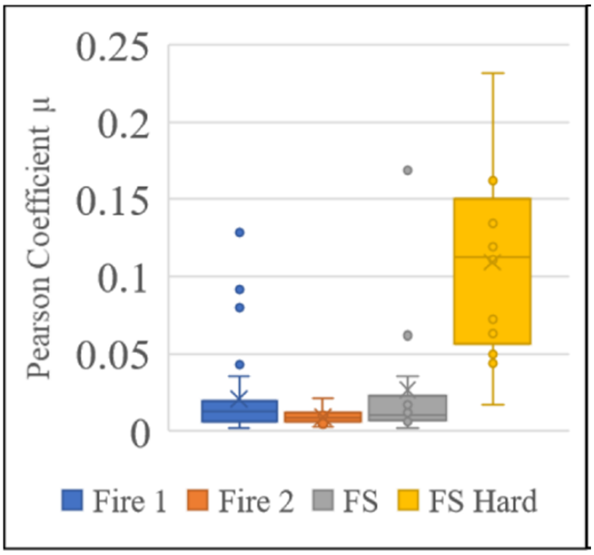

Figure 5.5: Binomial grid-based frequency analysis of SiC grains, showing the Pearson correlation between B clustering and the processing technique. Fire 1 and 2 refer to samples that were conventionally sintered. FS refers to SiC that was flash sintered using the 400 W heating schedule without carbon additions. FS Hard refers to samples heated with the 550 W flash sintering schedule and using the mirror 2 set up (section 3.2).

5.1.2 Discussion

5.1.2.1 Effect of density on hardness

As indicated in Fig. 5.2, Vickers hardness correlates with density up to approximately 90%, after which there was no further increase in hardness as density increased. It is suggested that once the mean density of a sample reached ~90% dense, the centre of that specimen was almost fully dense, and it was the porous edge that resulted in a low bulk density measurement (discussed throughout chapter 4). As a result, the hardness of the centre of the sample had reached what could be expected of dense SiC from the literature (see below). Any further increase in density only decreased porosity at the specimen's edge, which did not affect the hardness at the centre of the specimen and hence no further increase in hardness was achieved for higher densities.

The values of hardness reached after ~90% bulk density are higher than those reported by Wade et al.[73] for SiC of similar density using the same indentation load (approximately 22 GPa and 94% for coarse grained specimens and 23 GPa and 96% for fine grained specimens). Magnani et al.[40] measured a hardness of 23.4 GPa ± 0.7 GPa (10 kgf) for 97% dense samples made by pressureless sintering of the same powder as was used here. Microstructural comparisons between a flash sintered sample (550W, Fig. 4.3, 24.7 GPa ± 0.7 GPa) and that produced by Magnani show similarly low levels of porosity at the centre of the samples, where Vickers indents were made. Vickers hardness values of the samples were within error of each other. It is concluded that flash sintering created SiC that was at least as hard as conventionally sintered

SiC.

As can be seen in Fig. 5.2, the samples in ellipse 1 had a lower density but similar hardness values to other specimens. It is suggested that this is primarily a result of the atmospheric conditions that these specimens were produced in. These samples had very rough surfaces and low density as a result of chemical reactions at the surface of the sample during sintering (reactions discussed in section 4.1.6). Consequently, the surface absorbed more water and increased the saturated weight of the samples during the Archimedes density tests. This lowered the apparent density of these samples compared with those of samples produced in non-reactive atmospheres. The centres of these samples were less affected by atmospheric conditions and hence the specimens were of similar hardness to those produced in non-reactive atmospheres. It should be noted that the centres of these samples were not dense, and hence all these samples had low hardness values.

As shown in Fig. 5.2, the dependency of hardness on density diminished after ∼90% mean density was reached. However, it was possible to increase the hardness further by the addition of C into the sintering atmosphere (Fig. 5.2, green ellipse 2). The effect that C had on the hardness of SiC in this work shall be discussed in the context of average grain size, a C threshold, SiC polytype concentration and submicron B inclusions.

5.1.2.2 Investigation of super-hard SiC: effect of grain size

	400 W 30 min hold	Mirror 2 set up
Hardness [GPa]	24.4 ± 0.2	27.8 ± 0.4
Mean density [%]	93.2 ± 0.2	93.6 ± 0.4
Grain size [μm] (centre)	3.4 ± 0.2	6.6 ± 0.5

Table 5.2: Averaged, relative atomic composition of clusters in super-hard SiC grains.

For convenience, the properties of two flash sintered specimens that were discussed previously are given in Table 5.2: a sample sintered according to the 400 W, 30 min hold time schedule and that sintered using the mirror 2 set up. This comparison shows that despite the mirror 2 sample having a similar density to that of the 400 W 30 min hold specimen and an average grain size that was almost double, the mirror 2 specimen had a significantly higher hardness (27.8 GPa ± 0.4 GPa (mirror 2) vs 24.4 GPa ± 0.2 GPa (400 W 30 min)).

Hardness often obeys a conventional Hall-Petch relationship with grain size; however, Fig. 5.4 indicates that the SiC samples in this work deviated from this theory. The increase in hardness with grain size seen in samples with grain sizes below ∼4 µm can be attributed to the low densities of these samples (discussed in section 5.1.2.1). Any increase in grain size beyond this point did not affect the hardness of the samples, contrary to the Hall-Petch relationship. This behaviour has been seen before by Magnani et al. who sintered the same SiC powder as used in this work using a conventional, slow heating profile (similar to fire 1 heating schedule, section 3.5) and using a two-step sintering profile[40]. Although they do not explicitly measure grain sizes, their micrographs clearly show that the heating schedules produced samples with significantly different grain sizes, with the conventionally sintered sample having the larger size. Despite this significant difference in grain size, the Vickers hardness values of the samples remained within experimental uncertainty of one another. This lack of correlation between grain size and hardness is observed in super-hard specimens as well (green ellipse, Fig. 5.4). It is suggested that a Hall-Petch effect is not observed due to the comparably larger resistance of dislocations movement and twinning in covalently bonded SiC. It is concluded that changes in average grain size are not the determining cause of the super hard SiC.

5.1.2.3 Investigation of super-hard SiC: effect of the carbon furnace additions

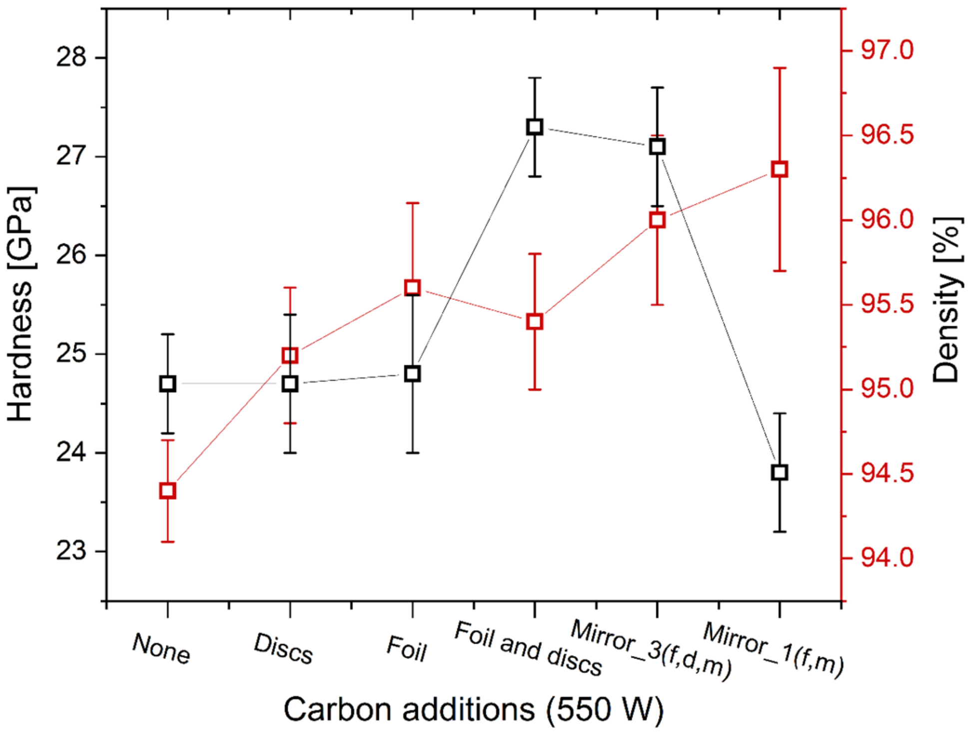

Figure 5.6: Plotted are data from section 5.2 that shows the effect that the individual components of the mirror set up had on the Vickers hardness of flash sintered SiC. All samples were sintered using the 550 W power schedule. The experimental setups are described in section 3.2.2. The letters in brackets indicate: f, foil, d, disc and m, mirrors.

Figure 5.6 indicates that the inclusion of either C discs or foil alone was not sufficient to cause an increase in hardness, but the combination of both was. The combination of C discs and foil increased the hardness to greater than 27 GPa from approximately 25 GPa when only the foil or discs were used individually. Including the mirrors (which raised the sample temperature, section 4.2.3.2) with the foil and discs (mirror 3) did not affect the hardness. Hence, the super-hardness of SiC was not caused by an increase in sample temperature above 2205 °C. Instead, it is suggested to be caused by a C threshold: a critical amount of C in the atmosphere, somewhere between that introduced by the sole addition of the C foil and that of the C foil and disc set up. This is true at the normal sintering temperatures (∼2205 °C) and at the higher sample temperatures caused by the inclusion of mirrors (>2205 °C). When only the foil was used (mirror 1), the hardness was 23.8 GPa ± 0.6 GPa but once the discs were also included in the setup, the hardness increased to 27.1 GPa ± 0.6 GPa.

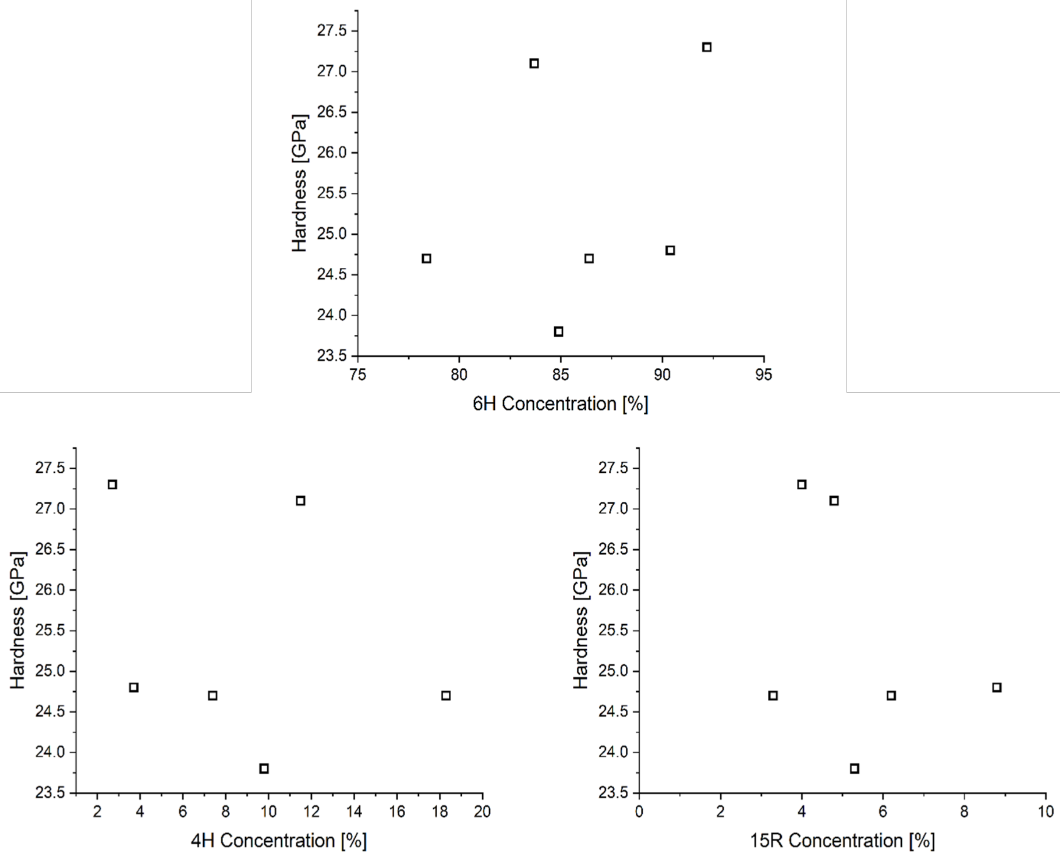

Figure 5.7: Polytype concentration in samples flash sintered using the 550 W power schedule with different C additions. The XRD scans and Rietveld analysis are shown in section 3.2.2.

To investigate this threshold further, Rietveld analysis was performed on XRD spectra from the samples described in Fig. 5.6, and the relative concentrations of the three SiC polytypes in the specimens that were identified from the analysis are shown in Fig. 5.7. All indicate that there is no correlation between Vickers hardness and SiC polytype concentration. This is corroborated by density functional theory modelling performed by W.-W. Xu et al. who show that although SiC polytypes may affect sample properties like Young's Modulus, the different polytypes are not predicted to have different Vickers hardness values[161].

5.1.2.4 Investigation of super-hard SiC: submicron boron inclusions

TEM analysis of inter-grain inclusions in hot pressed SiC with Al, B and C sintering additives has been conducted by Zhang et al.[44]. Their investigation showed that aluminium rich phases were found at triple junctions and grain boundaries, while intra-grain inclusions were identified as B rich phases. They suggest that unlike the aluminium rich phases, which exhibit wetting behaviour and cover grains, the B rich phases were non-wetting and formed spherical inclusions in the SiC grains. The inclusions range in size from 0.03 µm to 0.7 µm, with higher annealing temperatures resulting in larger inclusions.

Zhang et al. hypothesise that some of the grain boundary phase is incorporated into the grain as grain growth occurs. In this work, there was no discernible difference between the concentration of B in the centre of the conventionally sintered fire 1 and fire 2 specimens, despite the 6 h longer heating schedule of the former. APT analysis of the grain boundaries in these samples shows there was no significant difference in B concentration at grain boundaries of the two samples. This suggests that even at sintering temperatures, diffusion of B in the SiC grains (after the solubility limit was reached) was limited and hence nucleation is unlikely to have led to the precipitation of B inclusions within the SiC grains. The growth of the inclusions with increasing annealing temperature found in further work by Zhang et al., is likely due to the long annealing times (840 h) used in that work.

As concluded by Zhang et al., it is suggested that the non-wetting behaviour of the B rich secondary phase in flash sintered SiC resulted in portions of this phase being enveloped by SiC as grain growth occurred.

Alloys of B_4C-SiC have been investigated previously and super-hard SiC alloys were reported[45,75–77]. Each investigation produced B_4C-SiC through different processing routes (CVD, pressureless sintering and hot pressing) and a common processing variable/heating schedule cannot be identified between each of the tests. While this shows that super-hard SiC is not a unique product of flash sintering, the simplified flash sintering apparatus is advantageous over that used by others: Meerson et al. described their hot press set up as "expensive and impractical from a technological point of view"[76]. Using a conventional furnace with a single heating cycle and without pressure, the flash sintering technique could drastically reduced the overhead costs of producing dense super-hard SiC, an attractive attribute if the technique was to be commercialised.

Kieffer et al. suggest that dispersion hardening by sub-microscopic separation of SiC and B_4C phases is responsible for the super-hardness that they observed of B_4C-SiC "alloys"[75]. Shaffer et al. showed that no higher hardness than that of B_4C can be reached from a B_4C-SiC alloy[45]. It is suggested, akin to the conclusion of Kieffer, that the greater concentration of B clusters identified in the super-hard SiC samples in this work resulted in dispersion hardening, which was the cause of these samples' high hardness values.

5.1.2.5 Investigation of super-hard SiC: C thresholds and boron rich clusters

While the exact mechanisms that lead to a greater concentration of B clusters in the super-hard flash sintered SiC are still unclear, the following is given as a tentative hypothesis to describe their formation and help elucidate the reasons why a carbon rich atmosphere in combination with the 550 W heating schedule led to exceptionally high Vickers hardness values of SiC.

Firstly, on the formation of the clusters. The low solubility of B in SiC[162] makes it unlikely that the clusters are precipitates. There is no evidence in the available phase diagrams to suggest that B was significantly more soluble at lower temperatures either, which might have allowed the B to dissolve at lower temperatures and precipitate at higher ones.

Despite the significantly different sintering times of the SiC samples that were analysed using APT, all samples apart from the super-hard SiC samples exhibited a similar degree of B clustering and B concentration at the grain boundaries. This suggests that B did not diffuse to or from the clusters, as the clusters would either be bigger in the conventional fire 1 sample (long sintering time) due to Oswald ripening or would have disappeared by the B diffusing to the grain boundary.

The heating rate of all samples in the 'Effect of furnace carbon additions' investigation (section 5.1.2.3) was the same, and hence it could not bear sole responsibility for the greater concentration of B clusters in the super-hard samples. The slow diffusion of B in SiC suggested by the APT analysis above also suggests that the heating and cooling rates may not be important in the formation of the clusters.

Zhang et al. analysed hot pressed SiC with Al, B, and C sintering additives using TEM and nEDS[44,163]. They observed nanoscale secondary inclusions throughout the SiC grains that were rich in secondary phases and concluded that the nonwetting secondary phases were incorporated into the grains during grain growth to form spherical inclusions. They also observed that the size of the clusters only grew once SiC had spent a significant time at sintering temperatures (~840 h). This is similar to the results in this work where sintering time did not affect the B clustering in the conventionally sintered SiC. Given this similarity, it is suggested the B clusters in the samples in this work did not form through precipitation. Instead, it is hypothesised that the B clusters found in the SiC in this work were formed by a similar mechanism as proposed by Zhang et al. and were enveloped by the SiC grains during grain growth at sintering temperatures.

It was shown that a C rich atmosphere greatly affected the microstructure of flash sintered SiC and is assumed to have done so by affecting the grain boundary phase during sintering. The B_4C-SiC pseudo-binary[45] and ternary phase diagrams[46] suggest that the additional C in the sintering atmosphere may have partially solidified the B liquid phase during flash sintering. This might have affected the wetting behaviour of the liquid phase and resulted in more clusters of the B phase being enveloped by the SiC grains as growth occurred. This may explain why the “FS Hard” specimen

(Mirror 2), that was flash sintered in a sufficiently rich C atmosphere, exhibited a greater concentration of B clustering than the rest of the samples that were analysed using APT. However, further work is needed to better understand the balance between solidification of the B phase by the C rich atmosphere and sample temperature.

In summary, it is suggested that a C rich atmosphere modified the wetting behaviour of the B liquid phase. As the SiC grains grew, they enveloped this partially solid phase which formed the observed spherical inclusions dispersed throughout the grain. The effect of heating rate on their formation and the chemical interaction between atmospheric C and the B liquid phase require further investigation.

5.2 Flexural strength and fracture toughness

5.2.1 Results

5.2.1.1 Loading curve analysis

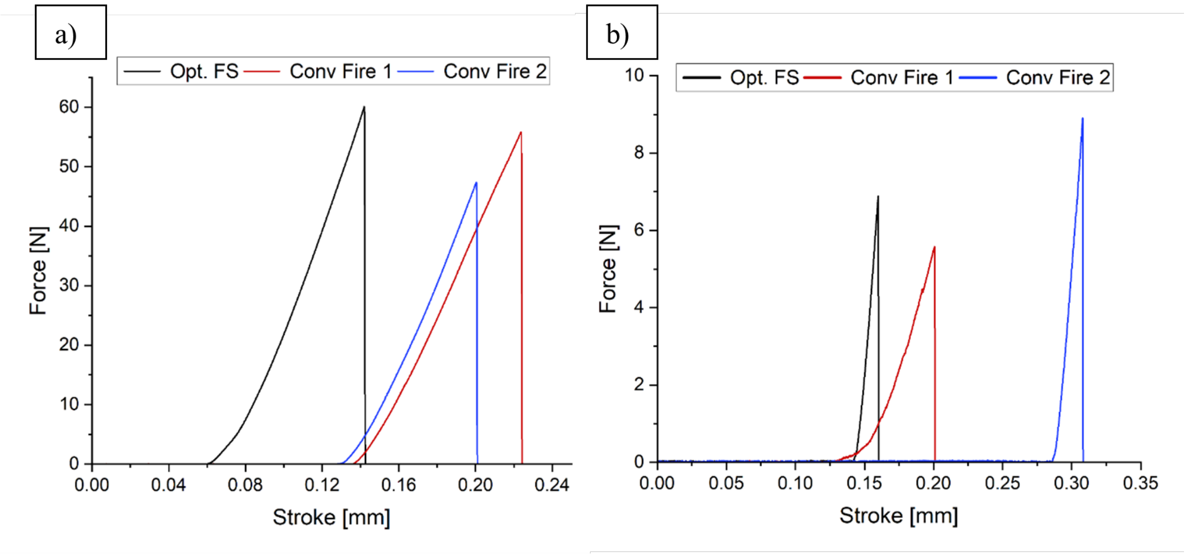

Figure 5.8: Representative loading curves of SiC processed in three different ways, during a) 3-point flexural strength tests and b) SEVNB toughness tests.

The loading curves shown in Fig. 5.8a and 5.8b are indicative of brittle fracture, as is expected of ceramic materials. The shallower gradient of the fire 1 sample from the SEVNB tests is likely a consequence of the slightly smaller average sample size of the samples in this test series.

5.2.1.2 Flexural strength and fracture toughness comparisons

Table 5.3 shows that while the average flexural strengths of the samples were within experimental error of each other, the fire 2 sample might have been the weakest of the materials at 520 MPa ± 33 MPa. Equation 3.2 was used to calculate the strengths. All average strengths had similar standard errors.

Sample	Average flexural strength [MPa]	Average fracture toughness [MPa $m^{1/2}$]
Conv fire 1	571 ± 38	2.7 ± 0.6
Conv fire 2	520 ± 33	2.1 ± 0.5
Optimised FS	576 ± 32	2.9 ± 0.4

Table 5.3: 3-point flexural strength and SEVNB toughness comparisons of conventionally sintered and flash sintered SiC.

Table 5.3 also shows the effect of sintering technique on the fracture toughness of SiC. While the average toughness of each specimen was within experimental uncertainty of one another, the upper bound of the error associated with the toughness of the conventional fire 2 specimen was just within the lower bound of the error on the toughness value of the FS specimen. The toughness of the fire 2 specimen may have been lower than that of the FS sample. Toughness was calculated using Eqn. 3.3.

5.2.1.3 Fracture surface comparison

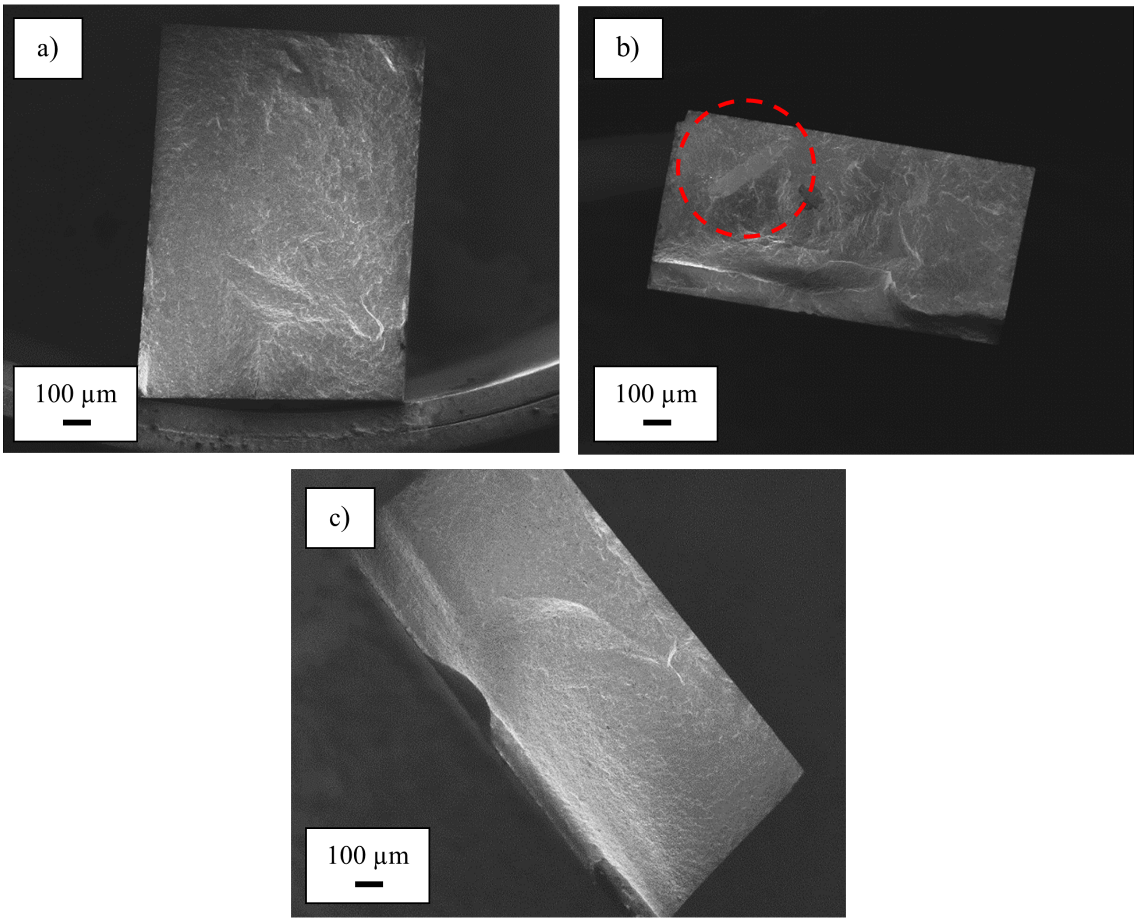

Figure 5.9: Representative SEM images of a fracture surface of a) a flash sintered sample, b) a conventionally sintered fire 1 sample and c) conventionally sintered fire 2 sample after a 3-point bend test. The red dashed circle shows a large, macroscopically smooth area.

As shown in Figs. 5.9a and 5.9c, the macroscopic fracture surface of a flash sintered sample and that of a conventionally sintered fire 2 sample were similar. The fracture surfaces of the FS and fire 2 are shown in Figs. 5.10a and 5.10b, respectively. Both show transgranular fracture with evidence of cleavage steps.

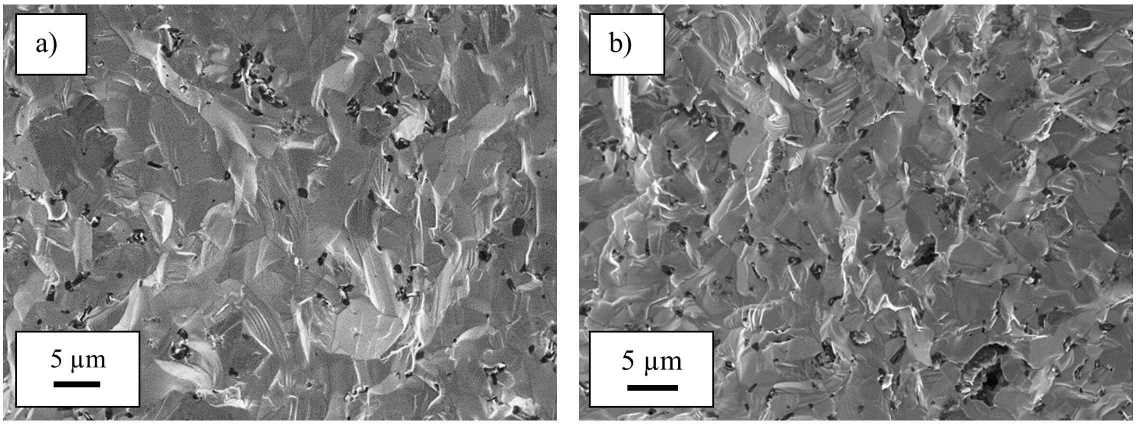

Figure 5.10: Fracture surfaces of a) a flash sintered sample and b) a sample made using the conventional fire 2 sintering profile.

5.2.2 Discussion

5.2.2.1 Brittle fracture in SiC

All SiC specimens had flexural strength values that were higher than those reported in the literature on BC-SiC. The same powder that was used in this work was conventionally sintered without pressure at 2200 °C for 1 h by Magnani et al.[40]. They report a flexural strength of 341 MPa ± 43 MPa using a 4-point bend test. Sample dimensions were 2 mm x 2.5 mm x 25 mm and used a 4-point rig with a 20 mm support span. Akin to the SiC processing in this work, they cold isostatically pressed their greenbody samples at a pressure of 200 MPa. Ghosh et al. used a 3-point bend test to show that their commercially available α-SiC samples (Hexoloy SA, Carborundum, [3 mm x 3 mm x 30 mm, 20 mm span]) had a flexural strength of 350 MPa[164].

The discrepancy between the values in Table 5.3 and those reported by Magnani or Ghosh is likely caused by the smaller sample dimensions in this work. These resulted in a smaller volume of the sample under maximum tensile stress. Additionally, a 4-point test creates a greater volume of sample under maximum tensile stress than that created using a 3-point bend rig. These factors reduced the probability of the largest flaw being within this volume on the face of the sample under tension and hence the SiC samples in this work had higher flexural strengths than that achieved by Magnani or Ghosh.

The strength values of each sample are within experimental error of one another, and hence the heating schedule did not significantly affect the strength of SiC. The results shown by Kim et al. demonstrate that grain size and shape do not significantly affect the flexural strength of α-SiC with varying β-SiC concentrations, owing to the strong interfacial bonding between SiC grains[21]. The similar standard errors of all the tests in this work suggest that, compared with conventional sintering, flash sintering did not introduce any substantially larger flaw into the specimens during sintering and hence did not degrade the flexural strength of SiC. This correlates with the results in Table 5.4, which show that critical flaw sizes in all samples were similar.

However, the relative size of the critical flaws to the average grain size of each sample might indicate what type of flaw caused failure in each sample (calculated using Eqn. 3.6). The grain sizes of the FS and fire 2 specimens are smaller than the calculated critical flaw size for either specimen (Table 5.4), which might suggest that a processing defect was responsible for failure. It was not possible to conclusively tell what type of defect caused failure in the specimens in this work.

Sample	Critical flaw size (µm)	Mean grain size (µm)
Conv. fire 1	14	10.2 ± 1.1
Conv. fire 2	10	4.0 ± 0.2
Optimised FS	16	4.5 ± 0.4

Table 5.4: Critical flaw sizes in SiC samples (semi-circular edge crack).

Toughness values of SiC from the literature are shown in Table 2.1. Results using a range of methods is given for context, but the most direct comparisons with the toughness values in this work (Table 5.3) are with those that used the same 3-point SEVNB technique. Both fracture toughness values recorded by Wang and Rao (3.2 MPa $m^{1/2}$ ± 0.2 MPa $m^{1/2}$ and 2.7 MPa $m^{1/2}$, respectively) are within experimental error of that measured for the conventionally sintered, fire 1 SiC specimen in this work (2.7 MPa $m^{1/2}$ ± 0.6 MPa $m^{1/2}$). Both authors reported coarse microstructures, as is the case for the fire 1 specimen (section 4.1.7). While this gives some confidence in the values of the control specimen in this work (fire 1), errors in the toughness values of any of the SiC samples in Table 5.3 could have arisen from the assumption of a perfectly sharp crack when calculating the toughness values and the measurement of notch length. These sources of uncertainty likely explain the large error values associated with the toughness values in Table 5.3. The higher values obtained using the SEVNB technique in this work over those from the Single Edge Pre-cracked Beam (SEPB) results is likely due to the use of a notch in SEVNB as opposed to a sharp crack in SEPB.

While some care should be taken when comparing the values in this work with those in the literature due to non-standardised sample sizes; there is broad agreement between the data, which should give some confidence in the results in Table 5.3.

Similar fracture surfaces of the same SiC used in this work were reported by Magnani et al.[40]. They show that a sample produced using a slow heating rate and a long hold time produces SiC that fractures transgranularly. Using a two-step heating profile they produced a sample with far smaller average grain size and the fracture surface of this sample showed evidence of inter and trans-granular fracture. This suggests that the large flat areas on the fire 1 fracture surface (red circle, Fig. 5.9b) that were not present on the fire 2 or FS sample surfaces, were likely a consequence of the larger grain sizes of the former specimen.

However, despite the highly bimodal microstructure of the long hold specimen, Magnani et al. also show that there is no significant change in toughness between samples. Similarly, the toughness value of the fire 1 specimen is within experimental error of that of fire 2, and the FS specimen. The large flat areas did not considerably affect the fracture toughness of this specimen. Kim et al. also show that limited crack deflection occurs in fine grained α-SiC and that the fracture toughness of α-SiC doped with varying amounts of β-SiC is independent of grain size and shape[21]. Hence, despite the slightly different fracture surface of the fire 1 specimen, it suggested that the fracture mode was broadly similar between all samples (predominately transgranular with some intergranular) and explains why their toughness values were similar.

5.3 Armour Discussion

As shown by Kieffer et al. and from the work in this Chapter, the hardness of SiC can be increased above that typically documented for BC-SiC[75]. Wade et al. showed that armour grade SiC had a Vickers hardness of ∼23 GPa[73], while that of the super-hard SiC in this work could reach ∼28 GPa under a similar load. Given that hardness has been suggested to be an important property in determining the ballistic performance of an armour ceramic[92], it might be reasonable to hypothesise that the super-hard flash sintered SiC in this work may outperform typical SiC ballistic armour. As a hard ceramic plate defeats a softer incoming projectile by eroding the surface of the latter, increasing the hardness of the ceramic plate may improve protection against armour piercing rounds with cores made of hard materials, such as hardened steel[89] and WC[165].

Hardness alone does not guarantee good ballistic performance of ceramic armour, but as shown, flash sintering has not degraded the strength or the toughness of SiC, which may give some confidence in the above hypothesis. However, additional B clusters in the super-hard SiC may affect other relevant properties of the material and requires further investigation.

As an armour ceramic, B_4C has advantages over SiC ballistic plates, namely its greater hardness and lower density. However, B_4C is prone to suffer from amorphisation during a ballistic event[96]. Given that the hardness of SiC can be increased through what has been suggested to be dispersion hardening, it may be possible to create armour that is as hard as B_4C but that does not deteriorate in a similar manner during a ballistic trial.

While flash sintering might lower the cost of producing such armour, it cannot reduce the density of SiC which makes it less attractive than B_4C ballistic plates. However, if the FS-SiC material does perform better during ballistic trials, FS-SiC plates might be made thinner than the SiC plates that are used currently, which would reduce areal density.

Despite the potential of increased performance and reduced costs, other factors need to be considered in selecting armour: what type of threats might be encountered; how the plates are attached to the armour system; and how the armour affects other functions such as structural components, or manoeuvrability.

5.4 Conclusions

The Vickers hardness of most of the SiC samples in this work was shown to be dependent on density and average grain size up to ∼90% bulk sample density and ∼4 µm, respectively, which corresponded to a hardness of ∼24 GPa. After this, the dependency of hardness on either property diminished. Atmospheric conditions were shown to affect the hardness of SiC; the inclusion of C additions in the furnace tube during sintering increased the Vickers hardness of SiC significantly above that achieved through conventional sintering of the same powder and SiC in the literature. The highest hardness achieved was 27.8 GPa ± 0.4 GPa of the sample produced using the mirror 2 set up. The underlying mechanism that led to this super-hard SiC was shown to be independent of density, grain size and polytype concentration but is suggested to be related to a C concentration threshold in the sintering atmosphere. APT analysis indicated that the super hard SiC samples had a greater concentration of B rich clusters than SiC of regular hardness, which are suggested to cause dispersion hardening in these samples. The exact mechanistic details of how a C rich atmosphere creates more of these B rich clusters needs further investigation.

A comparative study of specimens sintered using conventional fire 1, fire 2 heating schedules and an optimised flash sintering schedule indicated that the 3-point flexural strength and fracture toughness of SiC were largely independent from the tested heating schedules. It is concluded that flash sintering did not degrade the strength or the toughness of SiC.

Due to its higher Vickers hardness and similar strength and toughness, once an optimised flash sintering schedule is established that could create large SiC armour plates, they may outperform traditional SiC armour plates in a ballistic trial. However, properties of the former such as the elastic modulus still requires investigation, and due to intrinsic material characteristics, such as its density, flash sintered SiC may not be the optimum choice of ceramic ballistic plate in all scenarios.

Chapter 6

Electrical response of silicon carbide during flash sintering

This chapter investigates the underlying mechanism that initiates flash sintering in SiC and discusses the effect of the electric field and current on its microstructure. Previously, a thermal runaway model has been shown to accurately characterise the electrical and thermal response of oxide ceramics. The same model is applied to electrical results of SiC during flash sintering to better understand the electrical characteristics of a non-oxide ceramic during the same process.

6.1 Results

6.1.1 Electrical response at constant voltage

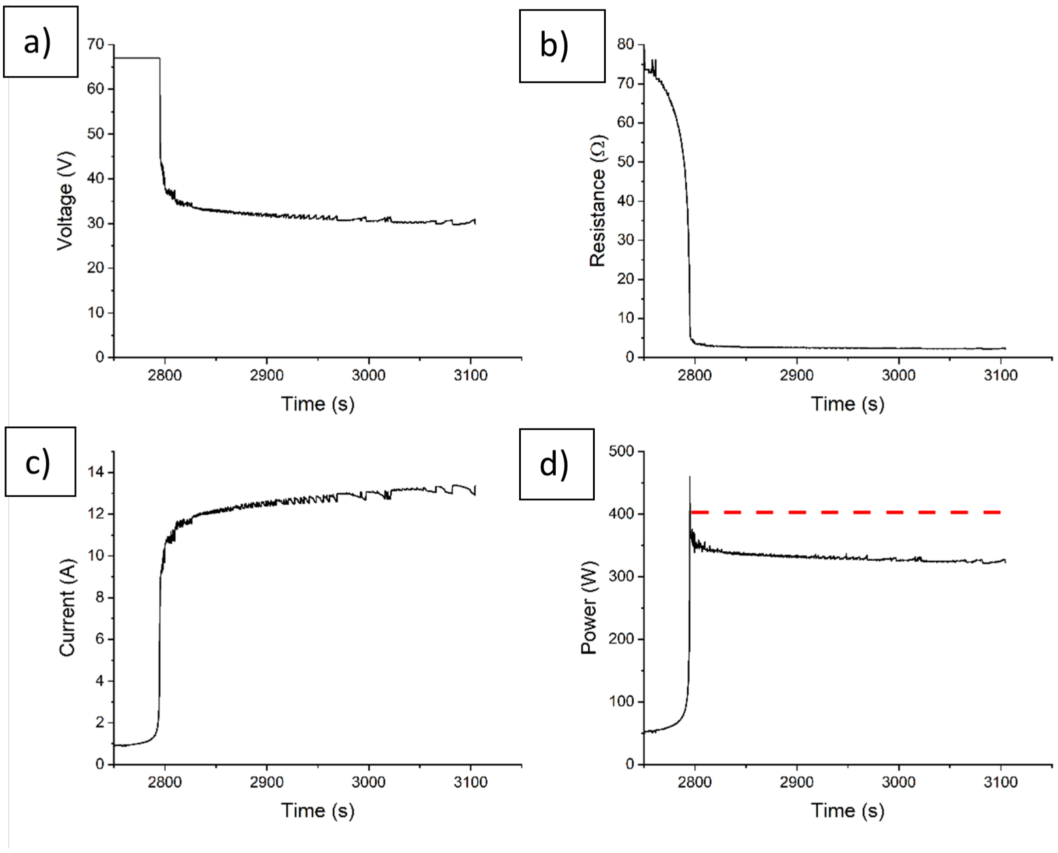

Figure 6.1: The electrical response of a SiC specimen during a constant voltage (initial field 30 V cm^{-1}), furnace ramp experiment around runaway. a) voltage, b) resistance, c) current and d) the power dissipated in the sample (total power including W wires represented by the dashed line). Sample temperature and other details are given for all constant voltage tests in Table 6.1

The electrical response from a sample during a typical constant voltage experiment is shown in Fig. 6.1. Resistance decreased with time and consequently there was an increase in current flow and the power dissipated within the specimen. The current increased slowly at first but rose more rapidly as the “flash event”[16] was approached, i.e. the characteristic electrical signature of flash sintering (~2790 s, Fig. 6.1). The furnace temperature at this flash point was 1032 °C ± 2 °C (the critical furnace temperature, section 3.3). Resistance dropped by a factor of ~25 compared with that of the green body immediately prior to the flash event. Once the power reached the predetermined limit of 400 W, the voltage was moderated by the power supply to maintain the total power at this level. As a consequence of the reduction in sample resistance, a greater a proportion of the total power was dissipated in the wires and hence a drop in power dissipated within the sample was observed during the isothermal hold period.

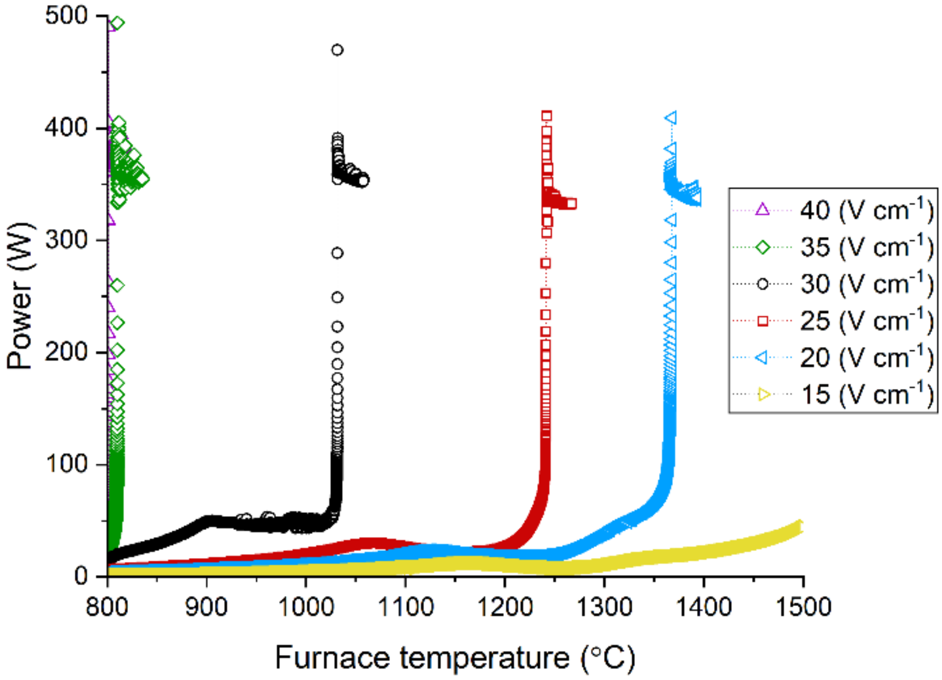

Figure 6.2: Power dissipated in specimens against furnace temperature during constant initial electric field experiments, for varying electric field strengths.

Figure 6.2 shows the effect of the electric field strength on power dissipated within specimens in the constant voltage tests. Lower electric field strengths required higher furnace temperatures to initiate flash sintering. The 15 V cm^{-1} specimens did not reach the flash event before the maximum furnace temperature of 1500 °C was reached. All other samples were held at a nominal power limit of 400 W for 5 min.

Electric field strength (V cm^{-1})	Furnace temp at runaway (°C)	Sample temp during hold (°C)	Density (%)
15	n/a	n/a	n/a
20	1364 ± 3	2085 ± 26	86.4 ± 0.5
25	1243 ± 2	2075 ± 26	81.5 ± 0.7
30	1032 ± 2	2020 ± 25	78.4 ± 0.7
35	820 ± 3	2010 ± 25	74.3 ± 1.3
40	802 ± 3	2005 ± 25	72.2 ± 0.8

Table 6.1: Furnace temperatures at runaway, sample temperatures during the isothermal hold stage and final specimen densities for varying initial electric field strengths in constant voltage experiments.

Runaway occurred within ~60 s for field strengths of 35 V cm^{-1} and 40 V cm^{-1}. All other specimens displayed a maximum in power (undulation) before the flash event.

The results in Table 6.1 indicate that the higher furnace temperatures at the flash event for lower initial electric fields resulted in higher sample temperatures and final sample densities. The highest density reached in this test series was 86.4% ± 0.5% by the 20 V cm^{-1} test with a sample temperature of 2085 °C ± 26 °C.

6.1.2 Resistivity-temperature relationship

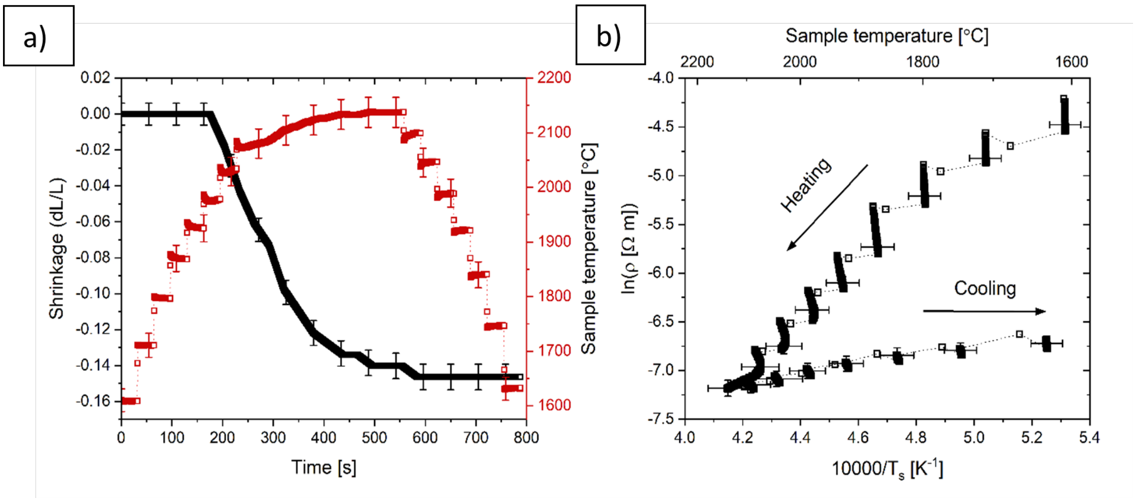

Figure 6.3: a) Specimen shrinkage (black) and sample temperature T$_s$ (red) against time and b) the corresponding inverse Arrhenius graph of resistivity during an isothermal, stepped power test to a power limit of 400 W at a furnace temperature of 1500 °C. The sample was cooled at the same rate as it was heated. The effects of sample shrinkage and resistance in the wires were incorporated into the specimen resistivity and temperature calculations. For clarity, error bars are only included for a small proportion of data points.

Noticeable shrinkage occurs at 180 s in Fig. 6.3a. At this point the specimen temperature was 1975 °C. Most of the shrinkage occurred before the power was ramped down, roughly 400 s after the onset of shrinkage. Figure 6.3a indicates that a peak sample temperature of 2135 °C ± 27 °C was reached and a maximum isotropic shrinkage of 15% was achieved.

Figure 6.3b shows the corresponding inverse Arrhenius plot for resistivity of the sample during the stepped power test in Fig. 6.3a. The electrical resistivity of the specimen decreased significantly as it was heated but there was little change during cooling. During heating, the resistivity of the sample continued to reduce during each constant power hold stage. Sample resistivity had reduced by a factor of ~18 by the end of the test compared with the specimen at the same temperature before the test.

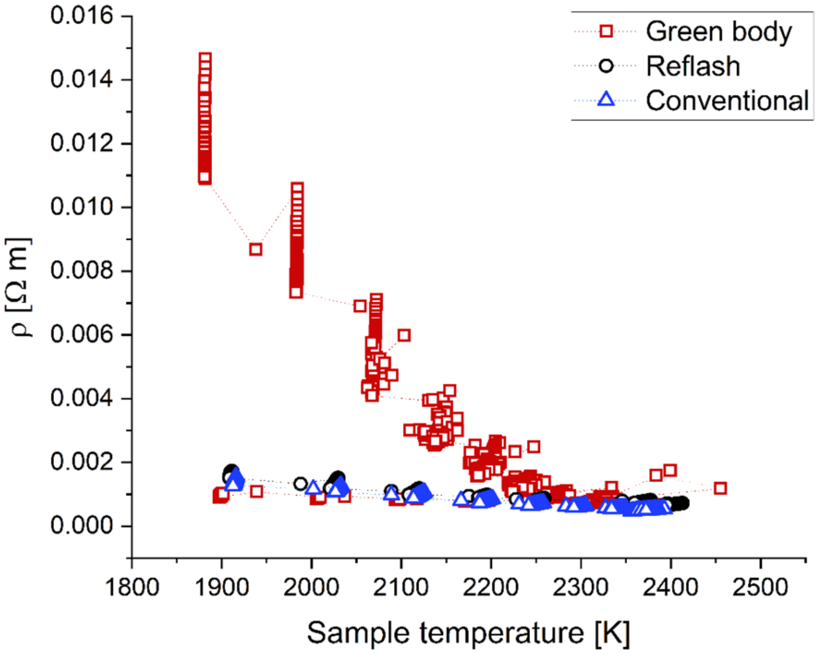

Figure 6.4: The electrical resistivities of a SiC green body during heating using the 400 W heating schedule (upper branch of results) and cooling at the same rate (lower branch), the same sample subjected to the same heating schedule again (reflash), and that of a conventionally pre-sintered sample, subjected to the same heating schedule with pristine electrodes.

Figure 6.4 compares the results of Fig. 6.3b, those of the resistivity of a green body during a flash sintering stepped heating experiment, with the results of the same specimen heated for a second time using the same combination of furnace and electrical heating, and a dense, conventionally sintered specimen, again subjected to the same heating cycle. The greenbody specimen was fitted with new electrodes, while the electrodes attached to the reflashed specimen remained unchanged between this and the former experiment. The conventionally sintered sample had new electrodes. All samples except the green body during heating for the first time follow the same line regardless of whether the electrodes were new or old or whether the pre-sintering was by "flash" or conventional heating.

6.1.3 Microstructure along the length of a flash sintered specimen

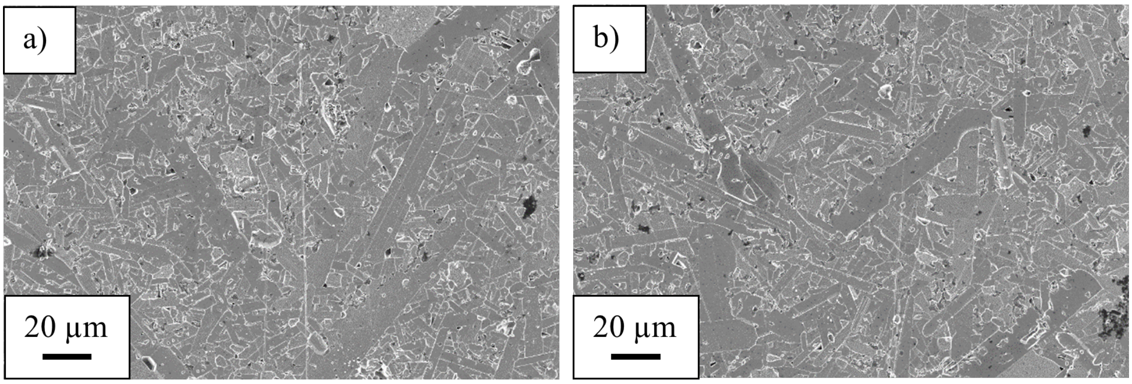

Figure 6.5: SEM images of a 550 W flash sintered sample, taken of the centre of the sample, along its length a), and of its cross section, b).

Figure 6.5a shows SEM images of the central region of a sample that was polished along its length and 6.5b shows the central region of a polished cross section of a separate sample that was flash sintered using the same heating schedule. Both images show randomly orientated, bimodal grain structures; average grain sizes were within experimental uncertainty of one another (5.6 µm ± 0.5 µm in Fig. 6.5a, and 5.8 µm ± 0.5 µm in Fig. 6.5b).

6.2 Discussion

6.2.1 Phenomenology of the electrical response: the flash event at constant voltage

The electrical response of SiC leading up to the flash event at constant voltage as shown in Figs. 6.1 and 6.2 was qualitatively similar to that of a wide variety of other ceramics[166]: a rapid drop in sample resistance occurred with a consequent increase in current and electrical power dissipation. The reduction of the critical furnace temperature required for the flash event in SiC with increasing electric field (Fig. 6.2) is also typical behaviour.

The electrical and thermal response of several oxides[100,101,104,114,167] during the flash event shows that it is caused by thermal runaway, in which the reduction of resistance as the sample temperature increases leads to a greater increase in power dissipation at constant voltage than can be lost from the sample surface as heat. The consequence is rapid electrical heating of the sample. The combination of electric field E and furnace temperature T_f at which runaway will occur is given by[100,116]:

$$E^2 = \frac{4p\epsilon\sigma\rho_0 R}{AQ(T_f + \Delta T_c)^5} exp(\frac{Q}{R(T_f + \Delta T_c)}) \tag{6.1}$$

in which for $\Delta T_c \ll T_f$:

$$\Delta T_c \approx \frac{RT_f^2}{(Q - 5RT_f)} \tag{6.2}$$

In these equations, p and A are the perimeter and area of the specimen cross-section between the electrodes, ϵ the emissivity, σ Stefan's constant, ρ_0 the pre-exponential in the inverse Arrhenius expression for the resistivity as a function of temperature, R the gas constant, Q the activation energy for electrical resistivity/conductivity, and ΔT_c the excess temperature of the specimen relative to the furnace (i.e. $T_s - T_f$) at runaway. The equations can be used to predict the critical electric field for runaway at constant furnace temperature or the critical furnace temperature at which the flash event occurs during heating with a constant electric field.

The values of Q and ρ_0 for the 15 V cm^{-1}, 35 V cm^{-1} and the 40 V cm^{-1} could not be accurately extracted from the results of Fig. 6.2. The 15 V cm^{-1} test did not exhibit runaway, and the electric field strengths of the 35 V cm^{-1} and the 40 V cm^{-1} tests caused runaway to occur immediately upon application of the electric field, indicating that the furnace temperature was already higher than the critical temperature. Hence, a precise critical furnace temperature could not be experimentally determined for these tests.

For each of the three samples in Fig. 6.2 that did exhibit flash events, the values of Q and ρ_0 were deduced from the inverse Arrhenius plots for resistivity in Fig. 6.6a. The plots for all three specimens possess two approximately straight sections with a distinctive undulation in between. The flash event occurred at higher temperatures than the undulation so the values of Q and ρ_0 for each specimen were extracted using the straight sections immediately to the left of the undulations in Fig. 6.6a and are given in Table 6.2. The transition in behaviour will be discussed in the next section.

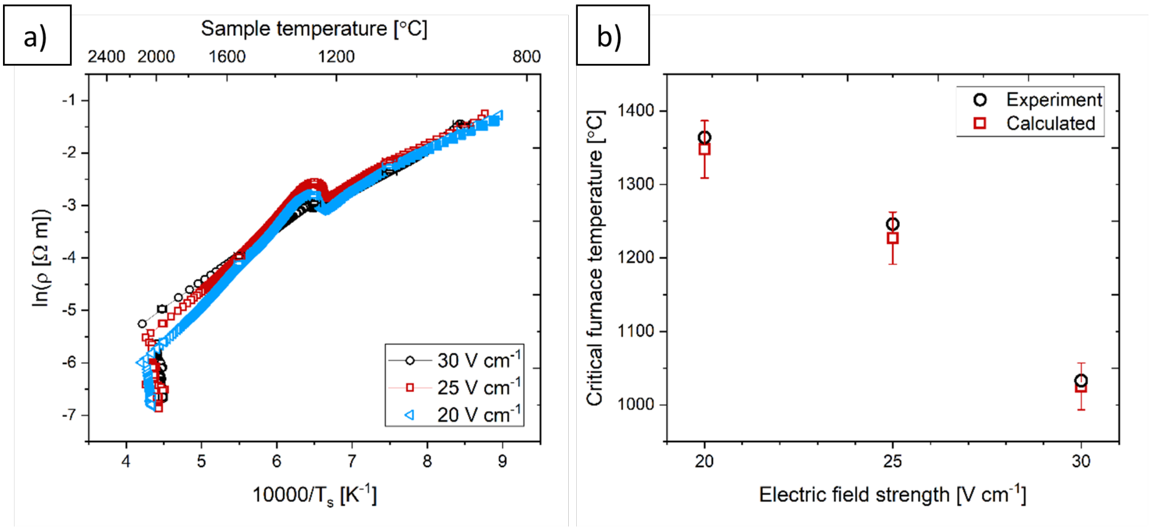

Figure 6.6: a) Data from the 30 V cm^{-1}, 25 V cm^{-1} and 20 cm^{-1} constant initial electric field tests plotted as $\ln(\rho)$ vs T_S^{-1}, where T_s is the specimen temperature and ρ the resistivity. For clarity, error bars are only shown for representative data points. b) The predicted and observed critical furnace temperature against electric field strength.

Electric field strength (V cm^{-1})	Q (kJ mol^{-1})	ρ_0 (Ω m)
20	137	1.91 x 10^{-6}
25	127	3.94 x 10^{-6}
30	92	3.74 x 10^{-5}

Table 6.2: Activation energies and pre-exponentials of resistivity for the data of Figs. 6.2 and 6.6a in the vicinity of the flash event.

Figure 6.6b compares the experimentally observed furnace temperatures at run-away for each initial electric field E with those predicted by solving Eqns. 6.1 and 6.2 for T_f using the values of Q and ρ_0 in Table 6.2 with $\epsilon = 0.85$[137] and the measured values for p and A. The agreement is within experimental uncertainty, demonstrating that the thermal and electrical characteristics of the “flash event” observed here in

SiC was consistent with thermal runaway, as in oxide ceramics.

6.2.2 Mechanisms influencing electric conductivity during flash sintering of SiC

The flash event at constant electric field analysed in the previous section originated in the NTC behaviour during heating evident in Figs. 6.3b and 6.6b. Most ceramic powder compacts exhibit NTC behaviour under the flash sintering conditions[111]. This can result from (i) the innate NTC behaviour of many ceramics caused by an increasing concentration or mobility of the charge carriers with temperature; (ii) extrinsic effects of the increase in current with temperature at constant voltage, such as the increasing component of electronic conductivity observed in YSZ under direct current as it becomes electrochemically reduced near the cathode[168]; and iii) the effect of the early stages of sintering in improving particle-particle contacts[116]. Electrochemical reduction is not expected to occur in an electronically conducting, covalently bonded semiconductor such as SiC, and the symmetrical appearance of the specimens during flash sintering suggests that any other effects of the direct current on resistivity were limited. As shown in Fig. 6.3b, the resistivity of the sintered specimen was also almost constant during cooling between 2200 °C and 1500 °C, so the underlying NTC behaviour of the SiC itself is evidently also weak under these conditions. This temperature-independence of resistivity above 800 °C has also been reported for a range of α-SiC ceramics by Gnesin et al.[63]. The same authors also showed that SiC heating elements had a resistivity that ranged between 10^{-1} and 10^{-2} Ohm·m at 1500

°C, depending on doping levels. Flash sintered SiC in this work had a resistivity of ∼2x10^{-2} Ohm·m at 1500 °C, Kim et al. show that the resistivity of polycrystalline SiC at room temperature can range from $10^{-}3$ and $10^{1}1$ Ohm·m[61]. Given this very wide range in the possible resistivities of SiC, the slight difference between the resistivity of SiC in this work and that observed by Gnesin is likely explained by differences in doping levels between the materials. Racette measured the resistivity of n-type SiC up to 2000 °C and found its conductivity to be ∼5 S $cm^{-}1$ at this temperature. The conductivity of SiC in this work at a similar temperature was ∼6.5 S $cm^{-}1$ (Fig. 6.3b). As such, the resistivity of SiC in this work is broadly consistent with that observed in the literature

It is also apparent from Fig. 6.4 that any chemical effect at the electrode/SiC intersection that might improve electrical contact could not have been responsible for the fall in resistivity during heating in Fig. 6.3b. This also shows that flash sintering did not alter/degrade the electrical resistivity of SiC significantly.

Instead, it is suggested that this drop in resistivity must therefore have been predominantly caused by mechanisms associated with the sintering of the powder compact. This is demonstrated by the large difference in resistivity at $T_s \sim$ 1600 °C in the heating and cooling parts of the cycle, and by the continuously decreasing resistivity at approximately constant specimen temperature during the constant power periods of the stepped profile used in the heating portion of the cycle, where the specimen temperature would have been constant. The difference in resistivity before and after sintering in Fig. 6.3b corresponds to a factor of ∼18. This is of the same order as the resistivity change measured before and after the flash sintering 3YSZ[116] and is considered to be primarily the consequence of the improvement in the quality and area of connection between grains as sintering progresses. This conclusion was also reached after investigation into thermal runaway-driven flash events in WC and AA5083 aluminium alloy. Both of these materials exhibit PTC electrical behaviour but their powder compacts initially exhibit NTC behaviour on the application of an electric field owing to the removal of oxides or other resistive contaminants from between the particles and the increase in contact area between the particles[17,169,170].

Additionally, a contribution to the change in conductivity during sintering from the diffusion of the B sintering aid - an acceptor dopant - into the grains during sintering cannot be completely ruled out. Due to the N_2 doping from the atmosphere during the Acheson process[171] it is expected that the powder used in this work was an n-type semiconductor. The B could be expected to counteract this[70,172] and initially increase the resistivity. However, the relevant diffusion coefficients[173] suggest that the B could only have diffused to the centre of the grains once the highest temperatures had been reached. Furthermore, even when holes become the dominant charge carriers, B additions are associated with an increase in the high temperature resistivity[63,174]. Given the strong reduction of resistivity during sintering shown in Fig. 6.3b, it is concluded that any such effect of B is outweighed by the resistivity reduction caused by sintering.

The variation of the values of activation energy Q in Table 6.2 is a consequence of indirect factors such as geometry, chemistry, and thermal history; factors that have no reason to obey an Arrhenius relationship. These are apparent activation energies, not indicative of a particular transport mechanism and there is therefore no reason for them to be constant. The straightness of the lines in Fig. 6.6a to the left of the undulations is therefore coincidental.

The undulations in Fig. 6.3a correspond to the transient peaks in power seen before the corresponding flash events in Fig. 6.2. These are suggested to be a consequence of the C sintering additives removing the layer of SiO_2 present on the surface of the SiC powder particles. Estimated sample temperatures during this period were similar for all electric fields, at 1200 °C - 1300 °C. The carbothermal[173] reduction of SiO_2 by C has been shown to take place in this temperature range[154,175]. It is suggested that the removal of the electrically insulating SiO_2 on the surfaces of the SiC grains initially increased the conductivity of the specimen. Eventually, the conductive free C was used up by the reaction with the SiO_2 and the specimen conductivity fell again, producing the peaks in Fig. 6.2. It is evident from Fig. 6.3a that the apparent activation energies are different before and after the undulation in each case, which is consistent with the proposed change in the chemistry of the conductive path through the specimen.

6.2.3 The role of the current and electric field during flash sintering

As discussed above and in Chapters 4 and 5, it is suggested that the current predominantly acts as a heat source during the flash sintering of SiC. The similarity between the microstructures of randomly orientated grains in Figs. 6.5a and 6.5b shows no sign of grain orientation along the direction in which the current flowed: the current has not had an anisotropic effect on the microstructure of SiC.

As discussed in section 2.4.2.2, there are authors that suggest that the electric field applied over samples during flash sintering increases the densification rate over that observed during conventional, pressureless sintering[18,136]. They argue that the field is necessary to initiate an avalanche of point defects in the crystal structure. Todd et al. show that the rapid densification of 3YSZ observed in flash sintering is equally possible using heating techniques that do not apply an electric field over the sample during sintering[100]. Figure 4.35 shows that despite similar times spent at sintering temperatures, conventional heating (fire 2) of SiC produced a denser material than that produced through flash sintering (550 W schedule). Additionally, Stobierski and Gubernat were able to sinter SiC green bodies with similar composition to those in this work to 92% dense in ∼40 s at 2150 °C[41]. With the same nominal temperature, it took ∼240 s for the flash sintered specimen in this work to reach a similar density. These observations demonstrate that the electric field does not play a dominant role in the densification rate during flash sintering. Additionally, evidence from each chapter in this thesis, such as the similarities between the microstructures, electrical resistivity of dense samples and the mechanical properties between most flash and conventionally sintered SiC specimens, strongly suggests that the current need only be regarded as a heat source and there is no need to account for any additional effects introduced by it.

6.2.4 Conclusions

The flash event in a non-oxide ceramic was shown to be phenomenologically similar to that found in oxide ceramics. It is characterised by a rapid rise in sample temperature followed by densification and accompanied by a decrease in sample resistivity, occurring under constant voltage conditions. This behaviour was shown to be consistent with thermal runaway, driven by the NTC characteristic of the resistivity during heating. A thermal runaway model accurately predicted the conditions for the flash event in SiC. In contrast to oxide ceramics, however, the underlying electrical resistivity of the SiC had a weak temperature dependence in the temperature range of interest. The origin of the NTC behaviour and the thermal runaway was found to be the early stages of sintering, in which improved connectivity between the powder particles led to a reduction in resistivity. No evidence of grain orientation along the axis of current flow was observed in the microstructure of flash sintered SiC. Throughout the investigation of this thesis, the current has had no discernible effect on SiC other than that of a heat source.

Chapter 7

Conclusions

7.1 Densification and microstructure

An experimental apparatus was developed that allowed BC-SiC bar shaped specimens to be flash sintered to 96% density in 16 min in an alumina tube furnace at 1500 °C. Compared with samples of similar density that were conventionally sintered using the powder's recommended sintering schedule, the production time of the flash sintered samples was reduced by more than 6 h and with a furnace temperature lower by 700 °C. An optimised flash sintering methodology was found from systematically testing the effect that the following flash sintering parameters had on sample microstructure: power limit, power ramp rate, furnace temperature, hold time, sintering atmosphere (gas type and C additions in the furnace tube), thermal insulations and sample thickness. Higher power limits, higher furnace temperatures, slower power ramp rates, and longer hold times all increased sample density and the average grain size of specimens. For constant specific power, increasing the thickness of samples decreased their density and average grain size. Two of the investigated sintering atmospheres were found to affect sample microstructure and density. RGAr and He atmospheres were shown to be similarly inert. Nitrogen reduced density and stabilised the 3C polytype; the cubic phase resulted in elongated grains that restricted densification. An atmosphere of Ar $+5\%$ H_2 reduced density and retarded the grain growth of the sample. The drop in density was caused by the active oxidation on the surface of the sample, but the cause of the limited grain growth requires further investigation. In all samples, larger grains were associated with an increase in the 4H SiC polytype concentration in that sample.

Carbon additions in the furnace were shown to have a significant impact on the densification and microstructure of SiC. Increasing the amount of C in the furnace tube during sintering decreased the average grain size and increased the density of the sample. It was suggested that these additions resulted in precipitation of graphite on the sample's surface and lowered partial oxygen pressures, which indirectly reduced the amount of C lost from the sample during heating. More C in the sample then reduced the amount of liquid phase during sintering and hence retarded grain growth.

None of the tested insulations (C foil or felt wrapped around the specimen and mirrors placed around the sample) increased sample density and all resulted in abnormal grain growth in these specimens. It was hypothesised that the increase in sample temperature caused by the insulations created more liquid phase during sintering, which led to the observed abnormal grain growth in these samples. The low densities of these specimens were suggested to be a consequence of the overly reducing atmosphere and the resultant active oxidation of the SiC that was caused by the proximity of the C insulations to the sample.

Out of the tested parameters, an optimum flash sintering profile for bar shaped specimens with typical dimensions 22 mm × 6 mm × 2 mm was identified as: a heating schedule with a maximum power of 550 W, at furnace temperature of 1500°C, and in a He sintering atmosphere with C discs and foil placed within the furnace. This produced samples with a small average grain size and high density.

It was shown that flash sintering did not cause faster densification than that achieved through conventional heating. Additionally, there was no microstructural evidence to suggest that novel sintering mechanisms arose due to the application of an electric field during sintering. Densification was achieved through liquid phase sintering, which was expected of B,C sintering aids from the literature. This part of the research has shown that high density SiC bars can be produced through flash sintering (up to 96% relative density). However, scaling the process up to create disc shaped specimens remains challenging and no density greater than 65% was achieved in this work for such specimens. A power supply able to supply greater currents than those accessible in this work is required to dissipate the heat necessary to flash sinter large SiC samples to high densities.

7.2 Mechanical properties of flash sintered SiC

The Vickers hardness of most of the SiC samples in this work was shown to be dependent on density and average grain size up to ∼90% bulk sample density and ∼4 µm, respectively. However, for low densities, it was assumed that density is the dominant influence on hardness. Samples that reached 90% bulk density typically had a hardness of ∼24 GPa. SEM images showed that the centres of these samples were almost entirely dense. After this density threshold of 90%, the dependency of hardness on it diminished. Atmospheric conditions were shown to affect the hardness of SiC; the inclusion of C additions in the furnace tube during sintering significantly increased the Vickers hardness of SiC above those achieved through conventional sintering of the same powder (in this work and in the literature). The highest hardness achieved of all tests was 27.8 GPa ± 0.4 GPa of the sample produced using a mirror set up that placed polished mirrors around the sample that were balanced on alumina discs. The underlying mechanism that led to this super-hard SiC was shown to be independent of density, grain size and polytype concentration but is suggested to be related to a C concentration threshold in the sintering atmosphere. APT analysis indicated that the super-hard SiC samples had a greater concentration of B rich clusters than SiC of regular hardness, which are suggested to cause dispersion hardening in these samples.

A comparative study of specimens sintered using slow and fast conventional heating schedules (fire 1, fire 2, respectively) and the optimised flash sintering heating schedule indicated that the 3-point flexural strength and fracture toughness of SiC were largely independent from the tested heating schedules. It is concluded that flash sintering did not degrade the strength or the toughness of SiC. Due to its higher Vickers hardness and similar strength and toughness values, if flash sintered SiC was successfully scaled up, the material may outperform traditional SiC armour plates in ballistic trials. However, properties of the former, such as the elastic modulus, still requires investigation and due to intrinsic material characteristics, such as its density, flash sintered SiC may not be the optimum choice of ceramic ballistic plate in all scenarios.

7.3 Electrical properties of SiC during flash sintering

The flash event in a non-oxide ceramic under constant voltage conditions was shown to be phenomenologically similar to that found in oxide ceramics. It is characterised by a rapid rise in sample temperature followed by densification and accompanied by a decrease in sample resistivity. This behaviour was shown to be consistent with thermal runaway, driven by the NTC characteristic of the resistivity during heating. A thermal runaway model accurately predicted the conditions for the flash event in SiC. In contrast to most oxide ceramics, however, the underlying electrical resistivity of the SiC had a weak temperature dependence in the temperature range of interest. The origin of the NTC behaviour and the thermal runaway was found to be the early stages of sintering, in which improved connectivity between the powder particles led to a reduction in resistivity.

No evidence of grain orientation along the axis of current flow was observed in the microstructure of flash sintered SiC. Throughout the investigation of this thesis, the current has had no discernible effect on SiC other than that of a heat source.

Chapter 8

Future work

These investigations have created further research opportunities in the following areas:

- Regarding flash sintering's utility as a manufacturing technique, the process will need to demonstrate that it can produce larger samples than the bar shaped specimens made in this work. The next step would be sourcing a power supply capable of supplying a higher current than that used in this investigation; high voltages (>100 V) would not be required. Larger samples would then allow direct comparison of ballistic performance between conventional SiC armour and the super-hard SiC produced in this work.

- Further investigation is needed into whether the reducing atmosphere created by the Ar + 5% H_2 gas can produce similar effects on sample microstructure and Vickers hardness to C in the sintering atmosphere. Investigate an Ar + H gas with smaller proportions of hydrogen.

- If flash sintering SiC from room temperature is to be investigated, electrical heating will be applied to the sample at a furnace temperature lower than the temperature at which carbothermal reduction of SiO_2 takes place (1200 °C

- 1300 °C). Samples in this instance may contain sufficient O to affect the sintering mechanisms and additional free C in the powder might be required to mitigate this. How the O content and the rapid heating of flash sintering affects the sintering mechanisms of SiC might be investigated by flash sintering SiC powders of varying O purities."

- APT has indicated that there was a greater concentration of B clusters in super-hard SiC than conventionally sintered SiC, but work is required to understand how a C rich atmosphere might have led to this. APT analysis on samples of normal and super-hard SiC that were produced using the same 550 W heating schedule might provide insight. It may be interesting to test whether there is a difference in B concentration at grain boundaries, or a greater degree of clustering in SiC sintered with different C atmospheres. Future work might also use APT to investigate SiC samples flash sintered to different densities, and samples flash sintered for longer. These results may show the evolution of the B cluster formation during flash sintering, potentially showing a greater number of the clusters in the newly formed grain volume, compared to the B content in the central part of the original grains. Additionally, it should be investigated whether a reducing atmosphere (Ar + H_2) could create samples that exhibit a similar increase in hardness to those made with a carbon rich atmosphere. If this is the case, using different mixes of a reducing gas might allow a more robust measurement and characterisation of how the atmosphere affects the viscosity of the B liquid phase during sintering."

- To show that sintering did initiate the flash event, it would be useful to image the samples using SEM just before runaway occurs, to see whether necking had started between SiC particles.

- The junction between SiC and the tungsten electrodes will likely form a Schottky barrier[110] and cause the Peltier effect[176] and asymmetrical heating of the sample near the electrodes. There was no visible difference in camera recordings, but SEM investigation near the electrodes would show any localised effects.

- Hallam et al. showed that there was no correlation between Vickers hardness and ballistic performance, but that there was for Knoop hardness[6]. It may be prudent to characterise the hardness of flash sintered SiC using the Knoop indentation technique.

- TEM analysis near the Vickers indents might allow for direct imaging of dislocation bowing around nanoparticles, which would provide substantive evidence that the clusters were the cause of the super-hard SiC.

- According to Stobierski and Gubernat, more B creates more liquid phase during the sintering of SiC, which can lead to abnormal grain growth[41]. However, if C in the atmosphere solidifies the phase or C can affect the solubility of B in SiC, it may be possible to increase the amount of B clusters or size of the B clusters above those found in the super hard SiC in this work and lead to an even harder material.

- Although the low densities of the SiC disc shaped specimens would not be appropriate for armour applications, porous SiC does have uses in high temperature filtration systems. It may be possible to use flash sintering to create low cost and low density materials for this purpose.

Appendix A

Supplementary information

Powder characteristic	Value
SiC polytypes	Alpha
Specific surface area	15 m^2 kg^{-1}
d50	115 nm
Morphology	Spray dried granules (~60 μm)
Impurities	
O	5.00wt.% max.
Fe	0.05wt.% max.
Al	0.04wt.% max.
Ca	0.01wt.% max.
Sintering aids	
B	0.45wt.% max.
C	3.25wt.% max.
Binder	PEG + PVA
Green density	1.80 – 1.90 g cm^{-3}
Sintered density	3.13 – 3.18 g cm^{-3}

Table A.1: Properties of the SiC premix powder.

Investigation	Sample name	Ramp rate	Hold period	Furnace additions
Power limit	300 W	100 W min^{-1} to 300 W No ramp down	5 min at 300 W	None
	350 W	100 W min^{-1} to 350 W No ramp down	5 min at 350 W	None
	400 W	100 W min^{-1} to 400 W No ramp down	5 min at 400 W	None
	450 W	100 W min^{-1} to 400 W No ramp down	5 min at 400 W 5 min at 450 W	None
	500 W	100 W min^{-1} to 400 W No ramp down	5 min at 400 W 5 min at 450 W 5 min at 550 W	None
	550 W	100 W min^{-1} to 400 W No ramp down	5 min at 400 W 5 min at 450 W 5 min at 500 W 1 min at 550 W	None
Ramp rate	100 W min^{-1}	100 W min^{-1} to 400 W 100 W min^{-1} ramp down	5 min at 400 W	None
	50 W min^{-1}	100 W min^{-1} to 400 W No ramp down	5 min at 400 W	None
	No ramp	No ramp to 400 W No ramp down	5 min at 400 W	None
	No ramp LH	No ramp to 400 W No ramp down	12 min at 400 W	None
Hold time	0.5 min	100 W min^{-1} to 400 W No ramp down	0.5 min at 400 W	None
	5 min	100 W min^{-1} to 400 W No ramp down	5 min at 400 W	None
	15 min	100 W min^{-1} to 400 W No ramp down	15 min at 400 W	None
	30 min	100 W min^{-1} to 400 W No ramp down	30 min at 400 W	None
Furnace temperature	1200 °C	~100 W min^{-1} to 460 W No ramp down	5 min at 460 W	None
	1350 °C	~100 W min^{-1} to 430 W No ramp down	5 min at 430 W	None
	1500 °C	~100 W min^{-1} to 400 W No ramp down	5 min at 400 W	None
Sample thickness	Thickness x1.0	100 W min^{-1} to 400 W 100 W min^{-1} to 0 W	5 min at 400 W	None
	Thickness x1.5	~100 W min^{-1} to 460 W ~100 W min^{-1} to 0 W	5 min at ~460 W	None
	Thickness x2.0	~100 W min^{-1} to 510 W ~100 W min^{-1} to 0 W	5 min at ~510 W	None

Table A.2: Matrix of flash sintering parameters.

Investigation	Sample name	Ramp rate	Hold period	Furnace additions
Insulation	Mirrors (Mirrors 2)	100 W min^{-1} to 400 W No ramp down	5 min at 400 W 5 min at 450 W 5 min at 500 W 1 min at 550 W	C discs mirrors
	C felt	100 W min^{-1} to 400 W No ramp down	5 min at 400 W 5 min at 450 W 5 min at 500 W 1 min at 550 W	C felt wrap
	C foil	100 W min^{-1} to 400 W No ramp down	5 min at 400 W 5 min at 450 W 5 min at 500 W 1 min at 550 W	C foil cylinder
Mirror constituent tests	Mirrors 1	100 W min^{-1} to 400 W No ramp down	5 min at 400 W 5 min at 450 W 5 min at 500 W 1 min at 550 W	C foil Al_2O_3 discs mirrors
	Mirrors 2	100 W min^{-1} to 400 W No ramp down	5 min at 400 W 5 min at 450 W 5 min at 500 W 1 min at 550 W	C discs mirrors
	Mirrors 3	100 W min^{-1} to 400 W No ramp down	5 min at 400 W 5 min at 450 W 5 min at 500 W 1 min at 550 W	C foil C discs mirrors
Carbon additions	400 W C foil	100 W min^{-1} to 400 W No ramp down	5 min at 400 W	C foil
	400 W C discs	100 W min^{-1} to 400 W No ramp down	5 min at 400 W	C discs
	550 W C foil	100 W min^{-1} to 400 W No ramp down	5 min at 400 W 5 min at 450 W 5 min at 500 W 1 min at 550 W	C foil
	550 W C discs	100 W min^{-1} to 400 W No ramp down	5 min at 400 W 5 min at 450 W 5 min at 500 W 1 min at 550 W	C discs mirrors
	550 W C discs + C foil	100 W min^{-1} to 400 W No ramp down	5 min at 400 W 5 min at 450 W 5 min at 500 W 1 min at 550 W	C foil C discs
	550 W C discs + C foil + mirrors	100 W min^{-1} to 400 W No ramp down	5 min at 400 W 5 min at 450 W 5 min at 500 W 1 min at 550 W	C foil C discs mirrors

Table A.3: Matrix of flash sintering parameters continued.

Investigation	Sample name	Ramp rate	Hold period	Furnace additions
Gas type	He	100 W min^{-1} to 400 W No ramp down	0.5 min at 400 W	None
	N_2	100 W min^{-1} to 400 W No ramp down	5 min at 400 W	None
	Ar + H_2	100 W min^{-1} to 400 W No ramp down	15 min at 400 W	None
Conventional sintering	Fire 1	5 min h^{-1} to 2150 °C 5 min h^{-1} to RT	2 h at 2150 °C	None
	Fire 2	16 min h^{-1} to 2150 °C 16 min h^{-1} to RT	5 min at 2150 °C	None

Table A.4: Matrix of flash sintering parameters continued.

Analysis	Temperature (K)	Pulse frequency (Hz)	Detection rate (%)	Laser energy (pJ)
Laser energy	50	200	0.5	30, 40, 50, 100
Laser vs Voltage	50	200	0.5	30
Reflection	50	200	0.5	30
Tip blunting	50	200	0.5	30
Laser proximity	50	200	0.5	30
Sample size	50	200	0.5	30

Table A.5: APT operating conditions for SiC analyses.

References

[1] P B Vandiver et al. "The Origins of Ceramic Technology at Dolni Věstonice, Czechoslovakia". In: *Science* 246.4933 (Nov. 1989), pp. 1002–1008. DOI: `10.1126/science.246.4933.1002`. URL: `https://doi.org/10.1126/science.246.4933.1002`.

[2] T Ma, P Chen, and J Zhao. "Overview on vertical and directional drilling technologies for the exploration and exploitation of deep petroleum resources". In: *Geomechanics and Geophysics for Geo-Energy and Geo-Resources* 2.4 (2016), pp. 365–395. ISSN: 2363-8427. DOI: `10.1007/s40948-016-0038-y`. URL: `https://doi.org/10.1007/s40948-016-0038-y`.

[3] J G Stone et al. "Stress analysis and probabilistic assessment of multi-layer SiC-based accident tolerant nuclear fuel cladding". In: *Journal of Nuclear Materials* 466 (2015), pp. 682–697. ISSN: 0022-3115. DOI: `https://doi.org/10.1016/j.jnucmat.2015.08.001`. URL: `https://www.sciencedirect.com/science/article/pii/S0022311515301410`.

[4] S Biamino et al. "Multilayer SiC for thermal protection system of space vehicles: Manufacturing and testing under simulated re-entry conditions". In: *Journal of the European Ceramic Society* 28.14 (2008), pp. 2791–2800. ISSN: 0955-2219. DOI: `https://doi.org/10.1016/j.jeurceramsoc.2008.04.006`. URL: `https://www.sciencedirect.com/science/article/pii/S0955221908001945`.

[5] CYKC Xia, C Y Kwok, and L F Nazar. "A high-energy-density lithium-oxygen battery based on a reversible four-electron conversion to lithium oxide". In: *Science* 361.6404 (2018), pp. 777–781. ISSN: 0036-8075. URL: `https://pubmed.ncbi.nlm.nih.gov/30139868/`.

[6] D Hallam et al. "The correlation of indentation behaviour with ballistic performance for spark plasma sintered armour ceramics". In: *Journal of the European Ceramic Society* 35.8 (2015), pp. 2243–2252. ISSN: 1873619X. DOI: `10.1016/j.jeurceramsoc.2014.11.035`.

[7] S Ji, Z Zhang, and F Wang. "Overview of high voltage sic power semiconductor devices: development and application". In: *CES Transactions on Electrical Machines and Systems* 1.3 (2017), pp. 254–264. ISSN: 2096-3564 VO - 1. DOI: `10.23919/TEMS.2017.8086104`.

[8] I Kiyoshi. *Electric-discharge sintering.* Mar. 1966. URL: `https://patentimages.storage.googleapis.com/0a/68/bb/162df6a9b6b160/US3241956.pdf`.

[9] S Grasso, Y Sakka, and G Maizza. "Electric Current Activated/Assisted Sintering (ECAS): a Review of Patents 1906–2008". In: *Science and Technology of Advanced Materials - SCI TECHNOL ADV MATER* 10.053001 (Oct. 2009). DOI: `10.1088/1468-6996/10/5/053001`.

[10] Baraldi and MECS-Machinery Economics Studies by ACIMAC. "World production and consumption of ceramic tiles". In: *Oceania* 56 (2016), pp. 0–4. URL: `https://zdocs.pub/doc/042049-statistic-prod-cons-mondiale-o1nzyx08e71l`.

[11] M Cologna, B Rashkova, and R Raj. "Flash sintering of nanograin zirconia in <5 s at 850°C". In: *Journal of the American Ceramic Society* 93.11 (2010), pp. 3556–3559. ISSN: 00027820. DOI: `10.1111/j.1551-2916.2010.04089.x`.

[12] M Cologna, J S C Francis, and R Raj. "Field assisted and flash sintering of alumina and its relationship to conductivity and MgO-doping". In: *Journal of the European Ceramic Society* 31.15 (2011), pp. 2827–2837. ISSN: 09552219. DOI: `10.1016/j.jeurceramsoc.2011.07.004`.

[13] A Karakuscu et al. "Defect structure of flash-sintered strontium titanate". In: *Journal of the American Ceramic Society.* Vol. 95. 8. 2012, pp. 2531–2536. DOI: `10.1111/j.1551-2916.2012.05240.x`.

[14] A L G Prette et al. "Flash-sintering of Co2MnO4 spinel for solid oxide fuel cell applications". In: *Journal of Power Sources* 196.4 (2011), pp. 2061–2065. ISSN: 03787753. DOI: `10.1016/j.jpowsour.2010.10.036`.

[15] R. Muccillo, E. N.S. Muccillo, and M. Kleitz. "Densification and enhancement of the grain boundary conductivity of gadolinium-doped barium cerate by ultra fast flash grain welding". In: *Journal of the European Ceramic Society* 32.10 (2012), pp. 2311–2316. ISSN: 09552219. DOI: `10.1016/j.jeurceramsoc.2012.01.032`.

[16] E. Zapata-Solvas et al. "Preliminary investigation of flash sintering of SiC". In: *Journal of the European Ceramic Society* 33.13-14 (2013), pp. 2811–2816. ISSN: 09552219. DOI: `10.1016/j.jeurceramsoc.2013.04.023`.

[17] I Mazo, A Molinari, and V M Sglavo. "Effect of pressure on the electrical resistance flash sintering of tungsten carbide". In: *Journal of the European Ceramic Society* 42.5 (2022). ISSN: 1873619X. DOI: `10.1016/j.jeurceramsoc.2022.01.017`.

[18] C Schmerbauch et al. "Flash sintering of nanocrystalline zinc oxide and its influence on microstructure and defect formation". In: *Journal of the American Ceramic Society* 97.6 (2014), pp. 1728–1735. ISSN: 15512916. DOI: `10.1111/jace.12972`.

[19] *Flash Sintering of Ceramics | Lucideon.* URL: `https://www.lucideon.com/healthcare/technologies/flash-sintering`.

[20] Edward G. Acheson. *Production of artifical crystalline garbonaceous materials.* 1893. URL: `https://patentimages.storage.googleapis.com/71/2f/b6/d18bfc04e2c958/US492767.pdf`.

[21] Hidehiko Tanaka. *Silicon carbide powder and sintered materials.* 2011. DOI: `10.2109/jcersj2.119.218`.

[22] C Barry Carter and M Grant Norton. *Ceramic materials: science and engineering.* Vol. 716. Springer, 2007. URL: `https://www.researchgate.net/publication/274719826_Physics_of_Advanced_Materials_Winter_School_2008_Determination_of_lattice_site_location_of_impurities_in_compound_semiconductors_by_transmission_electron_microscopy`.

[23] D Feng et al. "Occurrence forms of major impurity elements in silicon carbide". In: *Ceramics International* 48.1 (2022). ISSN: 02728842. DOI: `10.1016/j.ceramint.2021.09.095`.

[24] P T B Shaffer. "A review of the structure of silicon carbide". eng. In: *Acta Cryst. B* 25.3 (1969), pp. 477–488. ISSN: 0567-7408. DOI: `10.1107/S0567740869002457`.

[25] S Mitridis. "Physics of Advanced Materials Winter School 2008 Determination of lattice site location of impurities in compound semiconductors, by transmission electron microscopy". In: (Mar. 2011). URL: `https://www.researchgate.net/publication/274719826_Physics_of_Advanced_Materials_Winter_School_2008_Determination_of_lattice_site_location_of_impurities_in_compound_semiconductors_by_transmission_electron_microscopy`.

[26] W F Knippenberg. *Growth Phenomena in Silicon Carbide.* Philips research reports. N. V. Philips' Gloeilampenfabrieken, 1963. URL: `https://books.google.co.uk/books?id=jXYTAQAAIAAJ`.

[27] Y Inomata et al. *Polytypes of SiC crystals grown from molten silicon.* Tech. rep. 1970, pp. 83–88.

[28] G L Harris. *Properties of Silicon Carbide.* Institution of Engineering & Technology, 2000. ISBN: 9780863415548. URL: `https://books.google.co.uk/books?id=vPCOPwAACAAJ`.

[29] N. W. Jepps and T. F. Page. "Polytypic transformations in silicon carbide". In: *Progress In Crystal Growth And Characterization* 7.1-4 (1983), pp. 259–307. ISSN: 01463535. DOI: `10.1016/0146-3535(83)90034-5`.

[30] Akira Kondo and Hiroaki Kitahama. "Electrical properties of nitrogen-doped pressureless sintered SiC". In: *Journal of the Ceramic Society of Japan* 107.8 (1999), pp. 757–761. ISSN: 09145400. DOI: `10.2109/jcersj.107.757`.

[31] N. W. Jepps and T. F. Page. "The 6H→ 3C"Reverse" Transformation in Silicon Carbide Compacts". In: *Journal of the American Ceramic Society* 64.12 (1981), pp. C-177-C–178. ISSN: 15512916. DOI: `10.1111/j.1151-2916.1981.tb15906.x`.

[32] Yet-Ming Chiang, Dunbar P Birnie, and W David Kingery. *Physical Ceramics*. 1997. URL: `https://www.wiley.com/en-us/Physical+Ceramics%3A+Principles+for+Ceramic+Science+and+Engineering-p-9780471598732`.

[33] R Goodall, J.-F. Despois, and A Mortensen. "Sintering of NaCl powder: Mechanisms and first stage kinetics". In: *Journal of the European Ceramic Society* 26.16 (2006), pp. 3487–3497. ISSN: 0955-2219. DOI: `https://doi.org/10.1016/j.jeurceramsoc.2005.12.020`. URL: `https://www.sciencedirect.com/science/article/pii/S0955221906000276`.

[34] M F Ashby. "A first report on sintering diagrams". In: *Acta Metallurgica* 22.3 (1974), pp. 275–289. ISSN: 0001-6160. URL: `https://www.sciencedirect.com/science/article/abs/pii/0001616074901679?via%3Dihub`.

[35] S Prochazka. *The role of boron and carbon in the sintering of silicon carbide Chapter 16*. United Kingdom: British Ceramic Research Association, 1975. ISBN: 0900910240. URL: `http://inis.iaea.org/search/search.aspx?orig_q=RN:06204213`.

[36] Kun Sang Lee and Ji Ho Lee. "Mechanisms of Low-Salinity and Smart Waterflood". In: *Hybrid Enhanced Oil Recovery using Smart Waterflooding* (2019), pp. 27–37. DOI: `10.1016/B978-0-12-816776-2.00002-7`.

[37] C. Greskovich and J. H. Rosolowski. "Sintering of Covalent Solids". In: *Journal of the American Ceramic Society* 59.7-8 (1976), pp. 336–343. ISSN: 15512916. DOI: `10.1111/j.1151-2916.1976.tb10979.x`.

[38] Teizo HASE and Hiroshige SUZUKI. "Sinterability of Submicron β-SiC Prepared from Siliconization of Carbon Black". In: *Journal of the Ceramic Association, Japan* 86.1000 (1978). ISSN: 0009-0255. DOI: `10.2109/jcersj1950.86.1000{\_}606`.

[39] T Hase and H Suzuki. "Initial-stage Sintering of Beta-SiC with Concurrent Boron and Carbon Additions". In: *J. CERAM. SOC. JAP. J. Ceram. Soc. Jap.* 88.1017 (1980), p. 258.

[40] Giuseppe Magnani et al. "Pressureless sintered silicon carbide with enhanced mechanical properties obtained by the two-step sintering method". In: *Ceramics International* 40.1 PART B (2014), pp. 1759–1763. ISSN: 02728842. DOI: `10.1016/j.ceramint.2013.07.075`.

[41] Ludoslaw Stobierski and Agnieszka Gubernat. "Sintering of silicon carbide II. Effect of boron". In: *Ceramics International* 29.4 (2003), pp. 355–361. ISSN: 02728842. DOI: `10.1016/S0272-8842(02)00144-X`.

[42] Yinsheng Li et al. "High thermal conductivity in pressureless densified SiC ceramics with ultra-low contents of additives derived from novel boron-carbon sources". In: *Journal of the European Ceramic Society* 34.10 (2014), pp. 2591–2595. ISSN: 09552219. DOI: `10.1016/j.jeurceramsoc.2014.02.024`.

[43] K. Kaneko et al. "Determination of the chemical width of grain boundaries of boron- and carbon-doped hot-pressed β-SiC by HAADF imaging and ELNES line-profile". In: *Acta Materialia* 48.4 (2000), pp. 903–910. ISSN: 13596454. DOI: `10.1016/S1359-6454(99)00393-6`.

[44] Xiao Feng Zhang, Mark E. Sixta, and Lutgard C. De Jonghe. "Secondary Phases in Hot-Pressed Aluminum-Boron-Carbon-Silicon Carbide". In: *Journal of the American Ceramic Society* 84.4 (2001), pp. 813–820. ISSN: 00027820. DOI: `10.1111/j.1151-2916.2001.tb00746.x`.

[45] Peter T.B. Shaffer. "The SiC phase in the system SiC-B4C-C". In: *Materials Research Bulletin* 4.3 (1969), pp. 213–219. ISSN: 00255408. DOI: `10.1016/0025-5408(69)90058-0`.

[46] Mohammad Asadikiya et al. "The Role of Calphad Approach in the Sintering of B4C with SIC as a Sintering Aid by Spark Plasma Sintering Technique". In: *Additive Manufacturing and Strategic Technologies in Advanced Ceramics*. Vol. 258. 2016. DOI: `10.1002/9781119236016.ch19`.

[47] Svante Prochazka. "Sintering of Silicon Carbide BT - Mass Transport Phenomena in Ceramics". In: ed. by A R Cooper and A H Heuer. Boston, MA: Springer US, 1975, pp. 421–431. ISBN: 978-1-4684-3150-6. DOI: `10.1007/978-1-4684-3150-6{\_}28`. URL: `https://doi.org/10.1007/978-1-4684-3150-6_28`.

[48] L Stobierski and A Gubernat. "Sintering of silicon carbide I. Effect of carbon". In: *Ceramics International* 29.3 (2003), pp. 287–292. ISSN: 02728842. DOI: `10.1016/S0272-8842(02)00117-7`.

[49] F F Lange. "Hot-pressing behaviour of silicon carbide powders with additions of aluminium oxide". In: *Journal of Materials Science* 10.2 (1975), pp. 314–320. ISSN: 1573-4803. DOI: `10.1007/BF00540356`. URL: `https://doi.org/10.1007/BF00540356`.

[50] A Noviyanto and D H Yoon. "Metal oxide additives for the sintering of silicon carbide: Reactivity and densification". In: *Current Applied Physics* 13.1 (2013), pp. 287–292. ISSN: 15671739. DOI: `10.1016/j.cap.2012.07.027`.

[51] Jon Binner and Tammana S.R.C. Murthy. "Structural and Thermostructural Ceramics". In: *Encyclopedia of Materials: Technical Ceramics and Glasses* 2-3 (Jan. 2021), pp. 3–24. DOI: `10.1016/B978-0-12-818542-1.00067-9`.

[52] D Richter, G Haour, and D Richon. "Hot isostatic pressing (HIP)". In: *Materials & Design* 6.6 (1985), pp. 303–305. ISSN: 0261-3069. DOI: `https://doi.org/10.1016/0261-3069(85)90012-3`. URL: `https://www.sciencedirect.com/science/article/pii/0261306985900123`.

[53] M Omori. "Sintering, consolidation, reaction and crystal growth by the spark plasma system (SPS)". In: *Materials Science and Engineering: A* 287.2 (2000), pp. 183–188. ISSN: 0921-5093. DOI: `https://doi.org/10.1016/S0921-5093(00)00773-5`. URL: `https://www.sciencedirect.com/science/article/pii/S0921509300007735`.

[54] S. Hayun et al. “Microstructure and mechanical properties of silicon carbide processed by Spark Plasma Sintering (SPS)”. In: *Ceramics International* 38.8 (2012), pp. 6335–6340. ISSN: 02728842. DOI: `10.1016/j.ceramint.2012.05.003`.

[55] H P Meyers and H P Myers. *Introductory solid state physics.* CRC press, 1997. ISBN: 1420075020.

[56] Hendrik J. Monkhorst and James D. Pack. “Special points for Brillouin-zone integrations”. In: *Physical Review B* 13.12 (1976). ISSN: 01631829. DOI: `10.1103/PhysRevB.13.5188`.

[57] Zhen Zhang and John T. Yates. *Band bending in semiconductors: Chemical and physical consequences at surfaces and interfaces.* 2012. DOI: `10.1021/cr3000626`.

[58] W R (Wolfgang R.) Fahrner and Stefan Schwertheim. *Semiconductor thermoelectric generators.* Materials science foundations ; volume 61. Zurich: Trans Tech Publications, 2009. ISBN: 3-03813-321-3.

[59] Yasuhiro Ohba, Toshitada Shimozaki, and Hidenori Era. “Thermoelectric properties of silicon carbide sintered with addition of boron carbide, carbon, and alumina”. In: *Materials Transactions* 49.6 (2008). ISSN: 13459678. DOI: `10.2320/matertrans.MRA2007232`.

[60] Chul-Hoon Pai. “Thermoelectric properties of p-type silicon carbide”. In: *Seventeenth International Conference on Thermoelectrics. Proceedings ICT98 (Cat. No. 98TH8365).* IEEE, 1998, pp. 582–586. ISBN: 0780349075.

[61] Young-Wook Kim, Yong-Hyeon Kim, and Kwang Joo Kim. “Electrical properties of liquid-phase sintered silicon carbide ceramics: a review”. In: *Critical Reviews in Solid State and Materials Sciences* 45.1 (Jan. 2020), pp. 66–84. ISSN: 1040-8436. DOI: `10.1080/10408436.2018.1532394`. URL: `https://doi.org/10.1080/10408436.2018.1532394`.

[62] Y Taki et al. “Effect of B doping on electrical and thermal properties of SiC bodies fabricated by spark plasma sintering”. In: *Materials Today: Proceedings.* Vol. 16. 2019, pp. 211–215. DOI: `10.1016/j.matpr.2019.05.249`.

[63] G. G. Gnesin, V. K. Zakharenkov, and L. A. Shipilova. “Volume electrical resistivity of silicon carbide heating elements”. In: *Soviet Powder Metallurgy and Metal Ceramics* 17.1 (1978), pp. 72–76. ISSN: 00385735. DOI: `10.1007/BF00795145`.

[64] J. H. Racette. “Intrinsic electrical conductivity in silicon carbide”. In: *Physical Review* 107.6 (1957), p. 1542. ISSN: 0031899X. DOI: `10.1103/PhysRev.107.1542`.

[65] G. A. Slack. “Nonmetallic crystals with high thermal conductivity”. In: *Journal of Physics and Chemistry of Solids* 34.2 (1973), pp. 321–335. ISSN: 00223697. DOI: `10.1016/0022-3697(73)90092-9`.

[66] Martin Maldovan. “Thermal energy transport model for macro-to-nanograin polycrystalline semiconductors”. In: *Journal of Applied Physics* 110.11 (2011). ISSN: 00218979. DOI: `10.1063/1.3665211`.

[67] L. S. Sigl. “Thermal conductivity of liquid phase sintered silicon carbide”. In: *Journal of the European Ceramic Society* 23.7 (2003). ISSN: 09552219. DOI: `10.1016/S0955-2219(02)00271-6`.

[68] Jean Paul Crocombette and Laurent Proville. “Thermal conductivity degradation induced by point defects in irradiated silicon carbide”. In: *Applied Physics Letters* 98.191905 (2011). ISSN: 00036951. DOI: `10.1063/1.3589358`.

[69] Yukio Takeda. “Development of high-thermal-conductive SiC ceramics”. In: *American Ceramic Society Bulletin* 67.12 (1988). ISSN: 00027812. URL: `https://www.osti.gov/biblio/5833653`.

[70] Yinsheng Li et al. “Microstructure, thermal conductivity, and electrical properties of in situ pressureless densified SiC-BN composites”. In: *Journal of the American Ceramic Society* 98.3 (2015), pp. 879–887. ISSN: 15512916. DOI: `10.1111/jace.13376`.

[71] R. G. Munro. “Material properties of a sintered α-SiC”. In: *Journal of Physical and Chemical Reference Data* 26.5 (1997), p. 1195. ISSN: 00472689. DOI: `10.1063/1.556000`.

[72] R. T. Dolloff. *Research study to determine the phase equilibrium of selected metal carbides at high temperatures.* Ohio, 1960. URL: `https://apps.dtic.mil/sti/citations/AD0278009`.

[73] J Wade et al. “Contact damage of silicon carbide ceramics with different grain structures measured by Hertzian and Vickers indentation”. In: *Journal of the European Ceramic Society* 35.6 (2015), pp. 1725–1736. ISSN: 09552219. DOI: `10.1016/j.jeurceramsoc.2014.12.030`.

[74] E O HALL. “Variation of Hardness of Metals with Grain Size”. In: *Nature* 173.4411 (1954), pp. 948–949. ISSN: 1476-4687. DOI: `10.1038/173948b0`. URL: `https://doi.org/10.1038/173948b0`.

[75] E Gugel et al. “Investigations in the ternary system boron-carbon-silicon”. English. In: *Nat Bur Stand (U S), Spec Publ* (1972), pp. 505–513. URL: `https://www.osti.gov/biblio/4595562%20Gaithersburg,%20Md.%20(18%20Oct%201971).%20See%20NBS-SPEC.-PUBL--364`.

[76] G. A. Meerson et al. “Preparation and study of the properties of hard alloys from the pseudobinary section SiC-BC by growing from the gaseous phase”. In: *Soviet Powder Metallurgy and Metal Ceramics* 4.2 (1965), pp. 100–105. ISSN: 00385735. DOI: `10.1007/BF00777010`.

[77] G. A. Meerson et al. “Conditions of preparation and some properties of pseudobinary B4C-B4Si hard alloys”. In: *Soviet Powder Metallurgy and Metal Ceramics* 4.3 (1965), pp. 223–228. ISSN: 00385735. DOI: `10.1007/BF00773772`.

[78] Jinping Cui et al. “Load-deflection behavior of fracture toughness testing of ceramics by SEVNB method”. In: *International Journal of Applied Ceramic Technology* 15.5 (2018), pp. 1310–1315. ISSN: 17447402. DOI: `10.1111/ijac.12895`.

[79] Anzhe Wang et al. “A systematic study on the quality improving of fracture toughness measurement in structural ceramics by laser notching method”. In: *Theoretical and Applied Fracture Mechanics* 114.102981 (2021). ISSN: 01678442. DOI: `10.1016/j.tafmec.2021.102981`.

[80] George A. Gogotsi. “Fracture toughness of ceramics and ceramic composites”. In: *Ceramics International* 29.7 (2003), pp. 777–784. ISSN: 02728842. DOI: `10.1016/S0272-8842(02)00230-4`.

[81] Sarbjit Kaur, Raymond A. Cutler, and Dinesh K. Shetty. “Short-crack fracture toughness of silicon carbide”. In: *Journal of the American Ceramic Society* 92.1 (2009), pp. 179–185. ISSN: 00027820. DOI: `10.1111/j.1551-2916.2008.02829.x`.

[82] Rohit Malik and Young Wook Kim. “Pressureless solid-state sintering of SiC ceramics with BN and C additives”. In: *Journal of Asian Ceramic Societies* 9.3 (2021), pp. 1165–1172. ISSN: 21870764. DOI: `10.1080/21870764.2021.1946268`.

[83] J J Cao et al. “In situ toughened silicon carbide with Al-B-C additions”. English. In: *Journal of the American Ceramic Society* 79.2 (1996), pp. 461–469. DOI: `10.1111/j.1151-2916.1996.tb08145.x`. URL: `https://www.osti.gov/biblio/211706`.

[84] Rohit Malik and Young Wook Kim. “Effects of initial α-phase content on properties of pressureless solid-state sintered SiC ceramics”. In: *International Journal of Applied Ceramic Technology* 19.2 (2022), pp. 703–712. ISSN: 17447402. DOI: `10.1111/ijac.13892`.

[85] Janet B. Hurst and Sunil Dutta. “Simple Processing Method for High-Strength Silicon Carbide”. In: *Journal of the American Ceramic Society* 70.11 (1987), pp. C–303. ISSN: 15512916. DOI: `10.1111/j.1151-2916.1987.tb05642.x`.

[86] Yuhong Chen, Liang Jiang, and Xuehong Jia. “Properties of pressureless sintered SiC-TiB2 composites”. In: *Advanced Materials Research*. Vol. 177. 2011, pp. 369–372. DOI: `10.4028/www.scientific.net/AMR.177.369`.

[87] Haibo Wu et al. “Effects of Grain Grading on Microstructures and Mechanical Behaviors of Pressureless Solid-State-Sintered SiC”. In: *International Journal of Applied Ceramic Technology* 12.5 (2015), pp. 976–984. ISSN: 17447402. DOI: `10.1111/ijac.12409`.

[88] Charles E Anderson and James D Walker. “An analytical model for dwell and interface defeat”. In: *International Journal of Impact Engineering* 31.9 (2005), pp. 1119–1132. ISSN: 0734-743X. DOI: `https://doi.org/10.1016/j.ijimpeng.2004.07.013`. URL: `https://www.sciencedirect.com/science/article/pii/S0734743X04001289`.

[89] V Paris et al. “Fragmentation of armor piercing steel projectiles upon oblique perforation of steel plates”. In: *The European Physical Journal Conferences* 26.04032 (Aug. 2012). DOI: `10.1051/epjconf/20122604032`.

[90] M S Boldin et al. “Review of ballistic performance of alumina: Comparison of alumina with silicon carbide and boron carbide”. In: *Ceramics International* 47.18 (2021), pp. 25201–25213. ISSN: 0272-8842. DOI: `https://doi.org/10.1016/j.ceramint.2021.06.066`. URL: `https://www.sciencedirect.com/science/article/pii/S0272884221018058`.

[91] Mark Wilkins, Charles Honodel, and David Sawle. *APPROACH TO THE STUDY OF LIGHT ARMOR.* Tech. rep. 1967. URL: `https://www.osti.gov/biblio/4308612`.

[92] Darin Ray et al. “Effect of Room-Temperature Hardness and Toughness on the Ballistic Performance of SiC-Based Ceramics”. In: 2008. DOI: `10.1002/9780470291276.ch16`.

[93] M W Chen et al. “Dynamic plasticity and failure of high-purity alumina under shock loading”. In: *Nature Materials* 5.8 (2006), pp. 614–618. ISSN: 1476-4660. DOI: `10.1038/nmat1689`. URL: `https://doi.org/10.1038/nmat1689`.

[94] Andreas Krell and Elmar Strassburger. “Order of influences on the ballistic resistance of armor ceramics and single crystals”. eng. In: *Materials science & engineering. A, Structural materials : properties, microstructure and processing* 597 (2014), pp. 422–430. ISSN: 0921-5093. DOI: `10.1016/j.msea.2013.12.101`.

[95] O S Fakolujo et al. “Processing and Properties of Advanced Ceramics and Composites VI”. eng. In: Hoboken, NJ, USA: Hoboken, NJ, USA: John Wiley & Sons, Inc, 2014, pp. 83–91. ISBN: 9781118995495. DOI: `10.1002/9781118995433.ch9`.

[96] P G Karandikar et al. “Advances in Ceramic Armor IV: Ceramic Engineering and Science Proceedings, Volume 29, Issue 6”. eng. In: Hoboken, NJ, USA: Hoboken, NJ, USA: John Wiley & Sons, Inc, 2008, pp. 163–175. ISBN: 9780470344972. DOI: `10.1002/9780470456286.ch16`.

[97] Eugene Medvedovski. “Ballistic performance of armour ceramics: Influence of design and structure. Part 1”. In: *Ceramics International* 36.7 (2010), pp. 2103–2115. ISSN: 0272-8842. DOI: `https://doi.org/10.1016/j.ceramint.2010.05.021`. URL: `https://www.sciencedirect.com/science/article/pii/S0272884210002087`.

[98] Alexander B Dresch et al. “Ballistic ceramics and analysis of their mechanical properties for armour applications: A review”. In: *Ceramics International* 47.7, Part A (2021), pp. 8743–8761. ISSN: 0272-8842. DOI: `https://doi.org/10.1016/j.ceramint.2020.12.095`. URL: `https://www.sciencedirect.com/science/article/pii/S0272884220336968`.

[99] W. Ji et al. “Ultra-fast firing: Effect of heating rate on sintering of 3YSZ, with and without an electric field”. In: *Journal of the European Ceramic Society* 37.6 (2017), pp. 2547–2551. ISSN: 1873619X. DOI: `10.1016/j.jeurceramsoc.2017.01.033`.

[100] R. I. Todd et al. “Electrical characteristics of flash sintering: Thermal runaway of Joule heating”. In: *Journal of the European Ceramic Society* 35.6 (2015), pp. 1865–1877. ISSN: 1873619X. DOI: `10.1016/j.jeurceramsoc.2014.12.022`.

[101] Yuanyao Zhang, Jae Il Jung, and Jian Luo. “Thermal runaway, flash sintering and asymmetrical microstructural development of ZnO and ZnO-Bi2O3 under direct currents”. In: *Acta Materialia* 94 (2015), pp. 87–100. ISSN: 13596454. DOI: `10.1016/j.actamat.2015.04.018`.

[102] I. J. Hewitt, A. A. Lacey, and R. I. Todd. “A Mathematical Model for Flash Sintering”. In: *Mathematical Modelling of Natural Phenomena* 10.6 (2015), pp. 77–89. ISSN: 17606101. DOI: `10.1051/mmnp/201510607`.

[103] S K Jha et al. *Beyond flash sintering in 3 mol % yttria stabilized zirconia.* 2016. DOI: `10.2109/jcersj2.15248`.

[104] João Gustavo Pereira da Silva et al. “A dynamic bifurcation criterion for thermal runaway during the flash sintering of ceramics”. In: *Journal of the European Ceramic Society* 36.5 (2016), pp. 1261–1267. ISSN: 1873619X. DOI: `10.1016/j.jeurceramsoc.2015.11.048`.

[105] J S C Francis, M Cologna, and R Raj. “Particle size effects in flash sintering”. In: *Journal of the European Ceramic Society* 32.12 (2012), pp. 3129–3136. ISSN: 09552219. DOI: `10.1016/j.jeurceramsoc.2012.04.028`.

[106] J. Frenkel. *On pre-breakdown phenomena in insulators and electronic semi-conductors [3].* 1938. DOI: `10.1103/PhysRev.54.647`.

[107] S Grasso et al. “Flash Spark Plasma Sintering (FSPS) of α and β SiC”. In: *Journal of the American Ceramic Society* 99.5 (2016), pp. 1534–1543. ISSN: 15512916. DOI: `10.1111/jace.14158`.

[108] I Mazo, A Molinari, and V M Sglavo. “Electrical resistance flash sintering of tungsten carbide”. In: *Materials and Design* 213.110330 (2022). ISSN: 18734197. DOI: `10.1016/j.matdes.2021.110330`.

[109] S Grasso et al. “Flash spark plasma sintering (FSPS) of pure ZrB2”. In: *Journal of the American Ceramic Society* 97.8 (2014), pp. 2405–2408. ISSN: 15512916. DOI: `10.1111/jace.13109`.

[110] John G. Simmons. “Poole-Frenkel effect and Schottky effect in metal-insulator-metal systems”. In: *Physical Review* 155.3 (1967), pp. 657–660. ISSN: 0031899X. DOI: `10.1103/PhysRev.155.657`.

[111] M Yu et al. *Review of flash sintering: materials, mechanisms and modelling.* 2017. DOI: `10.1080/17436753.2016.1251051`.

[112] Christian Bechteler, Andrew Kirkpatrick, and Richard I Todd. "Visible light emissions during flash sintering of 3YSZ are thermal radiation". In: *Scripta Materialia* 219.114849 (2022). ISSN: 1359-6462. DOI: `https://doi.org/10.1016/j.scriptamat.2022.114849`. URL: `https://www.sciencedirect.com/science/article/pii/S1359646222003451`.

[113] Mattia Biesuz et al. "Theoretical and phenomenological analogies between flash sintering and dielectric breakdown in α-alumina". In: *Journal of Applied Physics* 120.145107 (2016). ISSN: 10897550. DOI: `10.1063/1.4964811`.

[114] M Biesuz and V M Sglavo. "Flash sintering of alumina: Effect of different operating conditions on densification". In: *Journal of the European Ceramic Society* 36.10 (2016), pp. 2535–2542. ISSN: 1873619X. DOI: `10.1016/j.jeurceramsoc.2016.03.021`.

[115] B Block, Y Kim, and D K Shetty. "Dielectric breakdown of polycrystalline alumina: A weakest-link failure analysis". In: *Journal of the American Ceramic Society* 96.11 (2013), pp. 3430–3439. ISSN: 00027820. DOI: `10.1111/jace.12492`.

[116] Michiyuki Yoshida, Simone Falco, and Richard I. Todd. "Measurement and modelling of electrical resistivity by four-terminal method during flash sintering of 3YSZ". In: *Journal of the Ceramic Society of Japan* 126.7 (2018), pp. 579–590. ISSN: 13486535. DOI: `10.2109/jcersj2.17256`.

[117] Victor M. Candelario et al. "Liquid-phase assisted flash sintering of SiC from powder mixtures prepared by aqueous colloidal processing". In: *Journal of the European Ceramic Society* 37.2 (2017), pp. 485–498. ISSN: 1873619X. DOI: `10.1016/j.jeurceramsoc.2016.08.024`.

[118] Andrew Rosenberger, Raymond E. Brennan, and Aubrey L. Fry. "Flash sintering feasibility study and localized densification in boron carbide". In: *Journal of the American Ceramic Society* 104.8 (2021), pp. 3823–3827. ISSN: 15512916. DOI: `10.1111/jace.17833`.

[119] John A. Downs and Vincenzo M. Sglavo. "Electric field assisted sintering of cubic zirconia at 390°C". In: *Journal of the American Ceramic Society* 96.5 (2013). ISSN: 00027820. DOI: `10.1111/jace.12281`.

[120] Andrew Gibson et al. "Pressureless flash sintering of α-SiC: Electrical characteristics and densification". In: *Acta Materialia* 241 (2022), p. 118362. ISSN: 1359-6454. DOI: `https://doi.org/10.1016/j.actamat.2022.118362`. URL: `https://www.sciencedirect.com/science/article/pii/S1359645422007418`.

[121] S. K. Jha et al. "Electric field induced texture in titania during experiments related to flash sintering". In: *Journal of the European Ceramic Society* 36.1 (2016). ISSN: 1873619X. DOI: `10.1016/j.jeurceramsoc.2015.09.002`.

[122] Jean Marie Lebrun et al. "Emergence and Extinction of a New Phase during On-Off Experiments Related to Flash Sintering of 3YSZ". In: *Journal of the American Ceramic Society* 98.5 (2015), pp. 1493–1497. ISSN: 15512916. DOI: `10.1111/jace.13476`.

[123] Dmytro Demirskyi and Oleg Vasylkiv. “Hot-spots generation, exaggerated grain growth and mechanical performance of silicon carbide bulks consolidated by flash spark plasma sintering”. In: *Journal of Alloys and Compounds* 691 (2017), pp. 466–473. ISSN: 09258388. DOI: `10.1016/j.jallcom.2016.08.234`.

[124] E A Olevsky, S M Rolfing, and A L Maximenko. “Flash (Ultra-Rapid) Spark-Plasma Sintering of Silicon Carbide”. In: *Scientific Reports* 6.33408 (2016). ISSN: 20452322. DOI: `10.1038/srep33408`.

[125] Bo Niu et al. “Ultra-fast densification of boron carbide by flash spark plasma sintering”. In: *Scripta Materialia* 116 (2016), pp. 127–130. ISSN: 13596462. DOI: `10.1016/j.scriptamat.2016.02.012`.

[126] S Grasso et al. “Ultra-Rapid Crystal Growth of Textured SiC Using Flash Spark Plasma Sintering Route”. In: *Crystal Growth and Design* 16.4 (2016), pp. 2317–2321. ISSN: 15287505. DOI: `10.1021/acs.cgd.6b00099`.

[127] Wei Qin et al. “Electrode Effects on Microstructure Formation During FLASH Sintering of Yttrium-Stabilized Zirconia”. In: *Journal of the American Ceramic Society* 99.7 (2016), pp. 2253–2259. ISSN: 15512916. DOI: `10.1111/jace.14234`.

[128] Lorena Batista Caliman et al. “Flash sintering of ionic conductors: The need of a reversible electrochemical reaction”. In: *Journal of the European Ceramic Society* 36.5 (2016), pp. 1253–1260. ISSN: 1873619X. DOI: `10.1016/j.jeurceramsoc.2015.12.005`.

[129] Y. Kubota, R. I. Todd, and M. Yoshida. “Controlling factors in flash sintering of ceramics”. In: *Ceramics Japan Bulletin of the Ceramic Society of Japan* 55.7 (2020), pp. 502–505. URL: `https://jglobal.jst.go.jp/en/detail?JGLOBAL_ID=202002251013398594`.

[130] Stephen L. Johnson, Ganesh Venugopal, and Andrew T. Hunt. “Flame-assisted flash sintering: A noncontact method to flash sinter coatings on conductive substrates”. In: *Journal of the American Ceramic Society* 101.2 (2018), pp. 536–541. ISSN: 15512916. DOI: `10.1111/jace.15218`.

[131] T Saunders, S Grasso, and M J Reece. “Ultrafast-Contactless Flash Sintering using Plasma Electrodes”. In: *Scientific Reports* 6.27222 (2016). ISSN: 20452322. DOI: `10.1038/srep27222`.

[132] Chrsitian Bechteler, Richard Todd, and Andrew Gibson. “formation and influence of plasma during flash sintering”. In: Krakow, 2022. URL: `https://www.researchgate.net/publication/362061027_formation_and_influence_of_plasma_during_flash_sintering`.

[133] M Biesuz et al. “Thermally-insulated flash sintering”. In: *Scripta Materialia* 162 (2019), pp. 99–102. ISSN: 13596462. DOI: `10.1016/j.scriptamat.2018.10.042`.

[134] Yinsheng Li et al. “Promoting core/surface homogeneity during flash sintering of 3YSZ ceramic by current path management: experimental and modelling studies”. In: *Journal of the European Ceramic Society* 41.13 (2021), pp. 6649–6659. ISSN: 1873619X. DOI: `10.1016/j.jeurceramsoc.2021.06.001`.

[135] Jungdeok Park and I. Wei Chen. “In situ thermometry measuring temperature flashes exceeding 1,700°C in 8 mol% Y2O3-stablized zirconia under constant-voltage heating”. In: *Journal of the American Ceramic Society* 96.3 (2013), pp. 697–700. ISSN: 00027820. DOI: `10.1111/jace.12176`.

[136] R Raj. “Joule heating during flash-sintering”. In: *Journal of the European Ceramic Society* 32.10 (2012), pp. 2293–2301. ISSN: 09552219. DOI: `10.1016/j.jeurceramsoc.2012.02.030`.

[137] M. Balat-Pichelin and A. Bousquet. “Total hemispherical emissivity of sintered SiC up to 1850 K in high vacuum and in air at different pressures”. In: *Journal of the European Ceramic Society* 38.10 (2018), pp. 3447–3456. ISSN: 1873619X. DOI: `10.1016/j.jeurceramsoc.2018.03.050`.

[138] ASTM. “ASTM B962”. In: 2017 Editi (2017). URL: `https://www.astm.org/b0962-17.html`.

[139] Mohamed Henini. “Scanning electron microscopy: An introduction”. In: *III-Vs Review* 13.4 (2000). ISSN: 09611290. DOI: `10.1016/S0961-1290(00)80006-X`.

[140] Anwar Ul-Hamid. *A beginners’ guide to scanning electron microscopy.* 1st ed. Vol. 1. London: Springer, 2018, pp. 129–180. URL: `https://www.researchgate.net/publication/328536320_A_Beginners'_Guide_to_Scanning_Electron_Microscopy`.

[141] Alec Saville et al. “MAUD Rietveld Refinement Software for Neutron Diffraction Texture Studies of Single and Dual-Phase Materials”. en. In: (2021). DOI: `https://doi.org/10.1007/s40192-021-00224-5`. URL: `https://tsapps.nist.gov/publication/get_pdf.cfm?pub_id=932239`.

[142] C R Groom et al. “The Cambridge structural database”. In: *Acta Crystallographica Section B: Structural Science, Crystal Engineering and Materials* 72.2 (2016). ISSN: 20525206. DOI: `10.1107/S2052520616003954`.

[143] Origin. *Origin: Data Analysis and Graphing Software*. 2020. URL: `https://www.originlab.com/origin`.

[144] Jaspreet Singh. “Atom probe tomography characterization of engineering ceramics”. PhD thesis. The University of Oxford, 2021, pp. 215–237. URL: `https://ora.ox.ac.uk/objects/uuid:60ef298f-bd52-47d4-984d-23982f2a6963`.

[145] B M Jenkins et al. “A more holistic characterisation of internal interfaces in a variety of materials via complementary use of transmission Kikuchi diffraction and Atom probe tomography”. In: *Applied Surface Science* 528.147011 (2020). ISSN: 01694332. DOI: `10.1016/j.apsusc.2020.147011`.

[146] Olof C. Hellman and David N. Seidman. "Measurement of the Gibbsian interfacial excess of solute at an interface of arbitrary geometry using three-dimensional atom probe microscopy". In: *Materials Science and Engineering A* 327.1 (2002), pp. 24–28. ISSN: 09215093. DOI: `10.1016/S0921-5093(01)01885-8`.

[147] Esteban Broitman. "Indentation Hardness Measurements at Macro-, Micro-, and Nanoscale: A Critical Overview". In: *Tribology Letters* 65.1 (2016), p. 23. ISSN: 1573-2711. DOI: `10.1007/s11249-016-0805-5`. URL: `https://doi.org/10.1007/s11249-016-0805-5`.

[148] R L Smith and G E Sandly. "An Accurate Method of Determining the Hardness of Metals, with Particular Reference to Those of a High Degree of Hardness". In: *Proceedings of the Institution of Mechanical Engineers* 102.1 (June 1922), pp. 623–641. ISSN: 0020-3483. DOI: `10.1243/PIME{\_}PROC{\_}1922{\_}102{\_}033{\_}02`. URL: `https://doi.org/10.1243/PIME_PROC_1922_102_033_02`.

[149] Roger Morrell. "Flexural strength testing of ceramics and hardmetals." In: *National Physics Laboratory* 7 (2007), pp. 4–5. URL: `https://eprintspublications.npl.co.uk/1564/1/mgpg7.pdf`.

[150] B. L. Boyce et al. "Detecting rare, abnormally large grains by x-ray diffraction". In: *Journal of Materials Science* 50.20 (2015). ISSN: 15734803. DOI: `10.1007/s10853-015-9226-3`.

[151] Stephen J. Bennison and Martin P. Harmer. "Effect of Magnesia Solute on Surface Diffusion in Sapphire and the Role-of Magnesia in the Sintering of Alumina". In: *Journal of the American Ceramic Society* 73.4 (1990), pp. 833–837. ISSN: 15512916. DOI: `10.1111/j.1151-2916.1990.tb05122.x`.

[152] Sean Gephart, Jogender Singh, and Anil Kulkarni. "Field assisted sintering of SiC using extreme heating rates". In: *Journal of Materials Science* 46.10 (2011), pp. 3659–3663. ISSN: 00222461. DOI: `10.1007/s10853-011-5283-4`.

[153] Yuanyao Zhang et al. "Probing the densification mechanisms during flash sintering of ZnO". In: *Acta Materialia* 125 (2017), pp. 465–475. ISSN: 13596454. DOI: `10.1016/j.actamat.2016.12.015`.

[154] William J. Clegg. "Role of carbon in the sintering of boron-doped silicon carbide". In: *Journal of the American Ceramic Society* 83.5 (2000), pp. 1039–1043. ISSN: 00027820. DOI: `10.1111/j.1151-2916.2000.tb01327.x`.

[155] Rishi Raj and Kalvis Terauds. "Bubble Nucleation during Oxidation of SiC". In: *Journal of the American Ceramic Society* 98.8 (2015), pp. 2579–2586. ISSN: 15512916. DOI: `10.1111/jace.13613`.

[156] G. Urretavizcaya, J. M. Porto López, and A. L. Cavalieri. "Pressureless Sintering of Al2O3/SiCw Materials: Effect of the Reducing Atmosphere". In: *Journal of the European Ceramic Society* 17.13 (1997), pp. 1555–1563. ISSN: 09552219. DOI: `10.1016/s0955-2219(97)00021-6`.

[157] B Harnisch. *Ultra-lightweight C/SiC Mirrors and Structures*. Tech. rep. Mechanical Engineering Department, ESA Directorate for Technical and Operational Support, ESTEC, Noordwijk, The Netherlands, 1998, p. 5. URL: `https://www.esa.int/esapub/bulletin/bullet95/HARNISCH.pdf`.

[158] Electro Optical Components Inc. *Molybdenum Mirrors: Substrate Materials for CO2 Laser Optics*. URL: `https://www.eoc-inc.com/co2-laser-optics-reflective-mirrors/molybdenum-mirrors-substrate-materials-for-co2-laser-optics/`.

[159] Wanxia Zhao, Zhiwei Sun, and Zeyad T. Alwahabi. "Emissivity and absorption function measurements of Al2O3 and SiC particles at elevated temperature for the utilization in concentrated solar receivers". In: *Solar Energy* 207.1 (2020), pp. 183–191. ISSN: 0038092X. DOI: `10.1016/j.solener.2020.06.079`.

[160] R. J. Thorn and O. C. Simpson. "Spectral emissivities of graphite and carbon". In: *Journal of Applied Physics* 24.5 (1953), p. 633. ISSN: 00218979. DOI: `10.1063/1.1721341`.

[161] Wei Wei Xu et al. "High-temperature mechanical and thermodynamic properties of silicon carbide polytypes". In: *Journal of Alloys and Compounds* 768 (2018), pp. 722–732. ISSN: 09258388. DOI: `10.1016/j.jallcom.2018.07.299`.

[162] Peter T.B. Shaffer. "Solubility of boron in alpha silicon carbide". In: *Materials Research Bulletin* 5.7 (1970). ISSN: 00255408. DOI: `10.1016/0025-5408(70)90061-9`.

[163] Bruce Teter, Steven D. Goodman, and David J. Galas. "Nano-precipitation in hot-pressed silicon carbide". In: *Journal of Materials Science* 36.22 (2001), pp. 5447–5455. ISSN: 00222461. DOI: `10.1023/A:1012429613824`.

[164] A Ghosh et al. "Elevated-Temperature Fracture Resistance of a Sintered α-Silicon Carbide". In: *Journal of the American Ceramic Society* 72.2 (1989), pp. 242–247. ISSN: 15512916. DOI: `10.1111/j.1151-2916.1989.tb06108.x`.

[165] B Mishra et al. "Experimental studies on the effect of size and shape of holes on damage and microstructure of high hardness armour steel plates under ballistic impact". In: *Materials & Design* 43 (2013), pp. 17–24. ISSN: 0261-3069. DOI: `https://doi.org/10.1016/j.matdes.2012.06.037`. URL: `https://www.sciencedirect.com/science/article/pii/S0261306912004244`.

[166] Mattia Biesuz and Vincenzo M Sglavo. "Flash sintering of ceramics". In: *Journal of the European Ceramic Society* 39.2 (2019), pp. 115–143. ISSN: 0955-2219. DOI: `https://doi.org/10.1016/j.jeurceramsoc.2018.08.048`. URL: `https://www.sciencedirect.com/science/article/pii/S0955221918305442`.

[167] E. Bichaud et al. "Flash sintering incubation in Al2O3/TZP composites". In: *Journal of the European Ceramic Society* 35.9 (2015), pp. 2587–2592. ISSN: 1873619X. DOI: `10.1016/j.jeurceramsoc.2015.02.033`.

[168] M Biesuz et al. “Investigation of electrochemical, optical and thermal effects during flash sintering of 8YSZ”. In: *Materials* 11.7 (2018), p. 1214. ISSN: 19961944. DOI: `10.3390/ma11071214`.

[169] Brandon McWilliams et al. “Enhanced Sintering Kinetics in Aluminum Alloy Powder Consolidated Using DC Electric Fields”. In: *Metallurgical and Materials Transactions A: Physical Metallurgy and Materials Science* 48.2 (2017), pp. 919–929. ISSN: 10735623. DOI: `10.1007/s11661-016-3861-4`.

[170] Brandon McWilliams, Jian Yu, and Frank Kellogg. “Sintering aluminum alloy powder using direct current electric fields at room temperature in seconds”. In: *Journal of Materials Science* 53.12 (2018), pp. 9297–9304. ISSN: 15734803. DOI: `10.1007/s10853-018-2207-6`.

[171] Yukio Takeda et al. “Effects of Elemental Additives on Electrical Resistivity of Silicon Carbide Ceramics”. In: *Journal of the American Ceramic Society* 70.10 (1987), pp. C-266-C–267. ISSN: 15512916. DOI: `10.1111/j.1151-2916.1987.tb04895.x`.

[172] Yinsheng Li et al. “High electrical resistivity of pressureless sintered in situ SiC-BN composites”. In: *Scripta Materialia* 69.10 (2013), pp. 740–743. ISSN: 13596462. DOI: `10.1016/j.scriptamat.2013.08.016`.

[173] Evgeniy N. Mokhov. “Doping of SiC Crystals during Sublimation Growth and Diffusion”. In: *Crystal Growth.* 2019. DOI: `10.5772/intechopen.82346`.

[174] V. L. Kuznetsova and R. I. Bresker. “Effect of B4C additions on the electric resistance of silicon carbide heaters”. In: *Refractories* 13.5-6 (1972), pp. 334–335. ISSN: 15739139. DOI: `10.1007/BF01284847`.

[175] Patrick D. Miller, J. G. Lee, and Ivan B. Cutler. “The Reduction of Silica with Carbon and Silicon Carbide”. In: *Journal of the American Ceramic Society* 62.3-4 (1979), pp. 147–149. ISSN: 15512916. DOI: `10.1111/j.1151-2916.1979.tb19041.x`.

[176] T M Tritt. “Thermoelectric Materials: Principles, Structure, Properties, and Applications”. In: ed. by K H Jürgen Buschow et al. Oxford: Elsevier, 2002, pp. 1–11. ISBN: 978-0-08-043152-9. DOI: `https://doi.org/10.1016/B0-08-043152-6/01822-2`. URL: `https://www.sciencedirect.com/science/article/pii/B0080431526018222`.